Dynamic Environments at the Origins of Life

Alkaline Vent Microfluidics in two and three Dimensions and Nucleoside Synthesis in prebiotically plausible Conditions

Maximilian Weingart

München 2024

Dynamic Environments at the Origins of Life

Alkaline Vent Microfluidics in two and three Dimensions and Nucleoside Synthesis in prebiotically plausible Conditions

Maximilian Weingart

Dissertation
der Fakultät für Physik
der Ludwig-Maximilians-Universität
München

vorgelegt von
Maximilian Weingart
aus Wörgl

München, den 31.07.2024

Erstgutachter: Prof. Dr. Dieter Braun
Zweitgutachter: Prof. Dr. Karen Alim
Tag der mündlichen Prüfung: 11.09.2024

Zusammenfassung

Auf der Suche nach einem möglichen Ursprung des Lebens auf der Erde, müssen alle Prozesse, die dazu beigetragen haben im Einklang mit den geo-physikalischen Gegebenheiten gewesen sein. Dies bedeutet, dass das Leben aus einfachsten chemischen Bausteinen entstehen musste, während alle Moleküle nur stark verdünnt in den präbiotischen Ozeanen vorhanden waren. Nukleinsäuren werden dabei als Ausgangspunkt für molekulare Evolution angenommen. Die genauen Vorgänge für mögliche Akkumulation von gelösten Molekülen und insbesondere die Synthese der primären Bausteine von Nukleinsäuren stellt eine der größten Herausforderungen auf dem Forschungsgebiet dar.

Alkalische Quellen werden als vielversprechende Umgebung für erste Prozesse in der Entstehung des Lebens angesehen, da sie die starke Gradienten über eine anorganische Mineralstruktur ausbilden. Ihre schlotartige Architektur erschwert allerdings jegliche Visualisierung oder Untersuchung der Gradienten im Labor. **Kapitel 3** widmet sich daher einer möglichen quasi-zweidimensionalen Anordnung, die die zeitaufgelöste Mikroskopie der Mineralienentstehung bei Injektion einer basischen Lösung in eine eisenreiche Flüssigkeit. Verschiedene Fließgeschwindigkeiten und Ionen-Konzentrationen führen zur Bildung verschiedenster Strukturen durch die ausgefällten Mineralien. Parallele, fingerartige Morphologien ermöglichten dabei die Entstehung und Aufrechterhaltung von pH-Gradienten, sowie die lokale Akkumulation dispergierter Partikel. Dieser Ansatz bietet nicht nur die Möglichkeit zur Untersuchung von Gradienten an semi-permeablen Membranen, sondern könnte auch mögliche Prozesse innerhalb dünner Risse im Meeresboden simulieren.

In **Kapitel 4** wurde die Akkumulation von gelösten Nukleinsäuren in dreidimensionalen Nachbildungen dieser Szenarien untersucht. Die charakteristischen schlotartigen Strukturen bildeten sich unter Infusion alkalischer Lösung in einen Kolben mit eisenhaltige Lösung mit gelöster DNA zur Simulation eines präbiotischen Ozeans. Messungen der DNA-Konzentration nach der Ausfällung einer Schlotstruktur, sowohl im Ozean als auch am Schlotmaterial, legten eine Anreicherung von DNA-Strängen am Mineral nahe, während die Ozeanlösung kaum DNA aufwies. Folgeexperimente mit RNA konnten diese Beobachtung bestätigen und zeigten, dass RNA im Laufe der Zeit aus der Ozeanlösung entzogen wird, was auf eine Bindung an gelöste Eisenkomplexe hindeutet, die sich rasch an den entstehenden mineralischen Präzipitaten anlagern. Alkalische Quellen könnten daher eine Möglichkeit darstellen, gelöste Nukleinsäuren aus verdünnten präbiotischen Ozeanen zu akkumulieren.

Kapitel 5 beschäftigt sich schließlich mit möglichen Rahmenbedingungen für die präbiotische Synthese von Nukleosiden als Vorläufermoleküle für erste Nukleinsäuren. Die kovalente Bindung von Nukleobase und D-Ribose wurde hier als Übersichtsprüfung verschiedener physikalischer und chemischer Bedingungen aufgesetz, um eine Abschätzung plausibler Voraussetzungen für zukünftige experimentell Ansätze zu erlangen.. Ein Vergleich der relativen Ausbeuten der Reaktionen legte nahe, dass die erhöhte Dynamik von periodischen Nass-Trocken-Zyklen eine effektive Methode darstellen. Bei der Synthese von Guanosin konnten außerdem Luft-Wasser-Grenzflächen in einem thermischen Ungelichgewicht die Ausbeute noch weiter steigern, und vergleichbare Ergebnisse wie bei der Zugabe von Carbonat erreichen. Diese Ergebnisse liefern eine Abschätzung für vielversprechende präbiotisch kompa-

tible Synthesebedingungen von Nukleosiden und können als Ausgangspunkt für eine tiefgreifendere Analyse in der Zukunft dienen.

Abstract

Alongside the search of a potential origin of life on Earth, it is clear, that all processes leading towards life's first molecules had to be compatible with the geo-physical circumstances provided by Earth's prebiotic environment. This implies that life not only had to emerge from simple chemical building blocks but also from the highly diluted solutions posed by the prebiotic oceans. As all living systems require information storing molecules, nucleic acids are assumed to be the starting point for molecular evolution. However, the mechanisms of how molecules could accumulate in early geological settings are poorly understood and especially the formation of nucleic acids primary building blocks poses one of the biggest challenges in the research field.

Alkaline hydrothermal vents are considered one plausible location along the path to life, as they facilitate the creation of strong gradients across inorganic mineral membranes, precipitated into tubular chimney structures. As any kind of testing or visualisation of the gradients is difficult in this three dimensional setting, **chapter 3** investigated the potential of a quasi-2-dimensional setup, enabling the spatio-temporal visualisation of the mineral formation process in low volumes upon the injection of an alkaline fluid into an iron-rich solution. Variation in inflow rate and ion concentration could show the emergence of different precipitation morphologies. Within this confined geometry, the formation of stable, finger-like precipitation structures have been found to allow for the emergence and subsequent maintenance of microscale pH gradient and locally accumulate dispersed particles. This setting provides not only a model to study gradients across semi-permeable boundaries, but could also represent potential precipitation processes within fractures in the seafloor.

Zooming further out of this confined setting, **chapter 4** studied the potential for accumulation of diluted nucleic acids in three dimensional recreation of alkaline vent chimneys. The characteristic tubular structures formed upon injection of an alkaline solution into a flask containing and iron-rich solution simulating a prebiotic ocean that included long strands of dissolved DNA. Measurements of DNA concentration after the growth of a precipitate chimney in both, ocean and chimney, suggested the localisation of the strands on the mineral structure, while the ocean was mostly depleted. Follow up experiments with RNA could confirm this observation and showed the depletion of RNA from the ocean solution over time, suggesting the binding of RNA to dissolved iron complexes that accumulated rapidly on the emerging mineral precipitates. Alkaline vent environments could therefore pose a way of accumulating dissolved nucleic acids from diluted prebiotic oceans.

Chapter 5 lastly explores possible boundaries for the prebiotic synthesis of nucleosides as precursor molecules towards first nucleic acids. The formation of a covalent glycosidic bond between nucleobase and D-ribose was approached here as the screening of a range of physical and chemical conditions to get an estimate of potential settings for further investigation. Comparison of relative reaction yields, suggested dynamics of wet-dry cycles as an effective settings for the improvement of canonical nucleosides yields. For the formation of guanosine air-water interfaces in a thermal gradient could boost the yield even further and reach comparable results in the presence of carbonate. These findings provide a rough estimate

of potential boundary conditions for the prebiotic synthesis of nucleosides and can serve as starting point for thorough analysis in the future.

Contents

Chapter 1

Motivation: The Early Stages in the Origins of Life

The onset of all living systems on Earth is a mystery that is not yet solved and might as well never will be with absolute certainty. Nevertheless, or maybe exactly because of that the question about the origin of life has been fuelling the curiosity of humans since the beginning of mankind. Many scientist have tackled the search for possible theories in agreement with scientific findings that could explain the transition from highly entropic clutter to self-sustaining ordered structures. Any insights on the requirements necessary for life's emergence, however, not only give clues about life on Earth, but how it could have emerged elsewhere under comparable conditions.

Attempting to find a possible answer to this question, the field of origin of life research evolves around these three key features:

(i) Apparent information,

(ii) Evident information and

(iii) Hypothesised connections.

Apparent information (i) summarises all the insights that are at hand now and can be directly observed form contemporary structures. This includes all kinds of modern life forms, from simple to complex, that show the structures that have been emerged at some point along the history of Earth. In the same way it also includes Earth itself and the geological circumstances that make life possible today. Knowing those results of modern biology and geology, this information can be extrapolated to estimate potential precedent structures and ways how they came into existence. To get some of the waymarks along this road, we can gain information from latent evidence (ii) still available today. Fossilised structures or inherited genetic patterns give clues about early forms of life, and together with radio-dating and elemental mapping rough insights into Earth's environment many million years ago. These boundaries then form the basis for hypotheses (iii) trying to find plausible connections in between. Any proposed theory can the be supported by simulations and experiments in the laboratory to find agreement with the extrapolated and evident requirements.

Using now the evidence, obtained form the oldest ever found fossils, radio-isotope analysis of their surrounding rock allows an estimation for an upper limit for the origin of life about 3.5Ga ago [1]. More recent findings, however, might have even found evidence for even older fossils in hydrothermal vent like environments, dating back the latest possible time for the origin of life to already 3.8Ga ago [2,3]. On the other hand, the moon forming impact around 4.5Ga ago [4,5] can be assumed to have would have wiped away all potential previous forms of life, rendering the Earth inhabitable [6]. After this Earth needed about 200Ma years to cool down and the formation of a crust and hosting of water [7], framing the window from 4.3Ga to 3.8Ga ago for life to emerge [6].

Considering the lower end of this time frame, it becomes apparent that the very first steps towards the origin of life have to had been dominated by geology. Thus, the geological circumstances must have played a crucial role in all potential scenarios. Even though the first things that likely come to ones mind when thinking about the start of molecular evolution are usually chemical processes, that must have formed new molecules form simple abiotic building blocks, they need to be compatible with the predicted geological environment [8]. However, this additionally also comes with the corresponding physical boundaries. Put together, this means an origin of life needs to happen in a geological environments within the (geo)-physical boundaries from the available (geo)-chemical material. With this in mind, it becomes clear, that one of the most crucial considerations is the search for a plausible location that could provide the conditions endorsing the early stages of the origin of life. The earlier the considered stages are along the route form abiotic molecules to live, the more important seems the necessity for compatibility with the surrounding.

After the early Earth cooled down to provide habitable temperature it took until approximately 4.2Ga ago for a stable hydrosphere to form [6, 9]. At this state, any kind of dissolved molecules could only be present in highly diluted form in the bulk water of an extensive ocean. This scenario is commonly referred to as the concentration problem in the origin of life [10]. Past research has shown that physical non-equilibrium conditions could effectively boost the accumulation and localisation of dissolved molecules to overcome this problem [11–16]. Live itself is inherently based on disequilibria [17, 18] and as already stated by Schrödinger in 1944 [19] all life requires non-equilibria to stay alive. The proposal that life also needed non-equilibria to be started initially, would close the circle and not come surprisingly.

One promising location for the origin of life could be alkaline hydrothermal vents (AHV) [20–22]. It is not only that the oldest putative fossils haven been found in potential hydrothermal structures [2], they also host a variety of different chemical and physical non-equilibria and further conditions beneficial for prebiotic reactions [23–27]. The vents form when ocean water seeps into the cracks and fracture in the ultramafic seafloor and gets enriched in ions and strongly alkaline after reaction with the surrounding rock [28, 29]. Buoyancy then causes the alkaline fluid to be exhaled back into the ocean and precipitate into chimney-like tubes upon contact with the ocean water [26, 30]. This creates steep gradients in temperature, pH, redox-potential or ion-composition between the fluid stream inside the chimneys and the surrounding ocean, separated by a semipermeable mineral barrier [26, 31]. Also the unique geo-chemical composition featuring highly reactive Fe(Ni)S minerals is thought to have catalytic effects [32] a variety of organic and inorganic synthesis reactions [26, 32], while at the same time the CO_2 reduction together with dissipating heat form Earth's mantle provides an energy source [32, 33]. Not least because of that, AHV are the centre of the eponymous theory for a metabolism-first hypothesis [22]. This proposes the ability of the proton gradients could boost CO_2-reduction and thus allow abiotic organic synthesis, similar to the acetyl-CoA pathway in bacteria and archea [21, 24, 26, 34, 35], favouring the formation of reduced carbon compounds essential for life [22, 36]. This would suggest abiotic structure capable of basic proto-metabolic functions as precursors to life's cellular structures [22, 37]. Additionally, the physical structure of AHVs resembles that of an autotrophic cell with an alkaline interior separated by a permeable barrier from an acidic outside [26].

Historically, this hypothesis was one of two strongly opposing approaches within origin of life researchers, metabolism-first and replication-first [24, 38]. The latter is represented by the so called RNA world theory [38], proposing the first step towards life to be the replication

of information storing molecules, building a key requirement for all forms of life. Ribonucleotides are therefore considered the most promising species of molecules as they not only have the capability to store complex information in the form polymers, but also having the ability to auto-catalyse their own replication [38, 39]. Nowadays, both theories are even considered comparable and inclusive [40].

Besides all different theories and approaches, it is clear that the beginning of the simplest living systems and their evolution to the outstanding complexity of life as we know it today has been and still is one of the most striking questions of mankind. Tackling this challenge needs joint interdisciplinary forces that address the task from many different angles, starting form modern biology as a top-down approach or from prebiotic geo-chemistry as bottom-up. Every new insight along the path adds one piece to the puzzle, that might one day give us a clearer vision of our own origin. Along this spirit, theses thesis aims to explore some of the very early stages within potential origins of life in potentially dynamic prebiotic environments. Therefore, it will investigate recreations of alkaline vents in two and three dimensions and the synthesis of ribonuclesides under various dynamic conditions. In summary the following chapters will address three main questions:

(1) Can quasi-2-dimensional alkaline vent precipitates generate gradients and accumulate dispersed particles?

(2) Can three-dimensional alkaline vent chimneys trap and localise long nucleic acids from bulk ocean water?

(3) How can different dynamic conditions, non-equilibria and salts/minerals influence the synthesis of nucleosides?

Chapter 2 will therefore give a short outline about the underlying geological, chemical and physical theory, necessary for the following chapters. It will give an introduction to modern and putatively prebiotic alkaline hydrothermal vents, the structures and properties of (ribo)-nucleic acids and physical non-equilibrium conditions and potentially resulting molecular transport processes. Chapter 3 will study the capability of a thin microfluidic chamber, that allows spatio-temporal visualisation of precipitation morphology formation under different parameters. Inclusion of pH sensitive dyes and fluorescence beads will then be used to assess their potential for gradient formation and the accumulation of dispersed particles. Zooming further out, chapter 4 uses three-dimensional recreations of alkaline vents to explore if dissolved DNA can be sequestered and localised by the electro-chemical gradients on the precipitating minerals. The experiments first aim, to optimise setup and protocols for DNA incorporation. Follow up experiments then probe the effect for RNA. In chapter 5 the question about first informational bio-polymers will be addressed, by screening of nucleoside formation under various conditions. Starting with the primary sub-structures of nucleosides, ribose and nucleobases, to evaluate the potential for synthesis in presence of alkaline vent minerals, in thermal non-equilibria or under wet-dry cycling and compared to dehydration.

Finally, chapter 6 will summarise the findings and connect the different parts into a bigger picture. At last, some outlook on further research and potential next steps will be given.

Chapter 2 Theoretical Background

The following chapter is intended to briefly summarise the necessary basics for the experiments presented in this thesis. Therefore, it will cover the major aspects of geological, (bio)chemical and physical essentials and give an introduction to submarine hydrothermal vents, nucleosides as the building blocks of life's information storing molecules and and the main (transport) processes induces by physical non-equilibria.

2.1 Submarine Hydrothermal Vents

Submarine hydrothermal vents have first been discovered on Earth in the early 80s [20, 41] and immediately gained interest for origin of life research [21]. These so called "Black Smokers" usually form near sub-seafloor magma chambers and obtain most of their energy from the resulting volcanic activity. Therefore, they emit hot fluids of up to 410 °C [41] of strongly acidic nature (pH 2-3) and enriched in dissolved transition metals [42]. The overall environment with dissolved gases and metal, hosting gradients in temperature and chemical compositions appeared to have a strong resemblance of what is known about prebiotic environments [21, 24]. Also, investigated Black Smokers showed a rich microbial community applying chemosynthesis to gain energy form reactions of ocean water with surrounding rocks [20], which makes them even more plausible as a primordial environments suitable to host life.

However, about twenty years later in 2000, a fundamentally new type of vents has been discovered [30, 43] that is commonly referred to as alkaline hydrothermal vents or White Smokers. The most prominent example for these types of vents is the Lost City Hydrothermal Field, the site of first discovery near the mid-Atlantic ridge, characterised by its carbonate-rich precipitates [30, 43]. The most important difference to Black Smokers is given by the considerably lower temperature of only up to 90 °C and the venting of strongly alkaline fluids (pH 9-11) [24, 30]. Especially this high alkalinity of the fluid in White Smokers, make them especially interesting for potential origin of life scenarios [24] as will be further elaborated below.

Within this thesis, the focus will lie on this second type of hydrothermal vents. Therefore all experimental recreations and interpretations will be based on alkaline vents. The following sections will now describe their structure and emergence together with possible Hadean predecessors and their relevance within origin of life research.

2.1.1 Formation and Structure of Alkaline (Hydrothermal) Vents

Alkaline hydrothermal vents (AHV) are emerging in off-axis locations form the ultramafic seafloor and grow into characteristic tubular structures, resembling chimneys rising from the ground of the ocean [30]. Primarily, the main prerequisites for the formation of those vents are a heat source and a fluid phase [33]. The fluid for this phenomenon, however, furthermore requires cracks and fractures in the seafloor, forming an extensive network of

interconnected pores to allow fluid circulation in a permeable lithology [24, 33]. The ocean water can flow into those small gaps and percolate Earth's upper mantle usually comprised of mainly ultramafic rock [44]. Upon contact of the ocean water with the surrounding rock, a metamorphic chemical reaction sets in, called serpentinisaion [28, 29]. It converts the ultramafic rock to serpentinite in an exo-thermal process, leaving the water alkaline, ion-enriched and strongly reducing [24, 29].

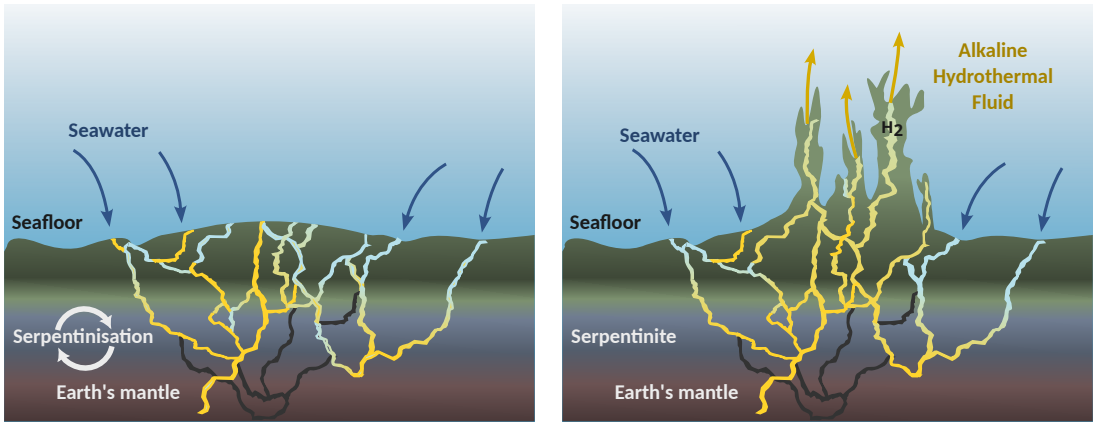

Figure 2.1: Formation of hydrothermal vents. Ocean water seeps into the cracks and fractures of the ultramafic seafloor. Upon contact with the surrounding rock, a metamorphic reactions converts the rock to serpentinite and leaves the water strongly reduced, alkaline and enriched in ions. Dissipating heat from the mantle and the exothermic serpentinisation drive the fluid through the pore network by convection and yield subsequent exhalation into the ocean due to buoyancy. Upon contact with the ocean water minerals start precipitating around the vented fluid stream and grow into the characteristic chimney-like shape. Figer in parts adapted from [45].

The fluid circulation is mostly driven by convection, due to dissipating heat from the mantle and the exothermic nature of the reaction. Hence, the alkaline water reaches temperatures of 40-90 °C and can therefore be considered a low-temperature hydrothermal vents [24, 43]. This entails a considerably lower density of the sub-seafloor fluid compared to the ocean water, which results in exhalation back into the bulk ocean by buoyancy. As soon as the two fluids come into contact, precipitation sets in due to the difference in pH. The minerals precipitate in the interfaces between the two fluids all around the fluid stream, which results in the growth of vertical tubes giving the vents their characteristic chimney-like appearance [24, 43]. In low-temperature alkaline vents like the Lost City Hydrothermal field the chimney reach up to 60 m in height [30, 33]. The seafloor in this area is dominated by serpentinisation resulting in the most common minerals to precipitate being calcium carbonate and brucite [30].

2.1.2 Prebiotic Alkaline Vents

Although it is likely, that suchlike hydrothermal vents have been present on an early Earth ~4 Ga ago [21], they have probably differed to modern vents. Since Earth started to have oceans of liquid water approximately 4.4 Ga ago [7] it also gave the possibility to react with

ultramafic rock on the seafloor leading to hydrothermal alteration and therefore also serpentinisation [28,46,47], especially as ultramafic intrusions could have been more abundant [48]. The atmosphere of an early Earth in the Hadean was also drastically different [49] and had high levels of CO_2 [50]. Thus, the ocean water itself, was probably saturated with CO_2 from the atmosphere [51] and thus more acidic [52–54]. Apart from that, it is suggested that the Hadean and Archean oceans have been rich in high amounts of dissolved iron providing ferruginous conditions in addition with the lack of oxygen [51, 52, 55]. The potentially lower pH of the ocean water has probably inhibited the precipitation of brucite or carbonate minerals like in Lost City vents [43], due their high solubility in acidic milieu. However, fougerite or "green rust" a different kind of mineral is assumed to be plausible in prebiotic AHVs due to the ferruginous conditions and especially interesting for the emergence of life [54, 56, 57]. This redox-reactive mineral has the capability of creating semi-permeable mineral barriers to maintain gradients between the acidic ocean water and the alkaline hydrothermal fluid [54, 56, 58, 59].

2.1.3 Gradients in Alkaline Hydrothermal Vents

Hydrothermal environments are a setting of non-equilibria. Their processes are not only driven by temperature and density differences that lead to fluid transport, they are also capable of generating steep gradients in temperature, redox-potential and pH between the hydrothermal fluid and the ocean water [23, 24]. This setting is especially interesting, since the two fluid are separated by the mineral precipitates acting as a semi-permeable membrane. This setting also strongly reminds of the topological structure of modern autotrophic cells [24, 26].

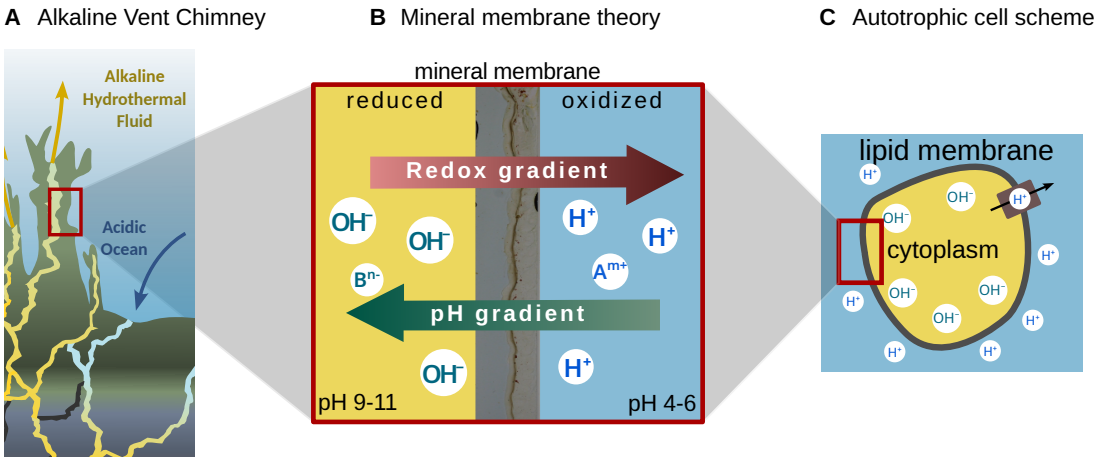

Figure 2.2: Gradients across a semi-permeable membrane. Mineral precipitates such as fougerite can form between the the alkaline fluid stream and the surrounding ocean water. As a result they act as a semi-permeable barrier, separating areas of high and low pH as well as high and low redox-potential. Topologically, this resembles the basic structure of all modern autotrophic cells [26, 31]. Whereas cells, however, need active trans-membrane mechanisms to keep the gradients up, hydrothermal vents continuously feed in OH^- ions by the the effluent hydrothermal fluid. A partly adapted from [45], B and C form [60].

2.2 Nucleic Acid Basics

All living matter that we know today is based on proteins. The plans of their precise structure requires information storing molecules, capable of storing and replicating these information at high accuracy. Modern organisms therefore use nucleic acids, namely RNA and DNA, to store all its genetic informing. These long bio-polymers encode the blueprints for protein biosynthesis in the sequence of their single monomeric subunits, each of them characterised by one of the four canonical nubleobases (A, G, C, U/T). Triplets of those monomers, encode for either of twenty essential amino acids, which, chained together and folded in the correct order, build up a specific protein. The following sections will in more detail describe the structure of the building blocks of these information storing monomers and their potential arise in context of the emergence of life.

2.2.1 Chemical Structure of Nucleic Acids

RNA and DNA are long polymers, built up from their monomers, so called nucleotides. Nucleotides, in turn, are assembled from three precursor molecules: sugar, nucleobase and phosphate (see **Figure 2.3 B**). The nucleobases also characterise the nucleotide as one of four canonical types by incorporating either Adenine, Guanine, Cytosine or Uracil as the base in RNA-nucleotides. DNA-nucleotides in contrast, use the base thymine instead of uracil. Another key difference between RNA and DNA is the conformation of the sugar, in specific the group at the 2' end. While D-deoxyribose is used in DNA, D-ribose is used in RNA.

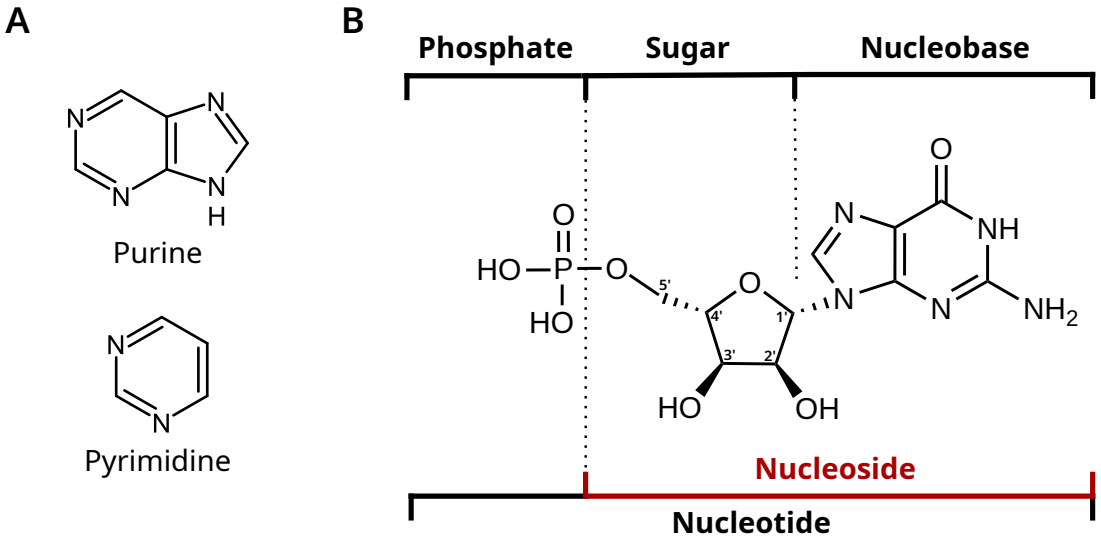

Figure 2.3: Chemical structure of a nucleotide and its precursors. **A**) All nucleobases are derived from either purine or pyrimidine, which also allows their classification in purine- and pyrimidine-based nucleobases. **B**) A nucleotide is composed of three precursor molecules, a nucleobase, a sugar and a phosphate group. Just nucleobase and sugar without phosphate are called nucleoside. The figure shows the example of a ribo-guanosine mono-phosphate nucleotide, with D-ribose as sugar and guanine as nucleobase.

The nucleic acid's characteristic long chains, that store information in the specific sequence of their links are formed by polymerisation of nucleotides. A single strand is thus

build up by binding of the phosphate group on one nucleotide to the 3'-end of the sugar in the next nucleotide and so on. In order to form a double-strand, the nucleobases on a single strand need to hybridise to their corresponding matching base on a complementary strand. Therefore, adenine binds to uracil or thymine and guanosine to cytidine via hydrogen bonding.

All of the common nucleobases are derivatives of either one of two precursor molecules, purine or pyrimidine **Figure 2.4 A**). This allows the classification of nucleobases in purine-bases (adenine and guanine) or pyrimidine-bases (cytosine, uracil and thymine). A nucleobase binding only to a sugar, basically a nucleotide without the phosphate, is called nucleoside. Especially for the prebiotic pathway towards first RNA molecules, nucleosides are considered precursor molecules alongside nucleotides [61]. Within this thesis, the focus will solely lie on ribonucleosides. In the following, only the structure of RNA-nucleosides will be covered in detail.

2.2.2 Ribonucleosides and their Stereoisomers

To form a nucleoside, ribose and nucleobase are connected via an N-glycosidic bond between the 1'C atom of the sugar and either the 1N or or the 9N atom in pyrimidine- or purine-nucleobases respectively. The corresponding canonical nucleosides are called guanosine, cytidine, adenosine and uridine.

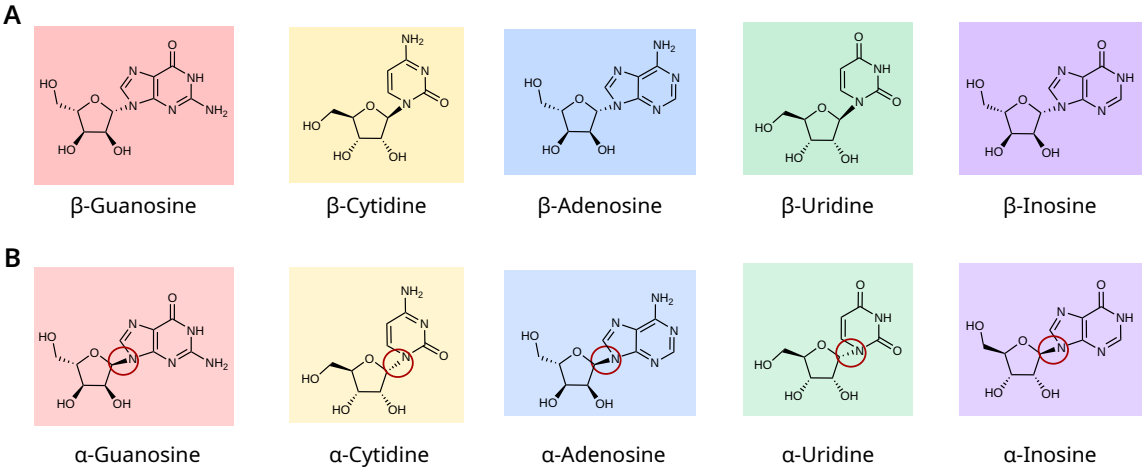

Figure 2.4: Structures of five Ribonucleosides. **A**) β-Ribonucleosides as used in RNA are composed of D-Ribose binding via a βN-glycosidic bond to one of the four canonical nucleobases to form the corresponding nucleosides Guanosine, Cytidine, Adenosine and Uridine. Inosine is a non-canonical nucleoside that used the base hypoxanthine, but might is thought to be an important precursor along the prebiotic formation of nucleosides [61–63]. **B**) Changed steric orientation of the N-glycosidic bond gives the α-anomers of the nucleosides. However, the β-form is mostly used in living systems.

A further, non-canonical nucleoside is inosine that is formed by binding of the base hypoxanthine to the ribose. Although it is not used in the nucleic acids of modern life, it is thought to be a potential precursor molecule for guanosine along the the emergence of first RNA structures [61–63]. The glycosidic bond between nucleobase an sugar, however, forms

an anomeric center and allows two steric conformations. Thus, two anomers α- and β-form nucleosides (**Figure 2.4**) can form. Life only uses the β-form of nucleosides in nucleic acids.

2.3 Physical Non-Equilibria

Physical non-equilibria are primarily established as gradients in one or more of a systems parameters. They can not only induce mass or particle transport processes, but as a consequence also locally enhance the concentration of dissolved molecules and create periodically cycling conditions in a system. The following sections will briefly explain the most relevant effects in microfluidic systems as well as in confined pores subjected to a temperature gradient.

2.3.1 Gradient Induced Transport Processes

The most important phenomena inducing a mass transport of particles or molecules by non-equilibrium in the following experiments are convection/advection, diffusion and diffusiophoresis. Convection describes the transport process by bulk motion of a liquid or gas. While essentially describing the same phenomenon, the term advection technically describes the mass transport within a bulk fluid flow. Convection or advection is induced by keeping a system out of equilibrium, e.g. by inducing local changes in the fluid. This can happen indirect by the resulting density variations in a thermal gradient in combination with gravity. This can e.g. cause the exhalation of hydrothermal fluid in submarine vents or cause a circular motion in a closed, confined compartment (cf. next section). Dissolved or dispersed particles, will as a result be dragged with the flow of the bulk fluid, which gives an advective flux of solutes of the same magnitude as the convective flow:

$$\vec{j}_{\text{adv}} = \vec{v} \cdot c, \tag{2.1}$$

with $\vec{v}$ being the velocity of the bulk liquid and c the concentration of solutes. Since the main focus within this thesis will be on the transport of dissolved molecules or particles within a liquid, the term "advection" will mainly be used in the following.

Diffusion is an effect, that occurs in the presence of a gradient in concentration of a solute within a solvent. It is based on Brownian motion, the random thermal fluctuations every particle experiences and drives solute molecules form areas of higher concentration towards areas of lower concentration. The directed, resulting flux can be described by Fick's first law:

$$\vec{j}_{\text{diff}} = -D \cdot \nabla c, \tag{2.2}$$

with diffusion coefficient D of the solute molecules and ∇c the gradient in their concentration. If two areas of high and low concentration are separated by a semi-permeable membrane, an effect called osmosis is triggers. While the membrane allows solvent molecules to pass through but not solute molecules, the concentration difference is equilibrated by diffusion of solvent molecules through the membrane. This, however, creates a pressure difference between the two sides, that allows the flow of solvent to equilibrate the concentration difference.

Hydrothermal vents create steep ionic gradients that could lead to so called diffusiophoresis [31]. This describes the transports of suspended particles, like macromolecues (e.g. RNA),

colloids or cells, in the concentrations gradient of another dissolved species of solutes in a solvent [64]. The resulting motion is directed against the motion of the diffusing solute molecules. In electrolyte solutions, e.g. in solutions of high salt/ion content like in hydrothermal systems, the diffusiophoretic movement results as the superposition of a osmotic pressure (chemiphoresis) and spontaneously emerging eclectic fields (electrophoresis) [31, 64]. The resulting diffusionphoretic flux can be written as the combination of both chemiphoretic velocity $\vec{v}_{\mathrm{cp}}$ and electrophoretic velocity $\vec{v}_{\mathrm{el}}$ [31]:

$$\vec{j}_{\mathrm{dp}} = \vec{v}_{\mathrm{cp}} + \vec{v}_{\mathrm{el}} = D_{\mathrm{dp}}^{\mathrm{osm}} \cdot \nabla \log I + \mu \cdot E_{\mathrm{diff}}, \tag{2.3}$$

where $D_{\mathrm{dp}}^{\mathrm{osm}}$ is the particles osmotic diffusiophoretic coefficient, I is the ionic strength of the solute, μ the particles electrophoretic mobility and E_{diff} the electric field generated by differently diffusion ionic species.

2.3.2 Air-Water Interfaces in Confined Spaces

Thin confined spaces containing air-water mixtures, subjected to a temperature gradient can exhibit several effects that can lead to the accumulation of molecules and periodically cycling conditions of high dynamics [15, 16, 65]. In **Figure 2.5** the schematics of a thin compartment in the boundaries of a thermal gradient is shown, based on the publications by [15, 16, 65]. Due to the the difference in temperature between the two sides several effects will be triggered at the air water interface. First of all, evaporation of water will be triggered on the hot side, leading to increasing vapour pressure in the gas phase on top. This, in turn will induce condensation on the cool side of the chamber with droplet formation on the wall. With continued evaporation, those droplets will grow until they reach a certain size and fall back down into the liquid. In this way, evaporation-condensation cycle is established in the gas phase.

In the liquid phase on the other hand, the evaporation causes a phenomenon called the ”coffee-ring effect”. It describes the increasing concentration of dissolved material at the interface between liquid and gas due to evaporation of liquid. This effect is further boosted by increased evaporation at higher temperatures and shifts the capillary flow towards the hot side of the liquid-gas interface. Furthermore, the temperature gradients together with gravity will cause density difference within the fluid phase. Those will results in a convective flow, that is directed form cold to hot at the bottom of the compartment, however, at the surface it will point from the hot towards the cold side of the chamber. The density differences additionally lead to difference in surface-tension of the water at the interface to the gas phase, with decreasing surface-tensions towards the hot side. This can induce a so called Marangoni-flow that is like the convection-flow at the interface directed towards the cold side [15, 66].

All together, those effects will cause a continuous evaporation-condensation cycle with a net flow pointing towards the warm side of the liquid-air interface. This not only leads to an up-concentration of dissolved molecules at this location, but also to a periodically changing height of the interface within the closed compartment. As a result, on the hot side of the interface, molecules will first accumulate to the net flow in the fluid phase and then start entering the dry state due to the retracting liquid-air interface as evaporation moves more water molecules to the gas phase. As soon as the condensing liquid droplets forming on the coll sides are large enough, they will fall back into the liquid and rise the interface up again

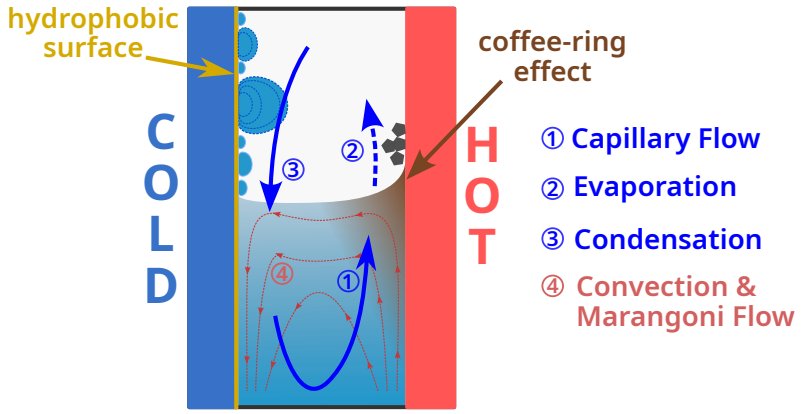

Figure 2.5: Temperature gradient across a narrow pore. The air-water interface within a temperature gradient is experiencing several effect in a confined compartment. Evaporation and the subsequent coffee-ring effect will lead to a net flow of dissolved particles towards the hot side of the interface, where molecules will accumulate dry to the lowering liquid surface. Evaporated liquid will condense on the cold side and eventually drop back into the liquid, raising up the interface and redissolving the dried molecules. This induces dynamic conditions that will repeat periodically.

and the dried molecules will go back in solution and the cycle starts again. This creates a highly rapid dynamic that additionally allows, depending on the magnitude of the temperature gradient, fast cycles between the wet and dry state of the solutes. Technically, also thermophoresis could play a role in a setting like this, adding a flow from hot to cold side, however, the dimensions of the chamber chosen in the experiments within this thesis are rather large (500 µm thickness), so that the effects of thermophoresis would be negligible [67].

Chapter
3

Quasi-2-dimensional Recreation of Alkaline Hydrothermal Vents

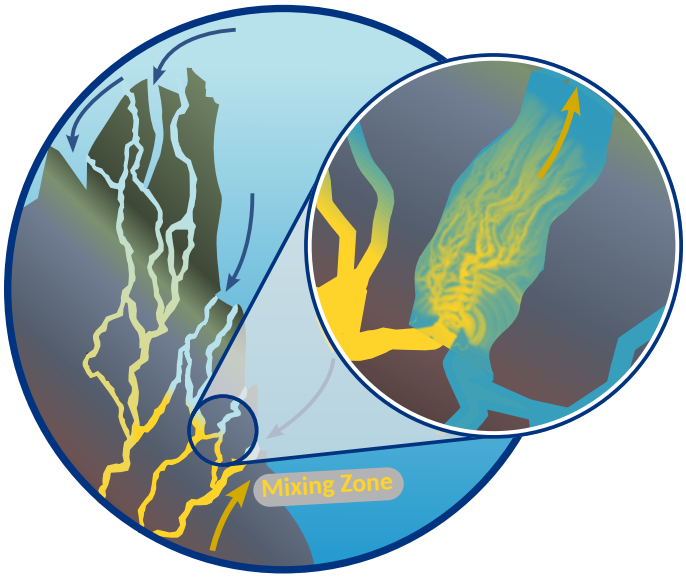

Summary: Alkaline Vents are considered a promising location for early processes hypothesised for the emergence of life as they have the potential to generate steep gradients across inorganic mineral membranes. This unique setting provides conditions that can help the accumulation of dispersed particles, boost chemical reactions and provide a platform for early forms of compartmentalisation. Past laboratory recreations of alkaline vents focused on the 3-dimensional chimney-structures, which prevented any kind of visualisation of emerging gradients and also made it hard to realise experiments in low volume.

At this stage, formation of alkaline vents in confined spaces and under variation of physical parameters are modelled by injection of alkaline fluid into an acidic, iron-rich solution prefilled into a thin, microfluidic chamber. Hence, the first part of this chapter describes the morphology of mineral precipitation in quasi-two-dimensions and tests their capability for the formation of gradients and accumulation of fluorescent bead particles [1]. The second part, the addendum shows supporting experiments that demonstrates the stability against non-modelled parameters and first insight into further explorations [2].

Microscope imaging allows for the spatio-temporal visualisation throughout the mineral formation process. Together with pH dependent fluorescent dyes the analysis shows that

finger like precipitation patterns can aid the formation of microscale pH gradients and accumulation of dispersed particles.

3.1 Introduction

When it comes to the search for a possible location for the origin of life on an early Earth, alkaline (hydrothermal) vents are a promising candidate as they provide several conditions beneficial for early processes facilitating the transition from abiotic to biotic matter [25–27] and might even be the location of the oldest ever found microfossils [2]. For this project, the main focus lies on the dynamic microfluidic environment that has the capability of creating channels by mineral precipitation [30, 34, 68]. In a prebiotic scenario, their formation is predicted to have created complex flow networks as soon as ion-enriched sub-seafloor fluid comes into contact with slightly acidic and ferruginous ocean water [27, 45, 48, 52]. On the other hand, the precipitated minerals act as a semipermeable barrier between the fluids [31, 51, 69], allowing the generation of steep gradients in temperature, pH and redox potential [23]. Fluid dynamics together with the non-equilibrium settings have the potential to accumulate dissolved molecules manifold from the fluid stream [11, 14, 70], which can then in turn be localised by adsorption to the mineral surfaces [71] to further participate in continuing molecular reactions. The close proximity to the geological material can even provide catalysing effects [28, 32] while the ongoing fluid flow feeds in new nourishment [24]. The unique setting of a mineral membrane separating different pH regions, resembles the structure of a modern autotrophic cell [26, 31]. In the same way the vent precipitates could act as a chemical reactor for organic synthesis reactions [24–26, 34, 51]. The cooperation of all those different features make alkaline vents especially interesting for catalytic inorganic reactions, replication and polymerisation [12, 13, 23, 72].

From modern alkaline vents like the Lost City Alkaline Vent Field, it has been observed that the precipitates usually grow into their characteristic tubular structure, when alkaline, ion-enriched fluids from cracks in the seafloor are exhaled into the bulk ocean water [30, 43]. Upon contact of the two fluids, minerals start to precipitate and form hollow, chimney-like cylinders around the alkaline fluid stream [26, 32]. In contrast to the ocean nowadays, is it suggested that prebiotic oceans have been more acidic [25, 53, 54] and anoxic as well as rich in dissolved iron(II) [51, 52, 73]. This makes the vents at Lost City still a model by structure, however, not by chemical composition as acidic prebiotic seawater [25] would have prevented the crystallisation of their characteristic acid-soluble minerals [43]. Past attempts to recreate those alkaline vent processes in the lab have used flasks with larger volumes of ocean solution with injections of alkaline fluid [23, 34, 68]. This approach managed to recreate miniatures of the vent precipitates, however, resulted in usually in several millilitres

[1] The results presented the first part of this chapter are published by Weingart et al. in *Science Advances* [60].
Authors: Maximilian Weingart, Siyu Chen, Clara Donat, Vanessa Helmbrecht, William D. Orsi, Dieter Braun, Karen Alim
Contributions: M.W., D.B., and K.A. designed the experiments. M.W., C.D., and S.C. performed all experiments. V.H. and W.D.O. developed the sample composition and gave major input on geological interpretation. M.W., S.C., V.H., W.D.O., and K.A. analysed the data. K.A. and D.B. supervised the project. M.W. wrote the manuscript, and all authors commented on the manuscript and contributed to the writing process. All authors edited and reviewed the manuscript for resubmission.

[2] The experiments investigating the trapping and accumulation of particles or molecules are still part of ongoing collaborative work with Mona B. Michelsen, Karen Alim and Dieter Braun.

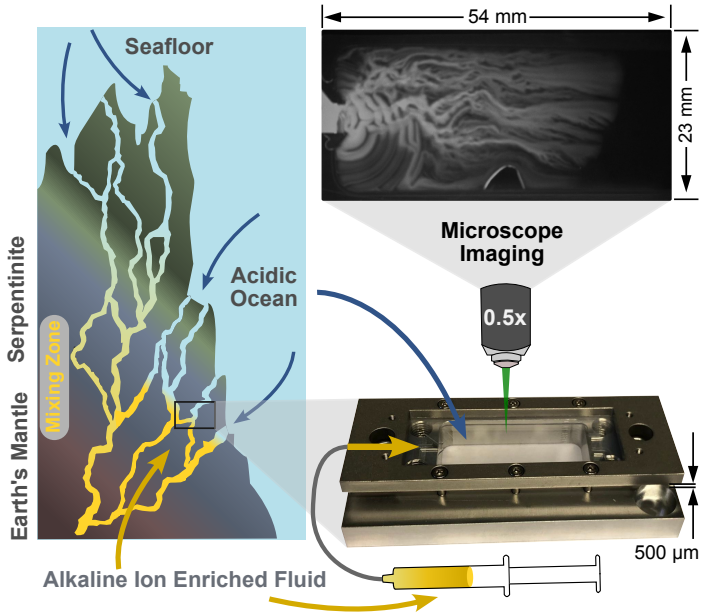

Figure 3.1: Alkaline vent precipitation in confined geometry. Alkaline vents emerge when acidic ocean waters fills narrow fractures in the seafloor where interaction with the surrounding rock enriches the water in ions and leaves it strongly alkaline. Upon contact of the enriched fluid with the ocean water, rapid mineral precipitation sets in. Narrow pores in the seafloor are simulated by a microfluidic chamber of 500 µm thickness. Alkaline fluid is injected in to the rectangular geometry, pre-filled with a ferruginous ocean simulant. Upon contact of the fluids, mineral precipitation forms different morphologies depending mainly on inflow-rate and OH^--concentration. Real-time monitoring of the precipitation process and morphology formation is achieved by microscope imaging. Fluorescent and universal pH dyes allow the observation of emerging gradients. Figure reprinted with permission from [60].

of 3-dimensional chimney systems, that were hard to observe in detail and even harder to use with small amounts of organic compounds [23, 74]. Thus, any kind of visualisation is prevented and so the study and visualisation of essential morphology and the role of their fluid dynamics for prebiotic reactions has been missing.

For similar experiments in a broader context, but not limited to geological analogues, the field of chemobrionics is dedicated to such laboratory precipitation experiments [58]. So called chemical garden experiments study growth and organisation of precipitates and crystals from solutions of different chemical composition and physical boundaries [58, 75]. The major interest here lies not only on the resulting morphology with structural patterns of crystals and precipitates but also their colour. As the emergence and growth of those structures builds one of the simplest forms of a self-organised system, it is not surprising they had already been picked up by origin of life researchers early on, due to the close resemblance of their dynamic behaviour to living systems [58, 75, 76]. However, the importance of chemical gardens for the emergence of life came only back, when NASA started to study them as alkaline vent analogues in the lab [34, 68]. Although they only considered 3-dimensional precipitates so far, the chemobrionics field established the research on quasi-2-dimensional structures, which not just opened a completely new perspective to the observation of pat-

terns, but also started to shift the experimental settings to microfluidic devices with low volume [69, 77, 78]. Most commonly used, are so called Hele-Shaw flow cells, that enable the injection of fluids into thin confined layers [79]. The structure growth is mostly driven not only by precipitation and crystallisation, but also by fluid advection through active pumping [77, 80, 81], convection or even osmotic pressure [82, 83]. None of the quasi-2-dimensional approaches, however, has been used as a recreation of an alkaline vent-like environment for the origin of life so far.

The branch of researchers studying the potential origin of life in alkaline (hydrothermal) vents, usually starts from an metabolism-first approach [24]. This assumes, that a metabolic activity of life's precursor molecules was established before the ability to replicate information storing molecules [24, 25, 38]. In this scenario, alkaline vents are especially interesting, because of their similarity to modern autotrophic cells, featuring an alkaline interior that is separated by a membrane from an acidic exterior [26]. With the minerals acting as a similar semipermeable barrier the difference in pH creates a proton gradient [26, 31], so that the the vent morphologies can act as an electro-chemical reactor and provide a precursor setting for CO_2 reduction similar to simple single-celled organisms [26, 73]. Experimental evidence, however, focused mostly on the structural base for this hypothesis [24, 25] and recent publications showed only low yields for organic synthesis reactions [34, 73, 84]. Thin mineral membranes, on the other hand, have been studied in microfluidic devices before, but only in controlled laminar flow regimes that only produces single straight membranes [31, 73, 85–87]. The approach described here is intended to provide a two-dimensional representation of the three-dimensional model to study the contact area between the two fluids.

The quasi-two-dimensional approach applied here, uses a rectangular chamber of 500 µm thickness. The microfluidic chamber itself is essentially built form a Teflon sheet with rectangular cutout that is squeezed tightly between two sapphire plates to allow optical access. The whole setup is placed horizontally on the stage of a microscope and the chamber filled with an acidic ferruginous solution to mimic the Hadean ocean water. To simulate the alkaline fluid that is exhaled into the ocean, a sodium hydroxide solution is injected into the pre-filled chamber with a syringe pump. In this setting, it is possible to image the precipitate formation in real-time with bright-field or dark-field microscopy to study the processes upon contact of the two fluids in a 2D representation.

The following results show, that the microfluidic chamber allows the visualisation of pH gradient formation in different emerging precipitation morphologies. The precise control of physical boundaries enables the study of different parameters, mainly flow-rate and concentration of the fluids, on the resulting morphology. The variation of different parameters and settings shows that stable finger-like precipitates are predominantly created at medium concentrations and inflow-rates, allow for micro-scale gradients in pH and offer the prerequisites to maintain them over longer times. Additionally, those mineral patterns are also capable of accumulating dispersed particles and concentrate them on the reactive mineral surfaces from a diluted flow. Those quasi-two-dimensional alkaline vent recreations, can fit into two plausible scenarios. On the one hand, they can be seen as a simplified model for the geological analogue, that provides a precise control of the emerging structures while allowing full optical access. On the other hand, it can also simulate a potential mixing of alkaline and ocean fluid in the cracks and pores of the seafloor, even before the alkaline fluid is exhaled into the bulk ocean water. Since this scenario might be hard to probe in on the sea floor, the setting described here provides a way to test all kinds of chemical reactions under different physical boundaries in low-volume in the lab.

3.2 Results

The following experiments are based on the usage of a thin microfluidic chamber to mimic the mineral precipitation in hydrothermal vents. The flow cell has a rectangular shape of 54 mm by 23 mm with a thickness of only 500 µm. Due to this confined geometry, the resulting structures are of a quasi-two-dimensional nature and give not only a flat representation of the three-dimensional example, but might also serve as a model for mineral formation processes in narrow cracks in the sub-seafloor rock. In order to facilitate the precipitation, the rectangular chamber is prefilled with an acidic ocean analogue and a high-precision syringe pump injects an alkaline fluid at a predefined flow-rate. This setting provides full optical access to visualise the spatio-temporal formation of mineral morphologies in real-time. In order to study the emergence and stability of pH gradients, pH sensitive dyes are mixed into both of the two fluids. For that purpose, either universal pH indicator or the pH-dependent fluorescent dye BCECF are used.

3.2.1 Precipitation Morphology under Parameter Variation

The first experiments assessed the influence of the physical parameter space on the structure of the resulting mineral precipitates. The results showed, that the predominant influence on the morphology comes from changes in the inflow-rate and concentration of the alkaline fluid injected into the flow-cell. In all those experiments, sodium hydroxide was used as an alkaline fluid, which means that changes in concentration directly correspond to changes in alkalinity of the fluid, i.e. its pH value. In this way, by changing the concentration of NaOH, also the pH difference between alkaline fluid and acidic ocean changes. However, altering the concentration of $Fe(II)Cl_2$ in the ocean fluid, appeared not to affect the general nature of the emerging patterns, and was therefore not further considered. Neither did the thickness of chamber under variation between 250 µm and 1500 µm and was fixed at 500 µm. In **Figure 3.2** the resulting morphologies for the variation of flow-rate and hydroxide concentration are shown.

The parameter ranges have been define by the boundaries, at which further alteration of the value, i.e. increasing at the upper end or decreasing at the lower end, will not affect the structure anymore. These gave the limits of $0.2 - 10\,\mathrm{mL\,h^{-1}}$ for the flow-rate Q and $0.2 - 1.0\,\mathrm{M}$ for the concentration c of injected sodium hydroxide. The snapshots of the microfluidic chamber have been chosen so that the morphological steady-state is captured. Further inflow of the alkaline fluid would not significantly change the structure of the mineral precipitates any further.

All combinations of those two parameters result in the formation of a diverse range of different precipitation morphologies. Amongst the different structural patterns, three dominant morphologies can be characterised (see **Figure 3.2**): Layers/rings, precipitation fingers and flow fields. On the upper end of the parameter space, at high concentration and flow rate layers/rings emerge as soon as the alkaline fluid comes in contact with the ocean and propagate layer by layer as more fluid is injected. These layered precipitates feature strong and thick precipitates, pushing back almost all of the ocean solution and leaving mostly alkaline fluid and minerals left in the chamber. On the lower end at slow influx and low inflow concentration flow fields form as wide and slowly intermixing areas of the two fluids. This is due to only weak precipitation. In the middle between the two limiting cases, the formation of precipitation fingers is predominant. They appear as almost parallel structures along

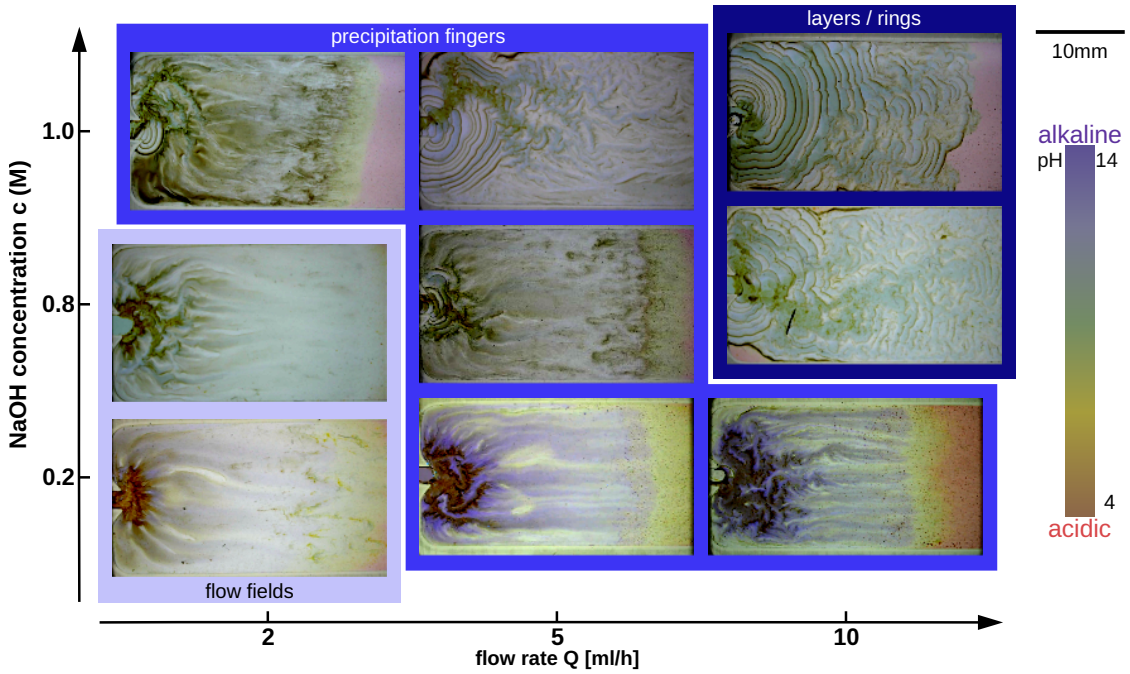

Figure 3.2: Morphology formation under parameter variation. Changes in inflow rate Q and concentration c of the NaOH solution injected into 200 mM $Fe(II)Cl_2$ result in different sets of precipitation morphologies. Study of both parameters within their respective limits revealed mainly three different types of structures. At the lower end of both parameters diffusive fields form, layers/rings emerge at the higher end. Medium flow rates and concentrations produce precipitation fingers capable of generating pH gradients across a mineral barrier between the inflowing alkaline solution within and the ocean fluid trapped between the fingers. In the layer/ring structures almost all ocean fluid is pushed out by the precipitates, whereas fluids in the flow fields keep mixing by diffusion across the weak precipitates. Neither of the two structures forms or maintains stable gradients. Figure adapted from [60].

the inflow vector and maintain stable precipitation morphologies. The experiments show, that the higher concentration and flow-rate of the injected solution, the faster precipitation happens and the stronger the precipitates are, as more ions are provided or fed during the process. Higher flow-rates also result in strongly advection dominated propagation of the fluid as it enters the chamber. The lower the flow-rate gets, the more diffusive behaviour can be observed. This concerns not only the initial inflow-rate, but also changes in flow-rate due to effects inside the chamber, e.g. hindrance by already formed precipitates. As the name already says, diffusive fields are mostly governed by diffusion rather than advection. Even after the fluid inflow reached the end of the chamber, intermixing of the two fluids still continues through the thin and weak precipitates. Because of that, flow fields take the longest time to arrive at a steady state. A more detailed view characterisation of the different formation times will be shown in the next section.

3.2.2 Time Evolution of Precipitates

Controlling inflow rate and concentration of the fluid has a direct influence on the speed of precipitation and of course also on the advection/propagation of the influx. The three different main morphologies identified in the previous experiments form on different time-scales, subsequently after each other. This means that variation in the experimental parameters essentially corresponds to change in the formation timescale. In **Figure 3.3** different time-steps are shown for three different experiments, each of them dominated by one of the three morphologies respectively. For better visualisation of acidic and alkaline areas, the fluids are mixed with a fluorescent pH dependent dye [2',7'-bis-(2-carboxyethyl)-5-(and-6)-carboxyfluorescein (BCECF)] that stains alkaline areas whereas acidic ones appear dark. Considering the experiment that is dominant by layers/rings (**Figure 3.3 left**), it can be seen that those structures form within the first $10 - 15$ s. In this case, the morphology is not only the dominant one, but also the only one as it persists until the chamber is completely filled.

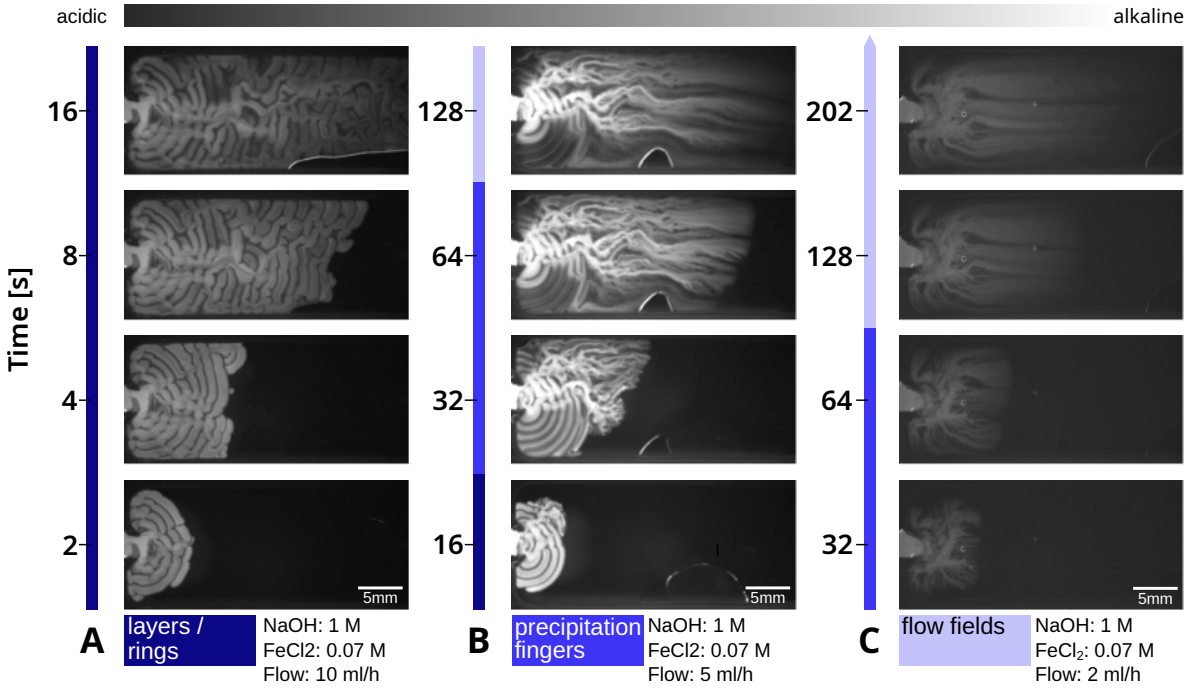

Figure 3.3: Time evolution of different morphologies. Three different experimental conditions (A-C) show the dominant formation of one morphology each by using the pH-dependent fluorescent dye BCECF. In each experiment snapshots of roughly the same chamber filling have been chosen to show the progression of the morphologies over time. Layers/rings form within approximately 20 s (A), precipitation fingers emerge between 30 s and 80 s (B) and flow fields can be observed after around 100 s (C). Artefacts of other morphologies can be seen in experiments B and C, however confirm the formation time-scale of the respective structure. Therefore a change in the experimental conditions corresponds to a shift in the formation time-scale shown in the chamber. Each of the identified morphologies therefore has their characteristic time-scale. Figure adapted from [60].

The same initial time-scale can be seen in the mid-regime experiment (**Figure 3.3 middle**): In the beginning layered/ring-like precipitates appear until approximately 30 s. After that, the fluid-stream splits into multiple smaller channels that start creating the characteristic

precipitation fingers between $30 - 80$ s that dominate the morphologies in this experiment. These continue growing towards the end of the chamber with ongoing injection, however, with increasing time the forming precipitates get weaker and start diffusing perpendicular to the flow-trajectories until they reach the end of the chamber after around 130 s. In the last experiment (**Figure 3.3 right**), a similar scaling behaviour can be observed: In the beginning 120 s weak, finger-like precipitates start to form, which then start to spread out diffusively as the precipitation diminishes and the flow fields start to dominate the morphology.

The comparison of multiple time-steps under different inflow rates and concentrations of OH^--ions shows that variation of these parameters also shifts the time-scale for the mineral precipitation. Each of the morphologies, layers/rings, precipitation fingers and flow fields, thereby needs an increasing time-range to form as the dominant structure amongst the precipitates. However, the emergence time-scale of each morphology individually, seems to be almost invariant under changes in the experimental conditions, as the certain morphologies could also be observed within their formation time in experiments dominated by another morphology. The formation of specific patterns in this confined geometry is therefore time-dependent.

3.2.3 Fluid Flow and Stability of pH Gradients over Time

The use of an fluorescent pH dye (**Figure 3.3**) not only allows the mapping of high and low pH areas, it also helps in tracing the fluid flow during the formation of the precipitates. The flow trajectories of the injected fluid are an important marker for the formation of the morphologies, but even more important for the assessment of the pH gradient formation and their stability over time under continuing influx. In the layer/ring structures, even though they form gradually layer by layer, after some time the main flow finds its way as a shortcut through all the rings. As a consequence that the fluid is then no longer tracing its initial way along all the layers, the fluorescence signal dims in the areas further away from the main flow. This might be due to ionic interaction of fluid an precipitates and leads to a difference in fluorescence signal between the main flow and the outer areas of the rings. The precipitation fingers on the other hand, this effect does not occur, since the flow is not tracing one consecutive path, but rather divides in to multiple sub-flows across the width of the chamber instead. This manifold of flow trajectories traces out the finger-like structure parallel to the direction of the overall fluid propagation. Therefore the constant inflow does not bypass the earlier formed precipitates of the precipitation fingers, but maintains the fluorescence and in turn also the pH gradients. Although the flow fields show a similar initial division into several sub-flows, the fluorescence diminished over time as the alkaline fluid diffuses into the remaining ocean liquid. Because of the weak and thin mineral precipitates, this diffusive mixing behaviour continues until the fluorescence and thus, all initially observed gradients are equilibrated.

In order to evaluate the potential of each of the three morphologies to form gradients, the final images of the time evolution (**Figure 3.3**) are further analysed in **Figure 3.4**. Therefore the fluorescence signal of a cross-section over the chamber width is plotted over time for each structure respectively. In the layers/rings structure strong and stable precipitates are formed, however, they do not provide any setting for the emergence of stable pH gradients. Since the precipitates take up the whole width of the chamber and fill it gradually form bottom to top, the whole acidic ocean fluid is either reacting with the alkaline fluid to form precipitates or is pushed out of the chamber as the precipitates grow. Gradients that appear

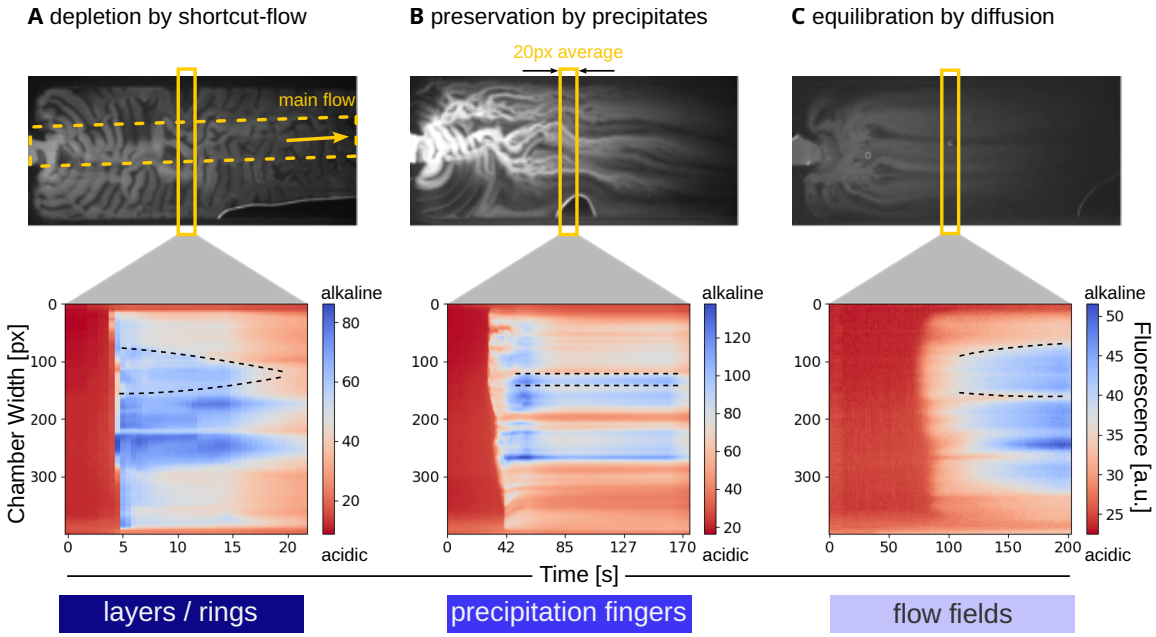

Figure 3.4: Stability of pH gradients over time. In the experiments (A-C) shown in **Figure 3.3** 20px are averaged over the the width of the chamber and plotted over time. In the layers/rings (A) a shortcut-flow establishes through the layers establishes in steady-state, leading to fading fluorescence in the outer areas of the rings. Narrowing blue (alkaline) areas show that gradients are not stable. Precipitation fingers (B) straight blue lines of constant width show stable gradients over time between red (acidic) and blue (alkaline) regions. Flow fields (C) intermix by diffusion over time (widening blue areas), hence neither stable gradients nor a steady-state are reached. Figure adapted from [60].

to form between the shortcut-flow and the outer areas of the rings as it can be seen by the fluorescence difference in the top part of **Figure 3.4 A** are only of very weak and short-lived nature. As the areas are in direct connections to the shortcut-flow without a mineral barrier separating higher and lower pH regions, the pH gradient would not be maintained and will eventually fade by diffusion. The bottom part of **Figure 3.4 A** in a similar manner, also the flow fields are not capable of producing stable pH gradients. As already mentioned briefly in the previous section, the morphologies do not reach a steady-state within the course of the experiments and, thus, the the two fluids are perpetually mixing by diffusion across the weak precipitates until a homogeneous pH in the chamber is reached. In the fluorescence image, this is clearly indicated be the blurred edges of the alkaline (light) areas (no sharp transition between high and low pH). In **Figure 3.4 C** the cross-section over time plot confirms this by the broadening of the alkaline (blue/white) section to an almost uniform pH at the end of the experiment. Amongst the three structures, precipitation fingers seem to be the only morphology that exhibits steady gradients. The fluorescence images show clear and sharp edges between the finger structures and the acidic ocean solution around them. This indicates a strong pH gradient in between the two areas that are separated by stable mineral precipitates. The minerals form a semi-permeable membrane separating alkaline and acidic regions while the constant influx keeps feeding OH^--ions to maintain the gradient. The time-dependent plot in **Figure 3.4 B** shows sharp and straight blue lines that persist

even after the morphology reaches a steady-state. From their emergence after around 30 s, they persist at at constant width of alkaline (blue) channels surrounded by acidic ocean fluid (red).

The evaluation of the different experimental settings for the alkaline vent precipitation in a confined geometry showed that a sufficient generation of steady gradients was only provided at medium concentration and flow of alkaline fluid in the emerging precipitation finger structure. In comparison with modern autotrophic cells, a quite similar compartmentalisation can be seen, as also an alkaline interior is separated form the acidic exterior by a permeable membrane. In contrast to the confined alkaline vent setting, however, a cells needs an active mechanism to pump protons across the membrane and maintain the gradients. The precipitation finger structures keep the gradients up as long as the the influx keeps feeding in OH^--ions with the alkaline fluid.

3.2.4 Accumulation of Dispersed Particles in Different Morphologies

In order to test the capabilities of the different confined alkaline vent morphologies for accumulation and concentration of dispersed particles, fluorescent beads were added to the system. Three different experiments were conducted, each of them representing one of the morphologies as the dominant precipitation structure. To simulate dispersed particles, fluorescent beads of 10 µm diameter were mixed in the injected alkaline fluid. **Figure 3.5** shows the fluorescence signal of the beads across the chamber for ∼30 % chamber filling (left) and the steady state (middle). On the right side the average fluorescence intensity of a selected region of interest (ROI) is plotted over time for each of the experiments. The ROI has dimensions of 100 × 50px and had been positioned so that a characteristic area for each morphology is shown. More intense fluorescence suggests a local accumulation of beads in the mineral structures.

For the flow fields **Figure 3.5 A** the overall fluorescence signal is rather weak and mostly uniform across the whole area. This suggests scarcely accumulated beads due to the weak precipitates and gradients. Some increase fluorescence at the lower end of the chamber seems to stem from the stronger precipitates in the beginning before transitioning to the flow fields (cf. also **Figure 3.3**).

In similar manner, also the layers/rings (**Figure 3.5 C**) show some higher fluorescence signal in the beginning, which could be explained with the higher inflow rate, but also very likely with the beads getting trapped in the grooves of the rings. Although the intensity plot shows an increase of fluorescence in one of the groves, but the slope is rather unstable and and flat. The increasing fluorescence, however, has two limitations: On the one hand, the beads are likely flushed out again, which is also supported by the fading fluorescence over time. On the other hand, trapped beads in the grooves or precipitates would not be subjected to any gradients as soon as the shortcut-flow established through the layers.

For the precipitation fingers (**Figure 3.5 B**) it also seems that some beads are accumulated during the precipitation process, suggesting an incorporation of the beads in the mineral material. In contrast to the other structures, however, these initial aggregates are not fading over time, but rather increase even further in fluorescence over time. This is also confirmed by the steep increase of the slope in the fluorescence plot and the stable plateau, persisting after the maximum intensity is reached. In this way, the ongoing influx seems to feed in new particles that are getting trapped and lead to a localised and enhanced concentration of the formerly dispersed particles.

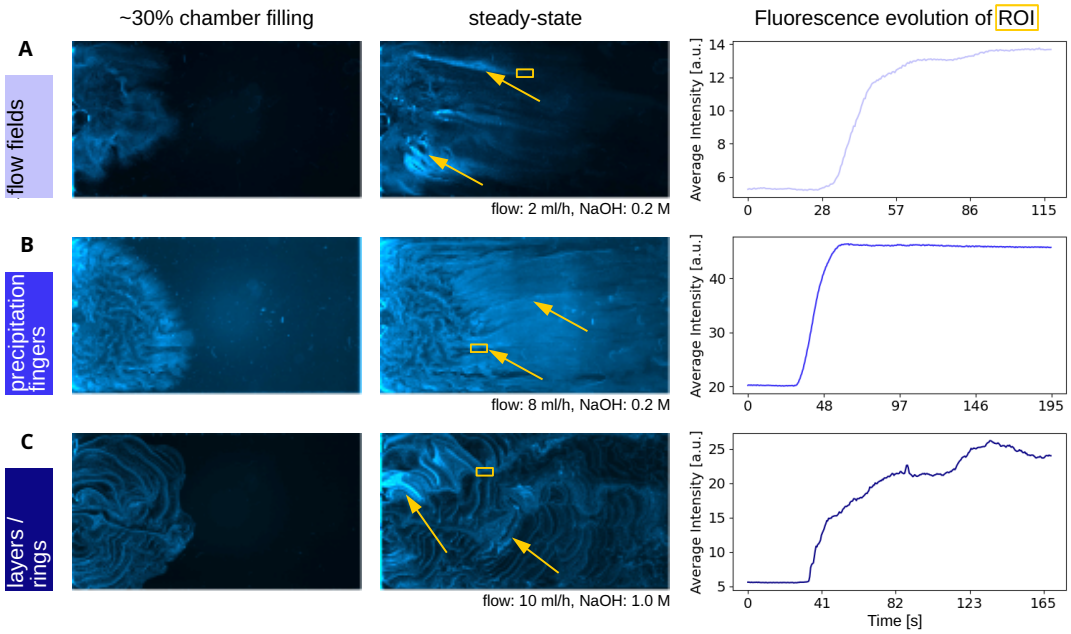

Figure 3.5: Accumulation of beads in mineral precipitates. Fluorescent beads of 10 µm are mixed into alkaline fluid and ocean solution. Snapshots of the experiments at ∼30% chamber filling and in steady state as well as a plot of the average intensity of selected regions of interest (ROI) show increased fluorescence in the resulting morphologies (A-C). Flow fields (A) show only weak fluorescence and mostly uniform across the chamber suggesting only scarce accumulation. Precipitation fingers (B) exhibit the strongest increase in local fluorescence and therefore probably the strongest accumulation. Layers/rings (C) also show locally increased fluorescence in the grooves. Accumulation can either be due to incorporation of beads during the precipitation process or later trapping from the stream. Figure adapted from [60].

3.3 Materials and Methods

The centrepiece of the experimentation on confined alkaline vents is a custom built microfluidic chamber (**Figure 3.6**) that allows the creation of thin quasi-2-dimensional flow-cells. This setup enables the precise sizing of thin chambers of custom shape and dimensions, provides inlets for fluid injection or extraction while maintaining full optical access by fluorescence and bright-field microscopy.

3.3.1 Microfluidic Setup

The microfluidic flow-cell used in the experiments consists of a rectangular chamber with dimensions of 16 mm × 40 mm and a thickness of 500 µm. In order to provide a uniform and precise thickness of the chamber, the rectangular geometry is cut out from a Teflon sheet (fluorinated ethylene propylene, FEP) of 500 µm thickness using a computer controlled cutting plotter (CE6000, Graphtec, Japan). The geometry is therefore supplied as two-dimensional sketch (**Figure 3.6 C**) created with the aid of a CAD software (Inventor 2021, Autodesk, USA). The sealed chamber is created from the Teflon sheet cutout by pressing it tightly between two transparent sapphire slides (22 mm × 60 mm). The assembly of the whole cell is shown in **Figure 3.6**. The top sapphire (1.0 mm thickness) is held in place by a steel frame that also

presses the three layers together by mounting them onto an aluminium base with six screws (M2) tightened to 16 mN m. Microfluidic access to the structure in the Teflon sheet is provided by four drilled holes in the bottom sapphire (0.5 mm thickness) that overlap with four threaded holes in the aluminium base. To access the chambers interior channels in the cutout of 1.7 mm are guided from the rectangular structure to the the points that overlap with the holes in the sapphire in the final assembly. Teflon tubing (polytetrafluoroethylene, PTFE) with 180 µm inner diameter are then connected via low-pressure fittings and ferrules to the threaded holes in the aluminium base and allow to inject or extract fluid to or from the chamber.

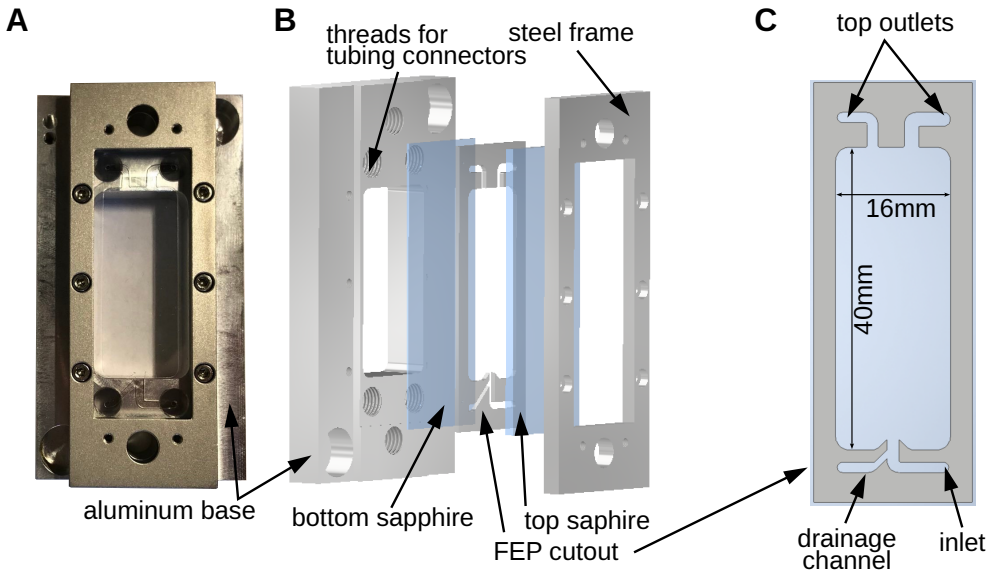

Figure 3.6: Assembly of the microfluidic flow-cell. Top view (A) and explosion scheme (B) show the steel frame that is screwed onto an aluminium base to press together the chamber assembly. This is formed by a two-dimensional cutout from an FEP-sheet (C) that is sandwiched between two sapphire plates. The cutout forms a rectangular chamber with 4 channels connecting to it. Four holes in the bottom sapphire overlap with the end of the channels in the cutout as well as the threaded holes in the aluminium base to allow microfluidic access to the chamber by connecting tubings with corresponding screw connectors. Figure reprinted with permission from [60].

For the conduction of the experiments the chamber is prefilled with an acidic solution to simulate a prebiotic ocean. Therefore, the inlet and drainage channel are tightly closed by putting end-caps on the connecting tubing in order to avoid ocean fluid penetrating the channels. Any residue of ocean fluid in the inlet channels could later on cause immediate precipitation upon contact with he alkaline fluid within the channels and block them for any further injection. Prefilling is then accomplished by hand using a 1 mL glass syringe and one of the outlets. The second outlet is left open for pressure balance and tilting with slight shaking of the whole setup during the filling process, ensures that the rectangular chamber is uniformly filled without enclosing any air pockets or bubbles.

The injection of the alkaline fluid is done using a pulsation-free, continuous-flow syringe pump (Nemesys S, Cetoni, Germany) with glass syringes (1 ml, SETonic, Germany). To prepare the prefilled chamber for the injection experiment, the two outlet channels are initially

sealed after the ocean solution has been filled in. One syringe is filled with the alkaline fluid and connected to the the inlet channel and another empty syringe is connected to the drainage channel. Injection of alkaline fluid is then started at a low flow-rate of around $2\,\mathrm{mL\,h^{-1}}$ to minimise the dead volume. At the same time, the empty syringe is set to retrieve at a flow-rate between $1 - 2\,\mathrm{mL\,h^{-1}}$ to remove the remaining air from the tubings, but avoid sucking the fluid into the drainage channel. Operation of all syringes is stopped, when the fluid front can be seen in the inlet channel close to the chamber at a distance of approximately 2 mm to the ocean fluid inside. The drainage channel is then closed tightly and both of the outlet channels are opened to collect potentially overflowing liquid at the end of the chamber. Image acquisition and injection at the required flow-rate can then be started.

3.3.2 Microscope Imaging

Due to the fully transparent setup of the flow-cell, it can be imaged with fluorescence microscopy with illumination from the top as well as bright-field microscopy with illumination from below. The whole chamber is therefore placed on the stage of a microscope (Axio Zoom.V16, Carl Zeiss, Germany) with the aid of a 3D-printed support stand. The microscope features a built-in source of white light for illumination from below the specimen platform in bright-field mode. For fluorescence imaging on the other hand, the chamber is illuminated from above by white light form a light engine (SOLA 80-10247, Lumencor, USA) passing through a filter-cube (38 He, Carl Zeiss, Germany). This creates the necessary wavelength of 470/40 nm for the excitation of the used fluorophores. In order to image the complete interior of the rectangular chamber (16 mm × 40 mm) and objective lens with 0.5× magnification is used. Depending on the experiment, image acquisition is either carried out by microscope camera with complementary metal-oxide semiconductor (CMOS) sensor (ORCA-Flash 4.0, Hamamatsu, Japan) for fluorescence or greyscale bright-field imaging or a photographic mirrorless camera (Lumix DC-G100K, Panasonic, Japan) with a C-mount adaptor for colour based imaging of samples containing a universal pH dependent dye.

3.3.3 Sample Preparation

For each experiment primarily fresh stocks were prepared for the acidic ocean solution and the alkaline fluid. Sodium hydroxide [NaOH] (Carl Roth, Germany) was used as alkaline fluid as shipped as a volumetric standard solution (1 M) or diluted in nuclease-free water (Ambion, Invitrogen, Thermo Fisher Scientific, USA) to get concentrations of 0.8 M and 0.2 M. Stock solutions for the ocean analogue were mixed by dissolving grains of iron(II)chloride tetrahydrate [$Fe(II)Cl_2 \cdot 4\,H_2O$] (Sigma-Aldrich, USA) in nuclease-free water. The amount of iron-chloride was adjusted to give the desired concentrations of either 0.075 M or 0.2 M. Since oxidation of iron(II)chloride starts quite rapidly after contact with air, it was stored under inert gas (argon) and all flasks and vial have been flushed with argon gas prior to usage. Although complete oxygen-free conditions could not be provided in the chamber during the experiment, oxidation of the stock-solution was limited.

For visualisation the stock solutions for both fluids have either been mixed in a ratio f 8:1 with a universal pH indicator (KS90-UpHI, Lovibond, Tintometer, Germany), mixed 50:1 with a solution of 2',7'-Bis-(2-Carboxyethyl)-5-(and-6)-Carboxyfluorescein [BCECF] (Invitrogen, Thermo Fisher Scientific, USA) or used without further modification. The experiments showing the accumulation of dispersed particles and tracing the fluid flows used a 2.5%

aqueous suspension of 10-µm fluorescent (bright blue) carboxylate polystyrene microspheres (Fluoresbrite, Polysciences, USA) that was mixed into the sodium hydroxide solution in a volume ratio of 18:1.

3.3.4 Image Acquisition and Analysis

Image Acquisition with the microscope camera was done with the microscopes proprietary software (ZEN pro 3.2, Carl Zeiss, Germany) with exposure times of around 20 ms. After recording the images have been exported as either avi or mp4 for further processing and analysis. For image acquisition on the photographic camera the default movie recording mode was used to produce movies in mp4-format. The image-series mode could only save an image every ∼6 s and was therefore to slow for the dynamics of the morphology formation. To create the time evolution plots (**Figure 3.3** and **Figure 3.5**), the movies have been processed using ffmpeg to export a series of images. These have been analysed in Python-script to average either a line of 20px width over the cross-section of the chamber or a designated ROI and plot those areas over the duration of the movie as heatmap or 2D-plot respectively.

3.4 Discussion

The experiments studying alkaline vent precipitation processes in a confined quasi-two-dimensional geometry show that mainly three different morphologies are obtained. Variation of experimental parameters thereby identified the flow-rate and OH^--ion concentration (i.e. the concentration of NaOH) of the injected alkaline fluid as the key parameters responsible for the formation of different precipitation structures. Under the aspect of pH gradient formation, precipitation fingers seem to generate the steepest and steadiest gradients. Within the given parameter space they form strong precipitates at medium flow rates and medium concentration of NaOH. To create the characteristic shape, the main fluid-flow splits into multiple sub-streams creating finger-like precipitates that separate alkaline fluid streams from enclosed ocean solution in between. These pH gradients across the precipitates are even maintained after the morphological state is reached as the fluid stream keeps feeding hydroxide ions through the fingers. Stable and strong precipitates are also the key characteristic of the layers/rings, however, they do not appear to from stable pH gradients. The fluid flow gradually covers the entire area of the chamber, which leaves behind the strong rings of precipitated minerals, but on the other hand also excludes any remaining ocean solution, so that only alkaline fluid is left within the layers. All the rings are eventually bypassed by a short-cut flow that forms as a stream straight through all layers to the back of the chamber. Although there seem to be gradients between the outer sections of the rings and the main stream with fresh hydroxide, ions, but since those areas are not separated by any barrier, the gradients will not remain stable over time. Similarly it behaves with the flow fields: The precipitates forming are only very weak and not stable over time. In this way they not only never reach a morphological steady state, but also fail to maintain any gradients, as the fluids will just intermix continuously by diffusion.

Considering the time-evolution of the morphologies under variation of the experimental parameters, it can be seen that a change in the conditions corresponds to a shift of the formation time-scale of the dominant structure. Each of the three different morphologies form at a different time which seems invariant under the variation of flow-rate or concentration of al-

kaline fluid, therefore forming an characteristic time-scale for each of the structures. Layers and rings are forming within the first 20 s after starting the injections, precipitation fingers emerge between 30 and 80 s and after around 100 s the emerging structures are dominated by flow fields. In agreement with this observation, all experiments exhibiting a certain dominant structure, but running long enough so that multiple of the characteristic timescale are passed, also show artefacts of the respective other morphologies. For instance in the experiments dominated by precipitation fingers, Layers/rings emerge within the first few seconds of the experiments and similarly the precipitation fingers slowly transition into flow fields towards the end of the experimental run. Since the precipitation fingers appear to be the most promising structure for gradient formation, their formation can be promoted by the usage of medium inflow-rates and concentrations of OH^--ions. As in **Figure 3.3** the time-evolution appears to scale binary-logarithmic compared to the chamber filling. This might be linked to the fact, that the inflow-rates in the experiments roughly double for each structure.

Accumulation studies that used fluorescent beads mixed into the alkaline fluid, showed locally increased fluorescence signals in layers/rings and precipitation fingers only suggesting an up concentration of beads in the morphologies. Flow fields did not suggest any significant accumulation. The explanation for the accumulation could be bases on two possible aspects: On the one hand, beads can already be incorporated into the mineral structures during the precipitation process and thus be localised in the morphology. On the other hand, beads seem to be accumulated from the continued influx, which in turn suggest trapping by the advective flow through the established structures or diffusiophoretic movement [31] of beads towards the mineral structures. In the latter case, the localisation would then probably be aided by either adsorption to the minerals or exclusion from the flow. Highest beads accumulation in the layers/rings could be observed in the outer groves of the rings, where no gradients would be applied after the shortcut-flow establishes. The plotted fluorescence of one groove over time shows an increase in intensity, however, no stable and rapidly increasing slope as for the other two morphologies. This might be caused by fewer incorporation of beads during precipitation as the strong precipitates form only at the tip of the stream. Accumulation would then mainly stem from diffusiophoretic accumulation or hydrodynamic trapping, which seems plausible given the high flow rates and initially steep gradients before the shortcut-flow forms. This seems to appear differently in the plot for the precipitation fingers: as soon as precipitation sets in the fluorescence increases in a steady and steep slope until it reaches its maximum intensity. This is kept at a stable plateau almost without any variations till the end of the recording. Compared to the layers/rings the finger structures are forming less rapidly and in parallel to the flow vector. In this way precipitation might also happen slower, providing more time for beads to be incorporated in the forming mineral structures. The high stability of the maximum intensity, is another indicator for the stable precipitates and gradients. However, it might also be a hint, that beads are mostly localised by the precipitate formation and less through trapping by the gradients. Another explanation would be that both effects are contributing quite rapidly and the mineral surfaces are saturated quickly but keep the beads adsorbed over time. For the flow fields a ROI was chosen, so that the plotted intensity reflects an area, that is not part of the initial finger-like fragments of the experiments. Also here, the plot indicates a rapidly increasing fluorescence, however, a longer time with more jittering until the maximum is reached. Since, the experiments was not recorded longer, it cannot be concluded, if the intensity goes down again as the gradients equilibrate over time.

The precipitation reactions in the quasi-two-dimensional experiments could be similar to the ones happening in modern alkaline vents as the Lost City Hydrothermal Vent Field. While the experiments could potentially model the structure of the modern vents, they do not resemble them by chemical composition, as it would be more complex than the fluids used in the lab. The selection of chemicals for the microfluidic studies was done in order to simulate the crucial properties of precipitation upon contact of the two fluids of different pH, but at the same time keeps the composition as simple as possible and in a way likely plausible on an early Earth. The formation of specific mineral was not within the goal of the study. However, the observed minerals are likely and amongst others composed of fougerite and amakinate (green and white rust) as identified in the publication by Helmbrecht et al. [45], where an identical chemical composition has been used. Since in the microfluidic chamber provide perfectly oxygen-free conditions could not be provided, potentially formed white and green rust likely started transforming into some of their other ferric states by oxidation in air. Colour changes to slight orange several minutes after the experiment has stopped or even blackish (after several minutes to hours) suggest the slow transition to lepridococite and magnetite [88]. The microfluidic setup allows the study of many further geo-chemical compositions of either fluid and therefore the study of their precipitation in confined geometries. To get a closer similarity to Lost City type vents, the incorporation of carbonate [30, 43] could be particularly interesting. A first rudimentary attempt with carbonate, however, showed only impaired precipitation (**Figure 3.D.1**). Further investigation of the precise fluid composition and experimental conditions are required. In terms of prebiotic relevance, aside carbonate also sufide would be a promising candidate ([24–26]), especially because of their catalytic effect when incorporated in highly reactive metal sulfides like Fe(Ni)S minerals [34, 47, 89, 90]. In previous experiments, sulfide has not been included for safety reasons and the potential generation of H_2S gas. Apart form the incorporation of more versatile mixtures of ions, future experiments should also improve the extraction of the resulting minerals to characterise them with analytical methods like Raman spectroscopy or scanning electron microscopy.

Comparing the temperatures at which alkaline vents usually form, Lost City represents so called low-temperature alkaline vents systems. Nevertheless, the exhaled fluids commonly reach temperatures between 40 °C and 90 °C [30, 43]. The microfluidic experiments have been carried out at room temperature throughout, but tests with heated fluid confirmed that no notable change in morphology is induced at higher temperatures (**Figure 3.C.1**). Another considerable difference to to real-life alkaline vents is the direction of injection against gravity. Since the microscope setup limits the technical feasibility of vertical orientations of the flow-cell, all experiments show above have been performed in horizontal orientation, i.e. injection perpendicular to gravity and therefore limiting its potential influence. The vent formation process on the seafloor it vastly dependent on buoyancy differences of the two fluid, which is responsible for the exhalation of the alkaline fluid into the ocean. This process is simulated in the experiments by active injection with the syringe pump. Given the close density of the fluids used (**Table 3.B.1**), however, it suggests that buoyancy effects in a vertical orientation would be negligible.

Flat two-dimensional geometries have also been established in the field of chemobrionics to study precipitation patterns in addition to the common three-dimensional chemical garden experiments. In contrast to the setup used here, however, most of the researchers used radial injection of one fluid into another [69, 78, 79, 91, 92]. Despite the differences in injection and overall chemical composition of the fluids, Rocha et al. [79] obtained similar pattern as observed here under the variation of parameters. A quick testrun to check radial

injection into our microfluidic flow-cell (**Figure 3.A.2**) also showed a ring-like structure initially progressing in a spiral motion around the orifice. However, the radial injection stopped producing spiral patterns after some time as in the layers/rings morphology with injection from the side, a shortcut-flow established through the different layers. At the same time, our rings also did not form in a regular way es shown in [79]. After all, none of the the structures in the literature referenced above coincided completely with our morphologies. Therefore, the precise conditions used here, would also be interesting from the perspective of pattern formation and modelling.

All other attempts to recreate the formation process of alkaline vents in the lab have used three-dimensional recreation in larger bulk solutions of several millilitres [34,58]. Compared to this setting, the microfluidic chamber used here, offers the advantage to precisely control the shape and thickness of the chamber, while providing full optical access to the chambers interior with bright-field microscopy. At the same time, the flow-cell only requires a sample volume less than 100 µL and would therefore especially provide a setting to study the effect of gradients and catalytic mineral surfaces as present in alkaline vents [23, 45] on chemical reactions in low volume. The quasi-two-dimensional setting can be seen as a model representation of the three-dimensional example. However, it can also be seen as a potential geological scenario as the the precipitation process could possibly already happen in the narrow pores and fractures of the seafloor, even before the alkaline fluid is exhaled into the bulk ocean water.

In the context of origin-of-life scenarios, the quasi-two-dimension alkaline vent model provides several positive aspects that are assumed to be required an an early Earth. Gradients form the basis for modern life as we know it, as many crucial processes are based on non-equilibria settings across semi-permeable membranes [31]. Considering the basic structure of an autotrophic cell, it consists primarily of a membrane that separates the alkaline medium inside of the cell from from an acidic outside. The same topological arrangement can be found in alkaline vents, where semi-permeable mineral barriers separate the alkaline fluid stream form the surrounding slightly acidic ocean water (in an Hadean scenario) [26,31]. For this reason the alkaline hydrothermal vent theory on the origins of life suggests the structural arrangements such alkaline vents as a precursor to the basic structure of living systems, in which a metabolic interaction with the environment would be established prior to a replication mechanism of information bearing molecules [24]. Such a setting can also clearly be seen in the precipitation finger morphology, where the acidic fluid stream is separated by precipitated minerals form the more acidic ocean solution trapped between the finger-like structures.

Apart from forming a potential precursor setting to an autotrophic cell-like structure, this topology also features other advantages. In an early Earth scenario, it is usually assumed that any kind of molecule would mainly be present in a highly diluted solution of an extensive ocean. Any chemical reaction potentially boosting molecular evolution, however, requires high local concentration of reagent molecules, a discrepancy commonly referred to as the "concentration problem in the origin of life" [10]. As the precipitation fingers provide stable ionic gradients across the mineral barriers it could open the door for direct colloidal transport of dissolved species via diffusiophoresis [31]. Furthermore, the physical structure of the morphologies could trap macro-molecules form the fluid stream by entropical trapping in pockets or gaps in the mineral surfaces. Taking into account a potential temperature difference between the two fluids, dissolved molecule accumulation would probably be boosted even more by thermophoresis [70]. After initial accumulation, adsorption of (macro-

)molecules to the mineral surfaces [45, 59, 71] can prevent the their re-dilution and and even aid reactions by mineral catalysis [26, 28, 31]. In order to investigate local accumulation, potential separation of species or even local product formation, two-dimensional imaging with matrix assisted laser dissorption/ionisation (MALDI) could be applied to dried samples of the morphologies in future experiments.

In theory, the main principle how steep proton gradients could catalyse organic synthesis reactions is bases on their potential to reduce CO_2 in a similar way to the acetyl-coenzyme A pathway in bacteria or archea [26, 34, 35]. While this primarily would suggest aiding organic synthesis reactions, recent publications [34, 73, 84] could only observe organic products in low yields. Nevertheless, the setting is posing a promising location for chemical reaction networks as the mineral barriers allow strongly opposing conditions as high-low pH or oxidising-reducing moiety in close spatial proximity giving the potential to combine different or consecutive reaction environments and even aid in the product selectivity of amino-acid synthesis [23].

3.5 Conclusion

The experiments investigated the precipitation of alkaline vent like fluids in a thin confined geometry. Among the different precipitate morphologies obtain under parameter variation, finger-like precipitates at medium flow-rate and OH^- concentrations form and maintain pH gradients, while having the potential to accumulate dispersed particles from the inflow. The confined geometry can, however, not only be seen as a model for the three-dimensional scenario, but also also as a promising geological phenomenon, if mineral precipitation already occurs in the cracks and fractures of the seafloor.

The developed microfluidic setup therefore allows a precise spatio-temporal visualisation of the precipitation process. The full optical access enables the application of fluorescent or universal pH dyes to study gradient formation under the microscope. Additionally, it drastically reduces the volume required for recreations of alkaline vents in the lab and provides a mean to study the potential of the geo-chemical environment for the accumulation of organic molecules, catalytic reactions and processes like polymerisation or replication of biopolymers.

Addendum 3

3.A Microfluidic Flow Cell with Radial Injection

Many approaches in the field of chemobrionics apply radial injection into confined geometries such as Hele-Shaw flow-cells [69, 78, 79, 91, 92]. To test the capability of our setup for radial injections some slight modifications were made to the flow cell. The results were then compared to the results presented by Rocha et al. [79] in a similar setting but different fluid composition. Instead of a singe FEP layer, now three different sheets are pressed together between the sapphires as shown in **Figure 3.A.1**. Still each individual of the sheets has a thickness of 500 µm. The top most sheet contains the actual rectangular flow-cell geometry, similar to the setup described in **Figure 3.6 C**. The bottom sheet, on the other hand, hosts a channel of 2 mm width guiding one of the inlet holes in the sapphire to the middle of the chamber, where the fluid should enter. To keep the sheets with the chamber geometry and the channel separated, the third sheet lies in between the two an contains only a round orifice at the same positions the channel ends in the chamber middle to provide an entry point for the fluid. Additionally, the bottom and middle sheet have holes on the position of the holes in the sapphire, except for the inlet hole to the fluid channel there is not hole in the middle sheet. All other inlet holes are connected through the layers to the remaining inlet/outlet channels of the geometry in the top layer.

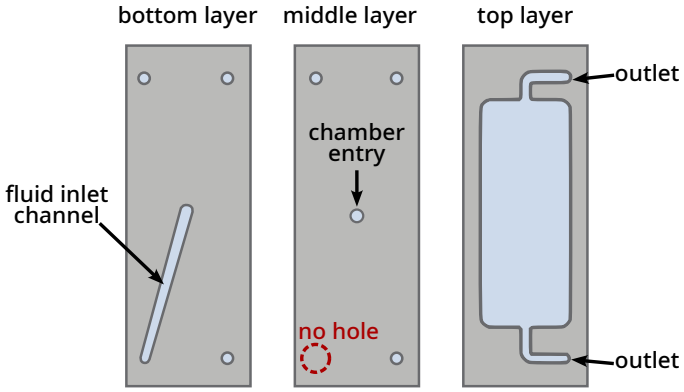

Figure 3.A.1: Chamber assembly for radial injection. Instead of just one, three layers of FEP-sheets are used to guide the alkaline fluid through an inlet channel to an orifice in the middle of the chamber. The top layers has again a rectangular geometry, whereas the bottom layer hosts a diagonal channel for the inflowing fluid. The middle layer separates top an bottom layers seals the chamber and the flow channel.

In order to investigate the morphology formation by radial injections similar fluid compositions as in the previous experiments are used: A solution of 1 M NaOH as alkaline fluid and 200 mM $Fe(II)Cl_2$ are both mixed with a fluorescent pH-dye in a ratio of 1:8. In this setting it turned out to be more difficult to bring the fluids together without bubbles of air remaining inside the chamber while at the same time avoiding premature precipitation within the

inlet channel, since no drainage channel could easily be guided close to the chamber entry. Therefore, before filling the chamber, alkaline fluid was carefully pumped into the inflow channel in the bottom layer while all the outlet channel were open until about 2 mm before the orifice. In a second step, the ocean solution was filled in the chamber via one of the remaining inlet/outlet channels while the second one remain open. After the prefilling procedure was complete, all outlet remain open and injection of the alkaline fluid was started at a flow-rate of 5 mL h^{-1}.

Figure 3.A.2: Radial injection of Alkaline Fluid in Acidic Ocean Solution. A sub-layer FEP-sheet guides the alkaline fluid to the round orifice or 2 mm diameter in roughly the middle of the chamber, where it comes in contact with the ocean solution. Precipitation starts around the orifice and creates irregular rings around the entry point in a spiral motion. After around 60 s the spiral motion recedes and form weak precipitates similar to flow fields until the chamber is filled. For better visualisation, both fluids are mixed with a universal pH dye.

In **Figure 3.A.2** the progression of the radial injected fluid is shown at three different time points. Right after starting the injection the alkaline fluid is pushed up into the chamber through the orifice and precipitation starts around the edge of the round inlet. However, since not a complete circle of precipitates is completed simultaneously, the fluid is further pushed in on the side of the inlet that is still open and progresses in a spiral motion around the orifice with precipitation continuing on the outer side of the spiral. This form irregular rings of different width around the entry point in a similar manner as observed in the layers/rings pattern (**Figure 3.2**) during injection from the side. Likewise, some kind of shortcut flow seems to form after several turns, so that further injected fluid bypasses the spiral. After that the fluid spreads in directed flows towards the outlets until the chamber is filled completely. This forms weak precipitates resembling the flow-field structures in the previous experiments.

Although the the radial injection also produced spiral precipitation in the beginning, the resulting structures do not match the observations shown in [79]. In contrast, the observed pattern here only formed irregular layers and did not continue to spread radially after the spiral motion. This might be due to several reasons, most of all the difference in chemical composition and chamber geometry as the chamber used here does not provide an ”infinite” area by being open on all sides and therefore restricts the geometry. Nevertheless, it could be shown that the setup is easily adaptable to more advanced ways of injection. Therefore, it would be an interesting alternative to commonly used flow-cells and could be tried with different chemical compositions.

3.B Influence of Gravity on Morphology

One key difference of the model setup used here to real-life alkaline vents is the the orientation of the injection vector. While the flow-cell in the experiments is horizontally placed, alkaline vent fluids are usually exhaled into the bulk ocean water against gravity. This is mainly based on the ion-composition of the alkaline fluid and also its higher temperature after reactions with the surrounding rocks, which both lead to a reduction in density compared to the ocean water. The orientation in the experiments is technically limited by the construction of the microscope, which only allow the visualisation at horizontal orientation of the flow-cell. The exhalation of the alkaline fluid is simulated by the applied pressure of the syringe pump. However, considering the densities of the fluids used in the experimental samples listed in **Table 3.B.1**, it appears that despite the different concentrations the difference in densities is only negligible.

Table 3.B.1: Calculated densities of alkaline fluid and ocean solution. For water a density of 997.13 g L^{-1} at 25 °C was assumed to calculate the densities of the fluids containing NaOH or Fe(II)Cl_2 as used in the experiments. Despite the different concentrations, the densities only vary marginally.

	Concentration (mol/l)	**Density (g/l)**
NaOH	1.000	1037.127
NaOH	0.800	1029.127
NaOH	0.200	1005.129
Fe(II)$Cl_2 \cdot 4\,H_2O$	0.200	1036.892
Fe(II)$Cl_2 \cdot 4\,H_2O$	0.075	1012.040

This could also be confirmed by an experimental test with a vertically orientated chamber and injection against gravity (**Figure 3.B.1**). An NaOH solution (1 M) is injected into an Fe(II)Cl_2 solution (75 mM) at 8 mL h^{-1}.

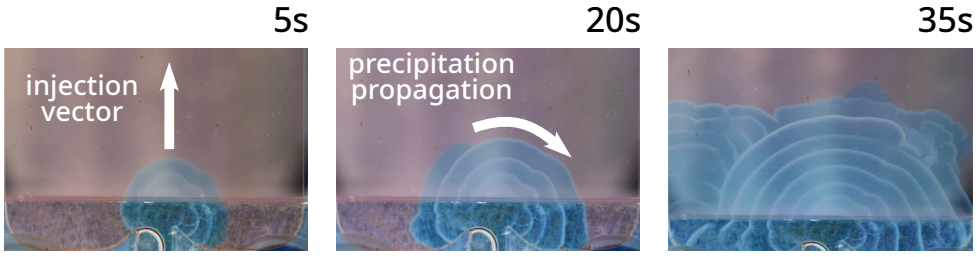

Figure 3.B.1: Injection of alkaline fluid against gravity. Upon entering the chamber the strong precipitates form that propagate in a ring-like motion around the injection point. Once the rings are as wide as to reach the sides of the chamber, the morphology transitions to thick precipitate layers. Overall the structure looks identical to the rings/layers obtained form injection from the side.

The morphology formation process is recorded using a photographic digital single lens reflex (DSLR) camera (EOS 90D, Canon, Japan) with a 65 mm magnification objective (65/2.8 MPE 419432, Canon, Japan). For better visualisation both fluids are mixed with a universal

pH dye in a ratio of 1:8. The result is shown in **Figure 3.B.1** for different times after start of the injection. In the beginning the precipitates start forming rings around the entry point of the chamber. Those then become more irregular and transition to layers of thick an stable precipitates filling up the whole chamber until all the remaining ocean fluid is depleted. The resulting structure looks identical to the layers/rings obtained form similar flow conditions at horizontal injection (**Figure 3.2**). Therefore, it can be assumed that the influence of gravity would only be marginally with the chemical composition of alkaline and ocean fluid in all experiments. Experimental conditions, shown to produce the two other dominant morphologies still need to be confirmed in anti-gravity injections.

3.C Alkaline Fluids at Higher Temperature

Modern alkaline vents, such as the Lost City alkaline hydrothermal vent field are consider "low-temperature" vents, although they vent fluids at a temperature between $40 - 90\,°C$ [30, 43]. Since all the experiments mentioned above have been carried out at room temperature, the question arises about the influence of higher temperature alkaline fluids on the morphology formation. In **Figure 3.C.1** shows a comparison of morphologies formed at different temperatures. For better contrast, the solutions have been mixed in a ration of 1:50 with the pH dependent fluorescent dye BCECF.

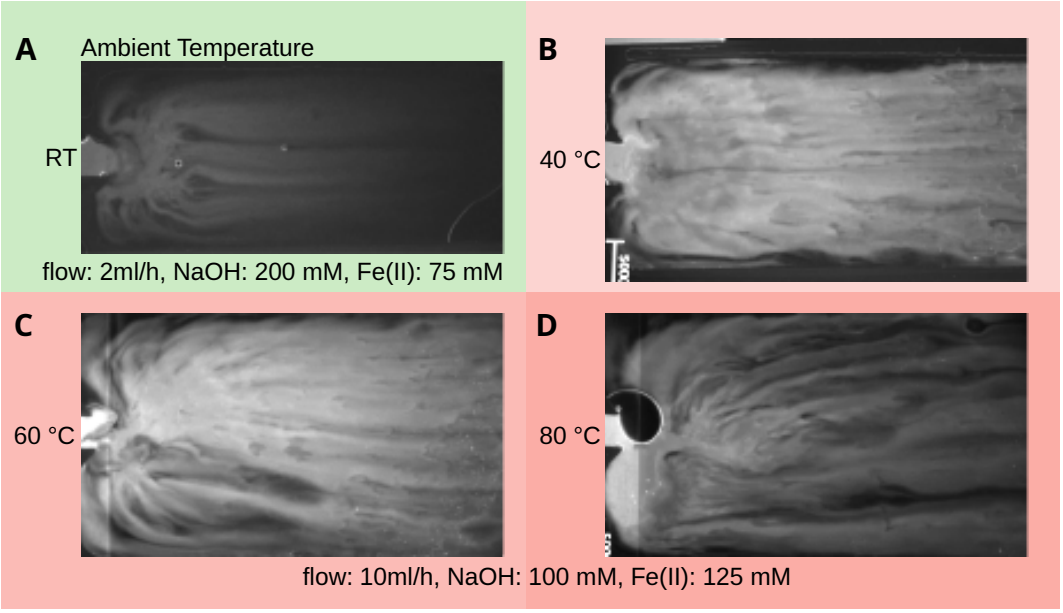

Figure 3.C.1: Morphology formation at higher temperatures. A morphology formed at ambient temperature (A) is compared to experiments conducted with alkaline fluid injected at 40 °C (B), 60 °C (C) and 80 °C (D). The resulting morphologies appear to be similar to the one at room temperature and show no significant alteration at higher temperature. Figure adapted form [60].

The comparison of the experiments at higher temperature (**Figure 3.C.1 B-D** with a morphology formed at ambient temperature (**Figure 3.C.1 A**) shows no significant alteration of the structures with increasing temperature. Therefore, it can be assumed that the precipita-

tion experiments at room temperature can be used to simulate the mineral forming processes happening in real-life alkaline vents.

It has to be noted, however, that the higher temperature experiments are not actually creating a temperature gradients between the two fluids due to the technical limitations of the setup. The sapphires used to seal the flow-cell have a high thermal conductivity and thus every temperature difference would be equilibrated quickly via those. Instead of maintaining a temperature gradient between the influx and the surrounding fluid, the warm alkaline injection rather heats up the whole chamber with the ocean fluid inside. Nevertheless, the whole precipitation process appears to be robust against temperature increase of the overall fluids. Apart form that, the comparison has been shown for experiments dominated by the flow-field morphology. A comprehensive screening to verify also the invariance under temperature increase of the other two morphologies would be needed to draw a general conclusion.

3.D Alternative Geo-chemical Composition (Carbonate)

For simplicity, in all experiments the most rudimentary geo-chemical composition was chosen to simulate alkaline vents, including an solution of $Fe(II)Cl_2$ as the ocean and sodium hydroxide as the alkaline fluid. Another interesting chemical ingredient in the context of alkaline vents, could be carbonate [93]. In the following experiments it was tried to simulate the same scenario, but with a solution of 100 mM K_2CO_3 (pH 11.5) as alkaline fluid and 200 mM $Fe(II)Cl_2$ with 100 mM K_2CO_3 + HCl (pH 5.76) to simulate an acidic ocean. Both solutions were mixed with a universal pH indicator for better visualisation of emerging gradients. **Figure 3.D.1** shows snapshots for the initial contact of the fluids (left) and after complete filling of the chamber (right).

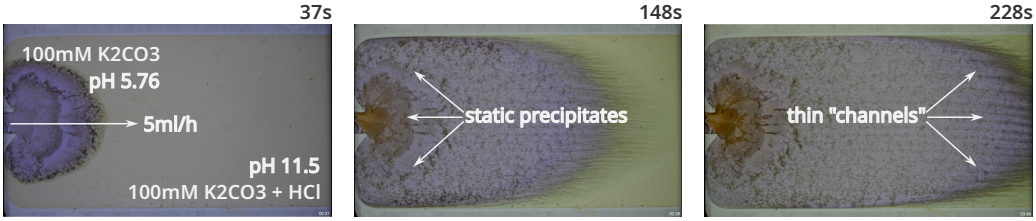

Figure 3.D.1: Alternative geo-chemical composition with carbonate. After injection of a K_2CO_3 solution into an ocean solution of $Fe(II)Cl_2$ with K_2CO_3 + HCl only weak and needle-like black precipitates form. The overall structure exhibits no stable precipitates, nor can the emergence of any gradients been observed.

Although precipitation can be observed upon contact of the carbonate-rich fluids, no solid structures as in the previous experiments were formed. As the alkaline fluid enters the chamber, a plume-like mixing of the fluids can be observed, that generates statically localised precipitates. The precipitates at the fluid front appear as black, needle-like chunks homogeneously distributed across the whole chamber and appearing like a multitude of narrow channels. However, all of the precipitates seem to be immersed in the mixed fluid and none of them forms a solid barrier between the two fluids. Because of that no gradients in pH seems to be present as the fluid seem to mix already completely during the injection process. Same is also indicated by the colours of the pH indicator. Although the concentrations

of the fluids have been chosen even lower compared to the previous experiments, the latter would still suggest the formation of flow fields with potential weak precipitates. However, no clear conclusion can be drawn on the influence of carbonate on the precipitate formation, further investigation and screening of parameters is needed.

Chapter

4

Nucleic Acid Accumulation on Alkaline Vent Chimneys

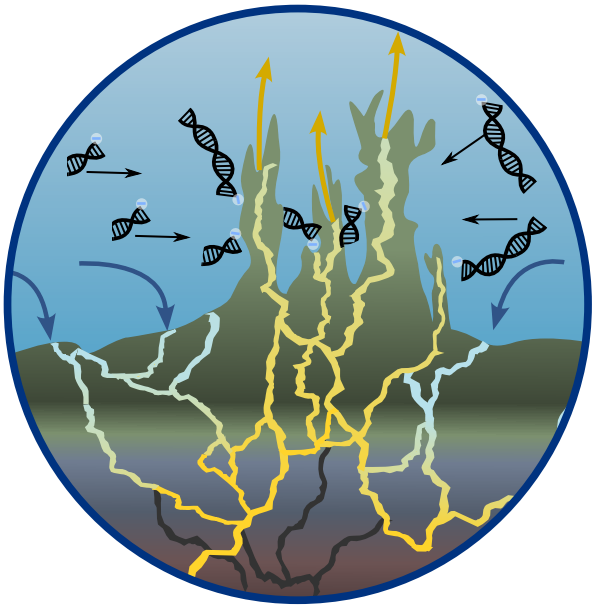

Summary: The prebiotic Earth was dominated by extensive oceans allowing only for high dilutions of dissolved molecules, representing the so called 'concentration problem'. The chimney-like structure of alkaline vent precipitates could provide a promising location for accumulating long nucleic acid strands from surrounding ocean water. Emerging oxyhydroxide minerals can act as a semipermeable membrane allowing the formation of strong ionic gradients between the alkaline interior and the acidic ocean. As a result, diffusiophoresis would drive dissolved nucleic acids towards the chimneys, where it adsorbs to the mineral surface yielding locally enhanced concentrations and prevention renewed dilution.

This chapter at first describes the optimisation of experimental setting that allows low-volume DNA experiments on de-novo formed mineral chimneys. Further, the challenge of extracting, desalting and analysing DNA from mineral and ocean samples is investigated and at last the qualitative results of accumulation are presented.

To simulate the chimney formation in the lab, we used and alkaline fluid (pH 13) injected bottom-up into a closed flask containing an Fe(II)-rich ocean simulant (pH 5.5) with dissolved DNA ladders. Follow-up experiments incorporated yeast-derived RNA and showed depletion of RNA form the ocean solution, suggesting its binding to dissolved iron and incorporation into the mineral structure during precipitation. [1]

[1]The results of the RNA experiments are published by Helmbrecht et al. in *Geobiology* [45].
Authors: Vanessa Helmbrecht, Maximilian Weingart, Frieder Klein, Dieter Braun and William D. Orsi.
(Chapter title figure and its variations throughout the thesis adapted from this publication.)

4.1 Introduction

Besides all the different theories for the origin of life, the availability of water is thought to one key requirement for Earths habitability [6]. After the moon forming impact around 4.5Ga ago, Earth needed to cool down to a temperature that allowed the aggregation of water and was compatible with prebiotic chemistry [6, 94, 95]. Even though Earth started to have liquid water already around 4.4Ga years ago [7], it is assumed that there have been several more "sterilising" collisions, so that temperatures allowing life and a stable hydrosphere could only be established$\sim$4.2Ga ago [6, 9]. Considering this lower limit as the earliest possible time for the emergence of life to start [6], it requires to think about plausible locations that supports prebiotic chemistry and is at the same time compatible with early Earths geological settings [8]. Alkaline hydrothermal vent environments, often proposed as one of life's potential starting sites [24, 56], could have likely been present on an early Eath $\sim$4Ga ago [21]. This would provide the two main requirements for hydrothermal vents to form: a heat source and liquid (water) phase [33].

In general, hydrothermal vents form by ocean water percolating in cracks and pores on the seafloor, where it get enriched in ions, warm and strongly alkaline by reacting with the surrounding ultramafic rock [24]. Buoyancy differences then leads to the exhalation of the alkaline fluid into the ocean, forming the characteristic chimney-like precipitates, upon contact with the ocean water [24, 26, 30]. Compared to the typical black smokers that feature temperatures up to 400 °C [41], the exhaled fluid in alkaline hydrothermal vents usually only reached temperatures up to 90 °C [30], providing compatible conditions for early life [24]. While modern alkaline vents precipitate mostly carbonate and brucite minerals [30], potential vents in the Hadean and Archean have likely been different in terms of their geo-chemical composition [56]. As the early Earth had a CO_2-rich atmosphere, the oceans were likely saturated in CO_2 and thus slightly acidic [25, 53, 54]. Additionally, the water was likely anoxic and high in dissolved iron [52]. Even though, at this stage the emergence of modern vent minerals is unlikely, the conditions would promote the formation of fougerite, also called "green rust" [56, 57]. This ferrous-ferric oxyhydroxide mineral has the capability of acting as a mineral membrane, giving it the potential to perpetuate the strong-non-equilibrium conditions between the alkaline interior of the chimney-tubes and the acidic surrounding ocean water [26, 54, 56, 59, 68].

The establishment of Earths hydrosphere, however, brings along also one of the biggest consequences for prebiotic chemistry: Any molecules present on the early Earth was only available in highly diluted form within an extensive ocean [10]. This circumstance poses one of the major challenges in origins of life research and commonly referred to as the "concentration problem" [10]. In order for chemical evolution to start, it requires the necessary feedstock molecules to be present in sufficient quantity [8, 96]. Alkaline hydrothermal vents have been proposed to be able to concentrate nucleic acids from diluted ocean water [97]. So far, however, the hypothesis had never been tested.

In this scenario, alkaline vents provide an environment that hosts strong gradients in temperature, pH, redox-potential and ionic compositions, separated by a semipermeable barrier of redox-reactive minerals [26]. It has already been demonstrated in the past, that physical non-equilibrium conditions have the potential to accumulate dissolved molecules and enhance their concentration multi fold [11–14, 72]. In the case of alkaline vents, a steep ionic gradient is established across the mineral precipitate forming between the alkaline interior and the acidic ocean [26, 31]. Dissolved nucleic acids in the vicinity of the growing chimney

could therefore be moved towards the precipitate by a process called diffusiophoresis [31]. Additionally, RNA or DNA molecules could further be localised by adsorption to the mineral surfaces [59, 71, 98, 99].

Although the recreation of alkaline vent structures in the lab has been attempted before [23, 34, 68], they have not yet been tested for their potential to accumulate dissolved nucleic acids. Most of the laboratory setups, applied large volumes to recreate the venting of alkaline fluid into a bulk ocean [68], a setting that is unfortunately not practically for low volume experiments that incorporate potential organic molecules or study chemical reactions. Although similar structures have been grown in low volume as so called "chemical gardens" in the field of chemobrionics [58, 75], the structure generating mechanism and chemical composition was mostly different and not targeted to study origin of life scenarios at all.

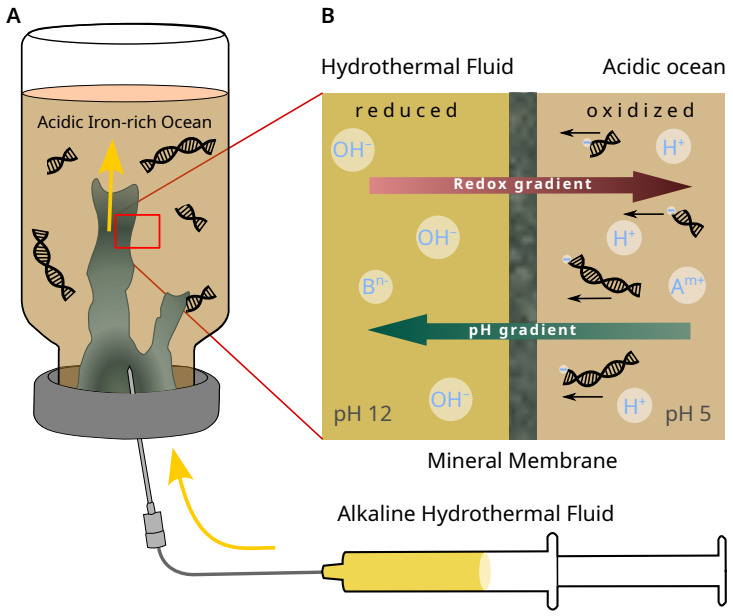

Figure 4.1: Laboratory recreation of hydrothermal chimneys to test accumulation of dissolved DNA. **A**) To mimic the precipitation process of the tubular precipitates in AHVs, a 5 ml crimp flask is prefilled with a ferric-ferrous solution to simulate a potential acidic Hadean ocean with ∼pH5. Injection of NaOH + Na_2S at pH12 as hydrothermal fluid is injected from the bottom and shows green-blackish precipitates upon contact with the ocean simulate. **B**) The precipitates act as a semi-permeable mineral barrier, maintaining steep gradients in pH between the in flowing fluid and the ocean solution. Dissolved DNA in the latter can therefore be dragged towards the chimney walls by diffusiophoresis and adsorb to the mineral surfaces, resulting in localisation and accumulation.

In the following experiments, aim to explore the capabilities three dimensional recreations of hydrothermal vent chimneys in the laboratory. Since the study any potential chemical reaction system in a hydrothermal environment requires the incorporation of feedstock molecules or organic precursors, the need for low volume experiments with recoverable samples is apparent. Experiments will therefore show the scalability of simple setups using sealed flasks prefilled with ocean simulant. Injection of hydrothermal fluid is provided by a syringe pump, connected to the ocean solution containing flask via a syringe needle

pinched through a septum. Alkaline fluid inflow into the upside-down flask then manages to produce chimney-like structures growing through precipitation in the middle of the flask. A setup using a 5ml crimp-seal flask and will then be applied to study the incorporation of long DNA strands (100–10,000bp) into the ocean. Analysis of ocean water and extracted mineral chimney test the capabilities of DNA accumulation and concentration. Along this way, also the steps necessary for recovery and extraction of dissolved and adsorbed DNA are examined together with potential ways to quantify retrieved amounts. Follow up experiments then test the sequestering of dissolved RNA from a bulk ocean solution. The results of the followup experiments including RNA are published in [45].

4.2 Results

The experimental setup and the chemical composition used in the following experiments for the growth of alkaline vent like chimney precipitates was inspired by the Barge and coworkers [23, 68]. The laboratory mimic of the hydrothermal environment applies a crimp-seal glass flask with pinchable septum to host an iron rich solution to simulate a Hadean/Archean ocean. Venting of hydrothermal fluid is then simulated by insertion of a needle through the septum into the upside-down vessel and injection of a sodium hydroxide solution by a syringe pump. Upon contact of the two fluids, mineral precipitation sets in and starts growing one or more chimney-like tubes around the fluid stream in the middle of the flask. The following sections describe the experiments exploring the scalability of the setup of for low-volume experiments, potential methods for the extraction and analysis of incorporated DNA samples. These experiments served as a base for DNA alkaline vent investigation and are therefore only presented as a qualitative description of the different key aspects to keep in mind. The follow up experiments incorporating and accumulating RNA have been published by Helmbrecht et al. [45] and will be presented at the end of the section.

4.2.1 Scaling Capabilities of the Experimental Setup

For the incorporation of organic material such as nucleic acids, usually not readily available for laboratory purposes, it is vital that experiments can be carried out in low volume. The setup therefore needs to enable the cost efficient integration of the material while at the same time keeping up the vent's unique features, such as the tubular structure and the emerging (geo)-physical gradients. Any boundary effects on chimney growth imposed by the vessel itself, should be avoided. Previous publications [23, 68] achieved recreations of the natural hydrothermal systems as chemical gardens in crimp-seal flasks of 120 mL volume. Since the eventual goal of the following experiments was to investigate DNA accumulation and potential length selection, comparable volumes were not feasible as DNA samples of known size distribution are usually only available small quantities of a few micro-grams. To test the the limits of scalability in different vessels that are still capable to represent the characteristic structure of the growing minerals, a range of standard laboratory containers has been put to the test.

For the recreation of the hydrothermal environment, the process of alkaline fluid venting in the bulk ocean water is simulated by injection of a mixture of H and Na_2S into an ferrous-ferric ocean simulant. Therefore the ocean solution is prefilled into a vessel or flask and alkaline fluid is injected by a syringe pump through a canula pinched through either a

septum or the plastic bottom/lid of the container. In the latter cases, the needled had to be tightened with epoxy around the puncture. The flask is then held in place by a laboratory stand in a way that the injection provides a fluid flow emerging from the centre of its bottom part (see **Figure 4.1**, yellow arrows indicate the injection vector). Upon contact of the fluids, mineral precipitates of greenish-black colour start to from. **Figure 4.1** shows the resulting chimney structures in different flask sizes.

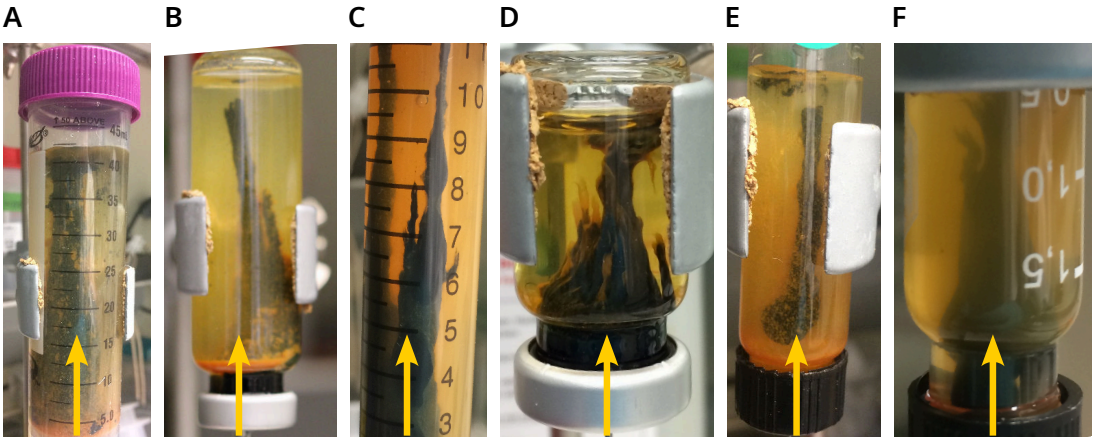

Figure 4.1: Chimney precipitation in flasks of different size. An alkaline solution containing NaOH and Na_2S was injected into flasks prefilled to about 2/3 of their volume with ferrous-ferric ocean simulant. The characteristic chimney structure could be obtained in **A**) 50 mL falcon tube at 23 mL h^{-1}, **B**) 20 mL crimp flask at 20 mL h^{-1}, **C**) 15 mL falcon tube at 15 mL h^{-1}, **D**) 5 mL crimp flask at 5 mL h^{-1}, **E**) 4 mL screw cap vial at 4 mL h^{-1} and on the lowest end **F**) 1.5 mL HPLC vial at 2 mL h^{-1} inflow rate.

The experiments show that chimney-like tubular mineral structures can form around the fluid stream in the all of the tested flask sizes under appropriate choice of inflow-rate and needle diameter. Regarding the pumping, the structures could form at set flow-rate between 2 mL h^{-1} and 23 mL h^{-1}. Readjusting the flow-rate with the flask size appears as a logical choice and resulted in the most stable structures in the respective flask. Another crucial impact, however, was given by the diameter of the needle used to inject the alkaline fluid. While needle diameters 0.4 mm, 0.8 mm, 1.1 mm have been tested, 0.8 mm inner diameter turned out to be the most versatile choice, that supports all flask sizes and flow rates. Larger diameters failed to produce chimney structures, as precipitation just filled up the flask from the bottom and did not grow in to tubular structures. Smaller diameters worked for small volumes and flow-rates, however, not for all flasks larger than 1.5 mL. Considering the resulting chimneys in the different flasks, the ones with 1.5, 4 and 15 mL were rather narrow compared to their diameter, which lead to the growing tube likely leaning to the side and getting attached to he walls of the vessel. This makes it more difficult to generate reliable stable structures. On the other end, 20 and 50 mL flasks offer a good environment for recreating the typical chimney structure, however, still host too much volume to integrate small amounts of nucleic acids. Therefore, in the following experiments, 5 mL crimp flasks are chosen, as they offer a reasonable volume and still provide enough radial space for the the tubular mineral precipitates to grow.

4.2.2 DNA Extraction form Alkaline Vent Environments

Apart form the creation of a reliable setup that offers enough control to create stable and reproducible chimney structures, the major challenge in this project was the the extraction of DNA form the alkaline vent model after the experiment. On the one hand, if nucleic acids are adsorbed to the mineral surfaces as expected, it is required to liberate the bound strands form the minerals prior to analysis. On the other hand, the solutions used in the experiments contain high amounts of iron and other salts to simulate a prebiotic ocean (see **Table 4.1**) that potentially cause issue with common analysis methods.

The principle of extracting adsorbed nucleic acids is based on the assumption, that mainly the phosphate groups of the nucleic acid's negatively charged backbone interact with the charged mineral surfaces. A first step in the extraction of the DNA sample is therefore the destruction and redissolution of the generated chimney samples by homogenisation of the sample in a BeadBeater together with silica beds. Apart form the mechanical destruction it can also help to add HCl to the sample tube, as the minerals only precipitate at alkaline pH. To remove potentially bound DNA form the iron complexes in solution, the protocols for the extraction then apply phosphate buffer to exchange the bound phosphate groups on the dissolved or precipitated iron complexes.

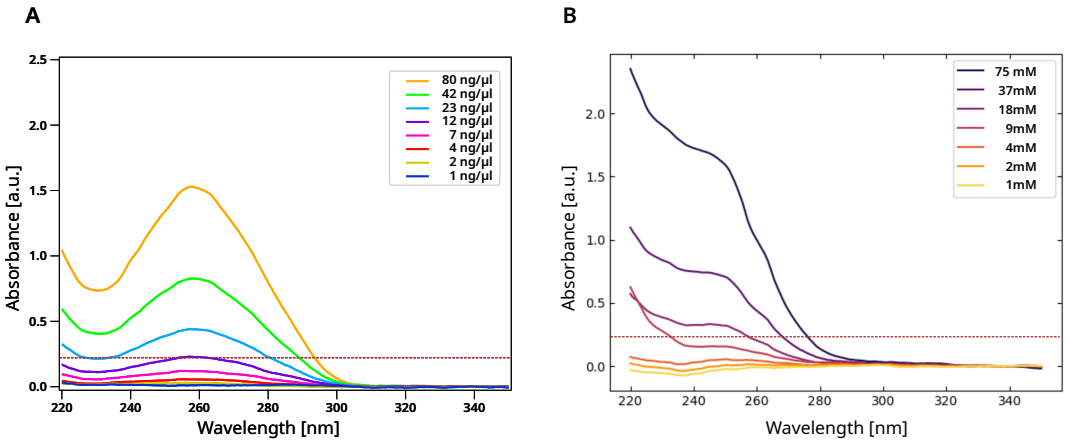

Figure 4.2: Absorbance of DNA compared to the Fe(II)Cl_2 solution.

However, for analysis the detachment form the binding metals or minerals is not yet sufficient for analysis, as the iron and salt in the sample solution might also interfere with most spectroscopic analysis methods. **Figure 4.2** shows a comparison of the the absorbance spectra of a dilution series of of the DNA ladder (100-10,000bp) and solution Fe(II)Cl_2 at different concentrations. Spectroscopic nucleic acid quantification methods (e.g. NanoDrop) use the characteristic absorption maximum of DNA at 260 nm, which can be seen for different concentrations in **Figure 4.2 A**. This value can usually be used to deduce nucleotide concentration and therefore the amount of DNA in the sample. Considering **Figure 4.2 B**, it can clearly be seen, that the absorbance of iron complexes in Fe(II)Cl_2 solutions exceeds the one of DNA concentrations (10 µg µL^{-1}) at a concentration around 9 mM, a fraction of what is used in the experiment. In **Figure 4.A.1** influence of iron on the extraction/analysis of DNA on a Bioanalyzer is shown. Despite equal DNA concentration in the samples, extraction form the ferric ocean solution showed significantly lower peaks compared to water and artificial sea-water.

In order to desalt and concentrate the DNA samples, primarily centrifugal filters are applied that retain the nucleic acids while flushing through most of the liquid including the dissolved ions and leaving a concentrated low volume containing the DNA. Higher amounts of DNA can be reached by repeating the step after adding again sample volume to the concentrate in the filter. Desalting on the other hand can be achieved by repeated centrifuging after after adding water to the concentrate. Further and more effective reduction in salt concentration is achieved by dialysis in SnakeSkin membranes, that let ions in the sample diffuse out into a larger water reservoir (for details see section 4.3). The efficiency of both methods on samples of ferric ocean solution is shown in **Figure 4.A.2 A**. SnakeSkin thereby turned out to be even more efficient in desalting than several dilution-filtration steps in centrifugal filter tubes. The effect of the desalting procedure with SnakeSkin on experimental samples is shown in **Figure 4.3**.

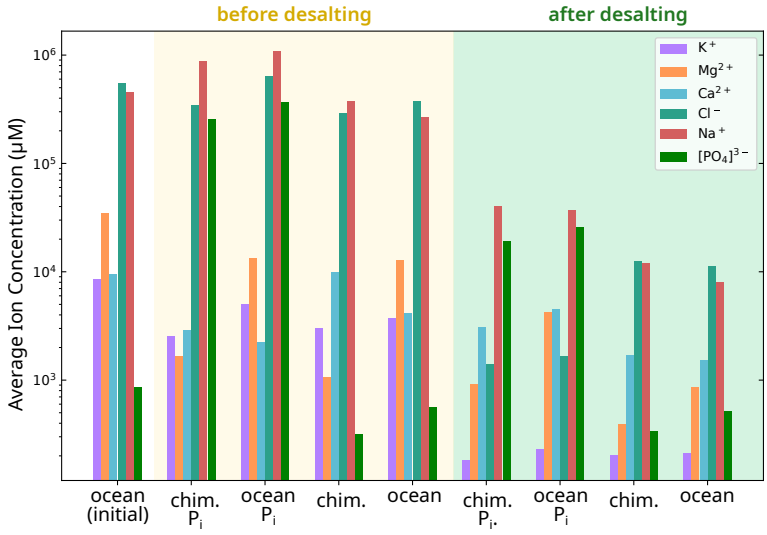

Figure 4.3: Desalting protocol applied to experimental sample. Assessment of ion concentrations using ion chromatography shows a significant reduction after the application of SnakeSkin for desalting for 30 min. The concentration of iron could not be measured, due to technical limitations of the instrument.

Due to the advantages of both methods (concentration and desalting, respectively) a combination of them was applied to the experimental samples.

4.2.3 Accumulation of Long DNA Strands on Hydrothermal Chimneys

The following section studies the incorporation of dissolved dsDNA strands into the hydrothermal system recreated in a low volume model using a 5 mL crimp-seal flask. The scope of the experiment is to study the up concentration and localisation of DNA integrated in the ocean solution during growth of the chimney precipitates by accumulation and adsorption in the vicinity of the mineral surfaces. For the DNA samples 50 µg of a dsDNA ladder were added to the ocean solution prior to the injection of the alkaline fluid resulting in a concentration of 10 ng μL^{-1} or an overall nucleotide concentration of about 33 µM. The ladder contains strands within the range of 100–10,000bp and thus offers a wide range of different

lengths, while at the same time the theoretical size distribution of the incorporated strands is known a priori.

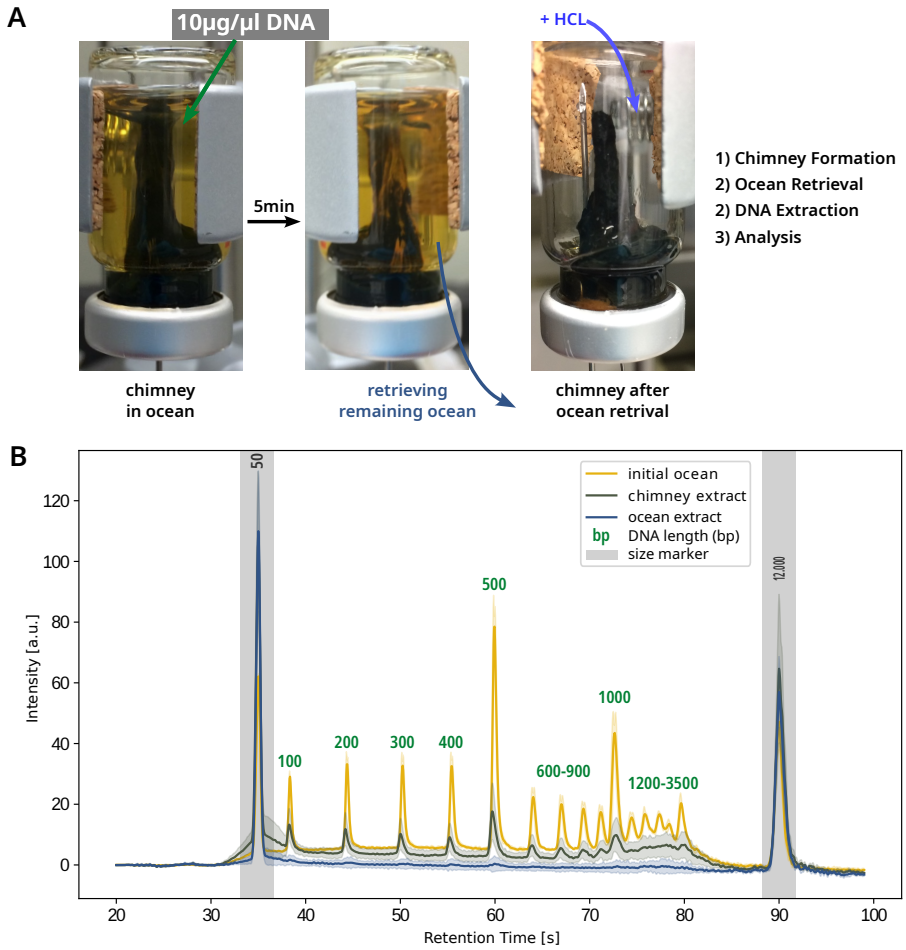

Figure 4.4: Average of extracted chimney and ocean samples form ferric ocean with sample desalting. **A**) Injection of NaOH + Na_2S into a ferrous ocean of 70 mM Fe(II))Cl_2 with 10 ng µL^{-1} dissolved DNA ladder (100-10,000bp). After retrieval of the remaining ocean solution, the chimney minerals were redissolved by addition of HCl. **B**) Bioanalyzer measurement of multiple samples showed similar chromatograms. Averaged traces show higher amounts of extracted DNA in the chimney than in the ocean samples throughout.

Experiments applying desalting of samples with SnakeSkin as well as the addition of HCl to the chimney sample to dissolve the structure were carried out in a ferric ocean solution containing 70 mM Fe(II)Cl_2. After the chimney precipitate is formed upon injection of the alkaline fluid, the sample flask is left at rest for approximately 5 min to provide time for potential transport processes to take effect. During this time, it can be seen that the mineral structures undergo slight colour changes at the outer parts of the tubular structures as seen in **Figure 4.4 A**. To separate ocean from chimney sample, the remaining ocean solution in the flask is retained manually by piercing a syringe with needle through the septum, and adding a single canula for pressure balance. The remaining chimney mineral in the flask is then redissolved by addition of HCl followed by the extraction protocol for both ocean and

chimney samples. The effect of desalting and mineral dissolving by lowering the pH showed to have a positive effect on the reliability of extraction or analysis, as all of the multiplexed experiments showed similar chromatograms, indicating clear peaks in the chimney samples and almost no peak in the retrieved ocean. **Figure 4.4 B** shows the averaged chromatograms from multiple samples under identical conditions. The shaded areas around the slopes indicate standard deviations across the multiple samples. While fewer fluctuation can be seen for initial ocean solutions, the chimney extracts show larger deviations across multiple samples. However, the overall trend in comparison with the ocean extract could be observed in all samples.

Consideration of **Figure 4.4 B** show a trend for all samples of clearly visible peaks in the chimney and depleted ocean. All individual runs (6 repetitions for chimney and ocean, 4 samples for the initial ocean solution) give comparable peaks for chimney and ocean sample and have been averaged in the plot. The traces show almost no peaks for the extracted ocean solution after the experiment, however, indicate clear peaks for several strand lengths in the extracted ocean sample. While the peaks are well visible for the shorter strands up to 1000bp, only very noisy signals are given for the long strands between 1200–10,000bp, which might also be explained by the lower resolution of the instrument for larger DNA molecules. Comparison to the initial strand length distribution of the extracted ocean prior to the injection of alkaline fluid, it is clearly visible that the signal is exceeding the post experimental ones multi-fold. This suggests primarily an inefficient extraction of the DNA form the mineral sample or potentially even hydrolysis of due to the much higher pH in the vicinity of the alkaline fluid stream within the flask.

4.2.4 Follow up Experiments with RNA

The followup experiments incorporate RNA instead of DNA. Their results are published by Helmbrecht et al. in *Geobiology* [45]. In order to achieve sufficient nucleic acid concentrations in the ocean simulant, yeast derived RNA is used, that is readily available as commercial stock. Apart from the usage of RNA, also the overall setup is slightly different form the previous experiments. To keep the geo-chemical composition as simple as possible, the ocean solution is solely simulated with dissolved $Fe(II)Cl_2$ under anoxic conditions. Hydrothermal injections are still provided by a sodium hydroxide solution, however, at a matching concentration of 200 mM to the iron-chloride and an inflow rate fo 3.7 mL h^{-1}. Anoxic conditions are provided by an oxygen level of less than 100ppm in a glovebox, to examine emerging minerals under prebiotically assumed conditions. To account for a large enough ocean reservoir, the experiments were conducted in 100 mL crimp seal flask. However, a more accurate scenario was simulated by cutting off the bottom of the glass vessel, so that the injection of the fluid only had to work against atmospheric pressure and no pressure built up in the vessel during the course of the experiment. To compensate for the large volume, higher amounts of RNA were used, readily available as yeast (*Saccharomyces cerevisiae*) derived RNA (Sigma-Aldrich, USA). Extraction of RNA used a different approach with combination of trizol and phosphate buffer with subsequent RNA precipitaion and subsequent fluorometric analysis (QBit 3, Invitrogen, Thermo Fisher Scientific, USA). Initial probing of the ocean solution after integration of RNA showed concentrations of (3.96 ± 0.54) ng μL^{-1}.

Figure 4.5 B shows the depletion of RNA from the ocean solution during growth of a chimney precipitate by injection of an alkaline fluid. It can be seen that the depletion rate of RNA corresponds to the growth rate of the chimney structure. Control experiments attempting

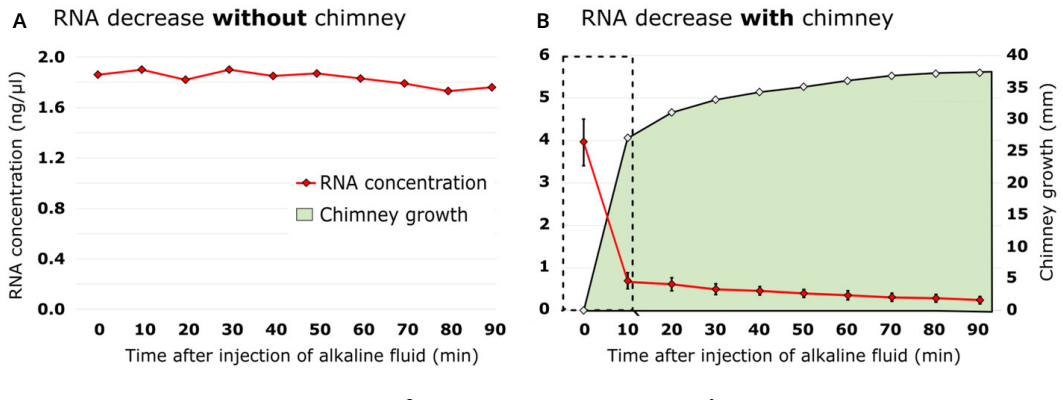

Figure 4.5: RNA depletion form ocean solution over time. **A**) RNA amount in a ferruginous ocean solution stays at a consistent level over time if no precipitates are forming. **B**) RNA is depleted from the ocean solution with increasing height of the forming chimney precipitate. Figure reprinted in parts with permission from [45].

extraction from the ferruginous ocean without phosphate buffer showed that no RNA could be extracted without phosphate, indicating that the RNA molecules are already bound to iron complexes in solution. This in turn leads to the conclusion, that RNA is sequestered into the mineral structure form the ocean solution during precipitation.

4.3 Materials and Methods

The experimentation is based on the three-dimensional recreation alkaline vent precipitates by injection of alkaline fluid into a iron-containing ocean solution. The geochemical composition of the samples has been chosen so that it could resemble a plausible prebioitic scenario on an Hadean or Archean Earth.

4.3.1 Sample Preparation

Both solutions for ocean and hydrothermal fluid were prepared freshly for each of the experimental runs. For the ferrous-ferric ocean solution one equivalent of iron(II)chloride tetrahydrate [$Fe(II)Cl_2 \cdot 4\,H_2O$] (Sigma-Aldrich, USA) and two equivalents of iron(III)chloride hexahydrate [$Fe(III)Cl_3 \cdot 6\,H_2O$] (Sigma-Aldrich, USA) were dissolved in artificial sea-water (**Table 4.1**) in a ratio of 1:2 to obtain concentrations of 70 mM and 35 mM, respectively. In experiments using a ferrouginous ocean solution, only $Fe(II)Cl_2 \cdot 4\,H_2O$ was dissolved in artificial sea-water at a concentration of 70 mM or 105 mM. In order to keep the oxidation of iron(II)chloride at a minimum, it was stored under inter gas (Argon) and all flasks and vessels were flushed with argon before usage. However, complete oxygen free conditions could not be guaranteed during the experiment. For the alkaline hydrothermal fluid solid flakes of sodium sulphate [$Na_2S \cdot xH_2O$] (Carl Roth, Germany) were dissolved at a concentration of $3\,g\,L^{-1}$ ($\sim$38.44 mM) in a volumetric standard solution (1 M) of Sodium hydroxide [NaOH] (Carl Roth, Germany). To incorporate DNA into the ocean, one packaging unit of GeneRuler DNA Ladder Mix (20µl) (SM0331/SM1551, Thermo Fisher Scientific, USA) was added into the crimp-sealed flask containing the ocean solution by injection through the septum with a syringe giving a concentration of $10\,ng\,\mu L^{-1}$.

Table 4.1: Artificial sea water recipe used as base for the iron-containing ocean solution. The composition was provided by the laboratory of Prof. William Orsi and based on the protocols described by [100] with slight modification.

Salt	Concentration [mM]	Concentration [g/l]
NaCl	422.09	24.67
KCl	8.94	0.67
$CaCl_2$	15.02	1.67
$MgCl_2$	77.02	7.33
$NaHCO_3$	21.82	1.83

The sodium phosphate buffer was prepared as a 1 M stock by first dissolving 25.67 g disodium hyrogen phosphate $Na_2HPO_4 \cdot 2\,H_2O$ (Carl Roth, Germany) and 16.49 g sodium dihydrogen phosphate$NaH_2PO_4 \cdot 2\,H_2O$ (Carl Roth, Geramany) in 250 mL nucleoase-free water (Ambion, Invitrogen, Thermo Fisher Scientific, USA). To prepare 10 mL extraction buffer, 8.35 mL of the phosphate buffer is mixed with 1.65 mL non denatured ethanol ($\geq$99.8%, Carl Roth, Germany). Ethylenediaminetetraacetic acid (EDTA) is added for extraction from a commercial 0.5 M standard solution (Ambion, Invitrogen, Thermo Fisher Scientific, USA) and diluted in nuclease-free water so that the concentration is about equal to the iron concentration in the extracted ocean liquid.

4.3.2 Setup

The experimental setup is based on the approach reported by Barge and coworkers [23, 68], but adapted to lower volume in order to integrate DNA. Therefore an iron containing ocean solution is filled into a 5 mL headspace flask that had been preflushed with argon gas to limit oxidation of the Fe(II). After filling of the flask with approximately 4.5 mL it sealed with crimp-top. The DNA ladder mix (100 µL is integrated into the ocean by injection with a syringe through the septum. This leaves approximately 5 mm space to the bottom of the flask, when turned upside down. The flask is fixed in a standard laboratory stand with the septum facing downwards. The alkaline fluid (either NaOH or NaOH + Na_2S) is taken up by a50 mL single-use syringe equipped with a canula of 1.1 mm inner diameter (ID). The syringe is mounted into a programmable syringe pump (AL-1000, World Precision Instruments, USA) and the canula connected to a teflon tubing (1.00 mm inner diameter). The other end of the tubing is connected to a canula of 0.8 mm inner diameter via standard low-pressure fittings/adaptors and tubing/needle are prefilled with solution form the syringe, until the liquid is around 20 mm before the tip of the canula, so that precipitation (fluid contact) only sets in when the pump is started. The canula is then pierced through the septum into the flask, so that approximately 5 mm of the needle stick out on the inside. Starting of the pump injects the alkaline fluid into the ocean solution and starts the mineral precipitation process.

4.3.3 DNA Extraction

In order to extract DNA form the hydrothermal vent model, the mineral chimney and remaining ocean need to be separated after the experiment after the injection process is completed. This is accomplished by retrieving the the ocean fluid around the chimney precipitate with a 5 mL syringe equipped with a long 0.8 mm ID needle. The canula is carefully inserted on

into the flasks at the outer edge of the septum, so that the tip is positioned in the ocean fluid around the chimney without touching or damaging the precipitate. For pressure balance another blank needle is inserted with the tip at the highest point of the flask. After complete separation of chimney and ocean, the chimney is shaken to destroy the mineral structure and 900 µL of both samples are pipetted in test tubes for treatment with either of the following protocols in order to extract the attached/dissolved DNA.

Minerals samples were destructed by shaking a lysis tube with sample and 100 µm silica beads in a Mini BeadBeater-1 (Biospec, USA). For desalting and concentration of the extracted DNA SnakeSkin desalting tubes with 3.5kDa molecular cutoff (Thermo Fisher Scientific, USA) and centrifugal filter tubes with 4kDa molecular cutoff (Amicon, Merck, USA) were used.

Phosphate-Extraction Protocol

This protocol has been adapted from an protocol intended for DNA extraction from solids and soils that has been provided by the lab of Prof. William Orsi [2] and is based the protocol described in [100, 101]. Steps 4 to 7 are mainly required for the breaking of cellular compartments during the extraction of DNA from biotic material. Their impact in the extraction form nucleic acids is therefore probably limited and an be left out.

1. Heating of extraction buffer ($NaPO_4$ + EtOH) to 60 °C until the $NaPO_4$ crystals dissolve
2. Addition of 350 µL HCl to 350 µL chimney sample to dissolve precipitated minerals
   → Addition of the equivalent amount of water to the ocean sample to compensate the dilution
3. 440 mg of silica beads (100 µm) in 2 mL lysis-tube
   Addition of 750 µL of sample + 500 µL of extraction buffer
4. Homogenising in BeadBeater for 40 s
5. Heating at 99 °C for 2 min
6. Freezing at −80 °C, thawing
   Repetition (two freeze/thaw cycles)
7. Heating at 99 °C for 2 min
8. Homogenising in BeadBeater for 40 s
9. Centrifuging at 4700 RPM for 10 min
10. Pipetting of 900 µL of the supernatant into SnakeSkin
    Leaving in 500 mL MilliQ H_{20} for 40–50 min
11. Pipetting of (500 µL sample into Amicon filter, centrifuging at 14000 × g for 15 min
    Repetition (400 µL supernatant)
12. Discarding of flow-through, addition of 420 µL nuclease-free water

[2] Prof. Dr. William Orsi, Department für Geo- und Umweltwissenschaften Paläontologie & Geobiologie, Ludwig-Maximilians Universität München

13. Centrifuging at 14000 × g for 30 min
    → Results in 48 µL of concentrate

14. Placing the filter inset upside down in clean tube, centrifuging at 1000 × g for 2 min

4.3.4 DNA Analysis

Several methods have been applied to selectively analyse the amount of DNA stands of different length in the samples after extraction as described above. Bioanalyzer (2100, Agilent, USA) analysis was carried out to analyse the strand length distribution of DNA in the samples. In order to resolve the wide range of different lengths the instrument was equipped with the Agilent DNA 12000 Kit for analysis of dsDNA strands up up to 12,000bp and operated as specified by the manufacturer. Spectroscopic analysis of the samples was done by absorbance measurements of micro-litre droplets on a Nanodrop spectrometer (NanoDrop One^c, Thermo Fisher Scientific, USA).

4.4 Discussion

The study of recreations of the characteristic topology and structure of mineral precipitates in alkaline hydrothermal vents started form the approached published by Barge at all [23,68]. The attempts to scale the laboratory model systems showed that tubular chimney structures can precipitate upon injection of alkaline fluid into a ferric-ferrous ocean solution in a wide range of common laboratory vessels starting from 50 mL and reaching down to even 1.5 mL. One key aspect, however, is the consideration of potential boundaries that smaller flasks add to the system and how they potentially influence characteristic features. Especially for high and narrow containers, the emerging chimney structures were likely to collapse, fall to the side or attach to the wall of the flask during growth. This is not only reducing the available mineral surface area for potential adsorption of studied molecules, but shifts the ratio of chimney volume (mineral plus enclosed fluid stream) and bulk ocean water. Characteristically, the chimney is surrounded by an extensive ocean, acting as a huge reservoir of ions. Limited ocean water left around the chimney could therefore reduce the non-equilibrium settings across the mineral membrane diminish emerging gradients.

The technical possibility for low volume experiments is crucial to study chemical reactions or the integration of bio-chemical material into the hydrothermal vent system in a cost efficient way. Especially for the study of length or sequence dependent DNA experiments, the material is usually expensive and and only available in low concentration and quantities. As the original idea of the project was to analyse the length dependent DNA accumulation inf hydrothermal vents, DNA ladder mixes turned out to be the best starting material. To reach sufficient concentration in the final ocean mixture while still providing key features of the chimney structures, 5 mL headspace bottles with crimp seal were used in the experiments.

One key challenge of the experimental system is the extraction and analysis of the integrated molecules and materials of interest. While it was possible to separate the ocean solution and the precipitated chimney structure quite efficiently by retrieval of liquid around the solid mineral, both samples contained high concentration of ions and especially iron. The characteristic absorbance spectrum of the dissolved iron complexes showed to overlap with the typical absorbance peak of DNA at 260 nm even at low concentrations and made analysis by absorbance based methods impossible. As iron is expected to bin and complexate the

phosphate groups in the backbone of nucleic acids, is is required to implement an extraction method that detaches the DNA form the dissolved and precipitated iron in the first place and then removes the iron from the solution to reduce interference with DNA analysis methods. In order to dissolve the precipitated minerals again, the pH of the extracted sample was lowered by addition of HCl, prior to mechanical destruction by homogenisation with silica beads. An inorganic phosphate buffer was used bind the iron complexed and purification of chimney and ocean samples was most efficient in a combination of centrifugal filter tips and SnakeSkin for upconcentration of DNA and desalting of the samples. Even though, it was due to technical limitations not possible to assess the iron concentration in the samples after purification, the procedure had a positive effect on the extraction efficiency and its reproducibility.

Interdiction of dissolved DNA into the ocean showed clearly detectable DNA in the chimney sample after extraction while almost complete depletion from the ocean. This suggests that the DNA form the ocean either gets incorporated into the mineral structures during precipitation or gets adsorbed to the surface after the chimney is established. Initial concentrations, however, still indicated higher amounts as the combined quantity of ocean and chimney extract together. This might probably indicate insufficient extraction from the emerging minerals or probably even a destruction of DNA due to hydrolysis in the proximity of the high pH alkaline fluid. Comparison of the chromatographic peak profiles obtained from Bioanalyzer measurements, for the chimney sample and the initial ocean mixture, no clear length dependency can be observed qualitatively. While fewer peaks of the incorporated 100–10,000bp ladder are present for the range between 5000–10,000bp, a similar trend can already be observed in the initial sample, which might on the one hand be due to the weaker resolving power of the instrument for longer strands, but probably also because of hydrolysis/destruction of longer strands during the extraction process. Although, reproducible results could be obtained for the extraction of chimney and ocean samples, that show a similar behaviour indicating DNA depletion from the ocean beyond the current detection limit, the chromatograms are still showing a broad variation amongst the peak intensity. This is most likely due to the difficult to control morphology of the chimney structures. Precise setting of the inflow rate with the syringe pump, canula diameter and position can ensure the growth of a chimney over just bottom accumulation of precipitate, however, the exact structure is hard to control reliably. This results in different morphologies such as multiple smaller growing tubes, larger thick tube or tubes with branching after ac certain height. This in turn leads to variation of mineral surface area available for adsorption and total mineral volume that potentially adsorb or incorporate dissolved DNA. This might also impact emerging gradients that could drive DNA towards the chimney strands by diffusiophoresis. In any case, these experiments were intended as a first test of the feasibility such alkaline vent models to study nucleic acid accumulation. To proof the mechanism and show potential length dependency, more experiments are required, alongside a more efficient extraction method to verify the total amount of initially incorporated DNA.

Follow up experiments published by Helmbrecht et al. [45], however, clearly showed the sequestration of dissolved RNA form a ferruginous ocean solution. The used setup differed from the one in the DNA experiments in several aspects. The ocean solution was contained in a 100 mL headspace bottle with cutoff bottom inside glovebox under inert nitrogen gas. This made it possible to simulate a more plausible prebiotic scenario, by using a minimal chemical composition for the ocean solution, only condition of dissolved iron(II) under anoxic conditions with no additional salts. The open bottle could therefore be used without the

problem of oxidation and provide a more natural injection of NaOH without the increasing pressure over time, as in the DNA experiments using a closed flask to limit oxidation. Also the larger flask provided a better representation of the bulk ocean volume, in which RNA could be sufficiently incorporated in the form of readily available yeast derived RNA powder. Using slow inflow rates, a chimney could be grown over the course of 90 min to reach a final height of about 3.5 cm. Periodic probing of the DNA level in the ocean, showed that most rapid RNA depletion happened during the first 10 min, when also the chimney gain in height the most rapidly. While control experiments without chimney growth could confirm a steady RNA level, extraction without addition of phosphate buffer show that no RNA could be recovered. This indicates that RNA is already bound to dissolved iron complexes. Since also most RNA is depleted during fastest growth of the chimney, this suggests that the strands get sequestered into the minerals by precipitation of the bound iron complexes. Most importantly, a double-sided t-test could confirm almost total RNA recovery form chimney and ocean after the experiment compared to the concentration measured in the initial ocean solution.

These findings also confirm the initial qualitative results shown for the DNA experiments. While initially assumed to be caused by an issue with the extraction form the ocean solution, it seems likely in the light of the RNA experiments, that also most of the DNA gets depleted form the ocean and sequestered into the chimney minerals with the iron complexes- leaving ocean extract choromatograms almost free of peaks while clearly showing strands of most lengths in the chimney sample. On the other hand, however, the comparison also clearly indicates, that a better and more efficient method for the extraction of DNA is required. Therefore, it might already be advantageous, to apply only a minimal ion solution to simulate a prebiotic ocean.

Considering the potentially emerging minerals in the applied systems, no characterisation has been attempted for the chimenys used in the DNA experiments. However, RNA experiments [45], showed a clear identification of white (amakinite) and green rust (fougerite) minerals precipitated from a ferruginous ocean solution. Although, the chimneys including DNA have not been grown under anoxic conditions, some conclusions on the potential minerals composition might be drawn from visual comparison and consideration of the applied conditions. **Figure 4.A.3 A-B** shows the oxidation after several minutes of a chimney grown form a ferrous-ferric ocean, while **C** used only injection of NaOH into a ferrous ocean and **D** show the same injection into the quasi-2-dimensional setup described in chapter 3. Considering the sample compositions it is likely that the while mineral precipitates are in fact amakinate that slowly morph into fougerite by oxidation in contact with dissolved oxygen in the surrounding water [57, 102]. Comparison with the findings shown in [88] suggest that further oxidation of green rust leads to the orange-brown solid of lepidocrocite that eventually further oxidises into the black magnetite after longer times. Based on the colour, these two seem likely for the material in the ferrous-ferric ocean, however, black structures might also stem from minerals based on the included sulphite from injected Na_2S.

The experiments shown suggest a accumulation and localisation of dissolved nucleic acids form and iron containing ocean solution during the alkaline precipitation of minerals. While the adsorption of nucleic acids in the context of the emergence of RNA has been studied in past publications [59, 71, 98, 99, 103] as a localisation mechanism, the sequestration into precipitating minerals might add an even more efficient mechanism for their accumulation and enhancement of local concentration. Additionally, this could even add alkaline hydrothermal vents as alternative location for nucleic acid concentration apart from the widely pro-

posed wet-dry cycles in warm little ponds [104, 105]. In the origin of life context of alkaline hydrothermal vents [22,24,25], this could add another aspect making them plausible location for the first biological systems to emerge and thereby support the hypothesis that alkaline vents could accumulate nucleic acids [97].

4.5 Conclusion

The experiments investigated the possible ways to incorporate nucleic acids into laboratory recreations of alkaline vents, in order to study their potential accumulation. Experimental setup using injection of an alkaline fluid into a container containing an iron-rich ocean solution support the formation of chimney-like tubular structures in a wide range of flask volume, but the potential limitation due to restricted geometry needs to be considered. While initial experiments suggested the accumulation of DNA on emerging minerals qualitatively, follow up experiments could confirm efficient RNA sequestration form a ferruginous ocean solution. These findings show that alkaline vents have the potential to concentrate and localise dissolve nucleic acids form a diluted ocean. Since all chemical processes at the origin of life require sufficient concentrations of starting material, this could pose a possible solution to the so called ”concentration probelm” [10].

Addendum 4

The following sections provide additional data and information that support and complement the results described in the experimental section.

4.A Desalting Efficiency

As the ocean solution as well as the alkaline fluid use high concentrations and high amounts of dissolved salts and iron, DNA analysis can be impacted by common analysis methods, especially the ones based on absorbance and fluorescence. The impact of dissolved iron complexes on DNA analysis efficiency in the solution is shown in **Figure 4.A.1** for extraction of DNA form the different media.

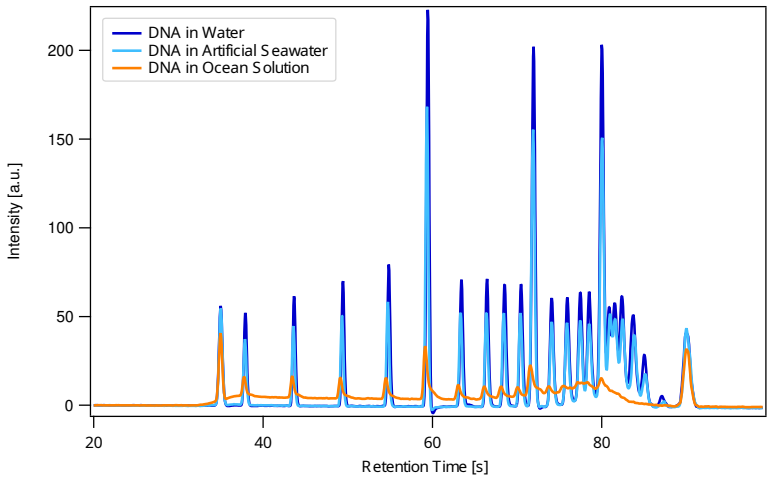

Figure 4.A.1: Comparison of DNA extraction form different media. 10 ng µL^{-1} DNA ladder (10–10,000bp) is extracted by addition of phosphate buffer protocol with one concentration and one "washing" step in centrifugal filter tips. Bioanalyzer traces show significantly lower results for for extraction from a solution containing 75 mM Fe(II)Cl_2 compared to extraction form water or artificial seawater.

Even after 2 desalting/washing steps of the recovered samples, extraction from an iron containing solution showed significantly lower amounts in Bioanalyzer analysis despite equal initial DNA concentration in all solutions. Already extraction form artificial seawater shows lower peaks as from pure water.

An efficient desalting methods seems therefore necessary prior to analysis of extracted DNA. In **Figure 4.A.2** the efficiency of ion reduction in a solution of 105 mM Fe(II)Cl_2 is shown for different methods.

While filtering steps with centrifugal filter tubes usually include an increase in DNA by concentration of the sample, this also leads to slightly higher ion concentrations of dissolved

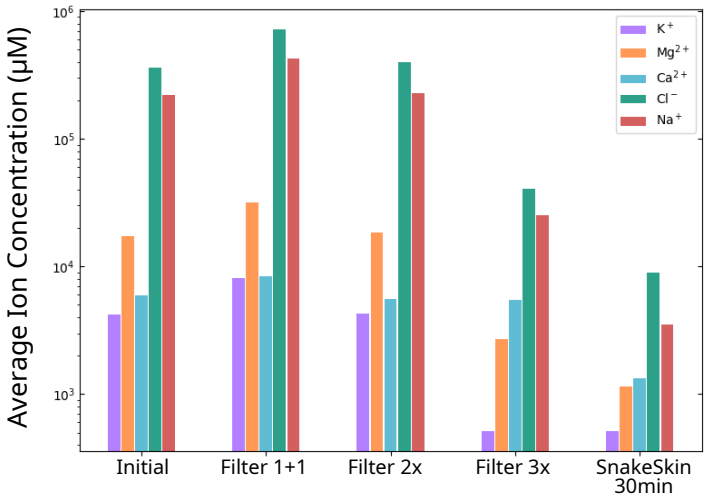

Figure 4.A.2: Desalting efficiency of different protocols. Samples containing 105 mM Fe(II)Cl_2 in artificial seawater are desalted with centrifugal filters or SnakeSkin. The 1+1 filter step applied the addition of more sample to the filtrate and repeated gentrification as usually applied to increase DNA amount. 2x or 3x filter steps used one concentration step followed by 1 or 2 additions of water and repeated gentrification to desalt the sample. Most efficiency, however, showed SnakeSkin with immersion in 500 mL water for a minimum of 30 min. Ion concentrations were measured using ion chroatography.

salts. However, addition of water to the filtrate and repeated gentrification can ”wash” and therefore desalt the sample. The most effective method, however, showed to be so called SnakeSkin tubes that, immersed in large volumes of water, promote diffusion of ions out of the sample.

4.A.1 Emerging Minerals

Although the no detailed characterisation or analysis of the emerging minerals has been conducted, the observation of colour and comparison with the findings in [45, 88] might give some clues. As shown in the publication by Helmbrecht et al. [45], injection of NaOH into an ferruginous ocean formed white rust (amakinite) that slowly oxidised into green rust (fougerite). Fougerite, in turn, can further oxidise into lepidocrocite (orange-brown) that eventually oxidises to magnetite (black) [59].

Figure 4.A.3 A and B shows a chimney grown from a ferrous-ferric solution by injection of NaOH + Na_2S at two subsequent time points. The initial greenish black solid starts to get orange edges suggesting oxidation in contact with the surrounding water. Based on the description in [88], this could be parts of green rust that oxidise to lepidocrocite. However, due to the injection of Na_2S probably also other minerals emerged in the process.

In **Figure 4.A.3 C** a completely white mineral structure formed upon the injection of NaOH into a ferrous ocean under limited exposure to oxygen by preflushing of all vessels with inert argon gas. As similar conditions are given as reported by [45], this is very likely white rust (amakinite) that would have morphed into its green rust phase after some time. Data for colour changes after longer times are unfortunately not available.

Lastly, **Figure 4.A.3 D** shows structures forming upon injection of NaOH + Na_2S into a ferrous ocean using a microfluidic device as described in chapter 1. Initially forming white precipitates turn green after prolonged contact with the surrounding water. this could indicate potential oxidation of white rust to green rust due to dissolved oxygen in the ocean solution.

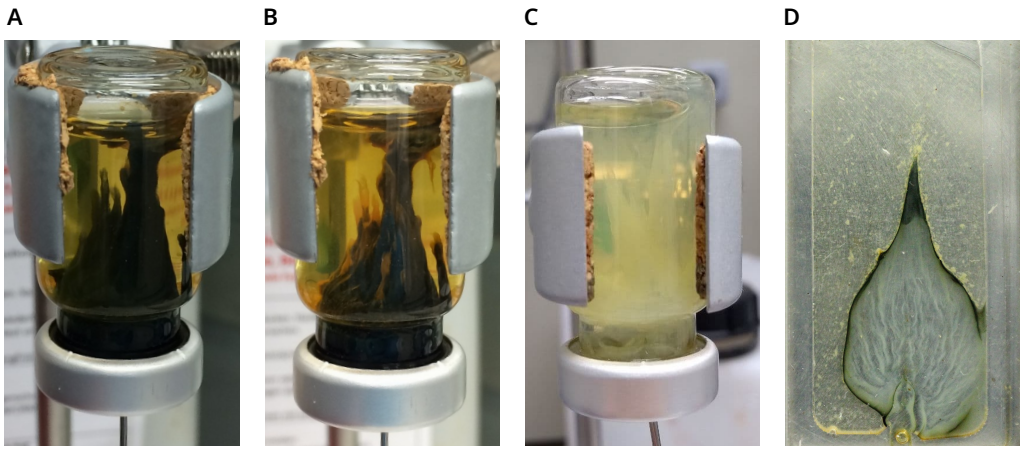

Figure 4.A.3: Emerging minerals and their oxidation. **A**) Chimney grown from a ferrous-ferric solution by injection of NaOH + Na_2S after formation and **B**) after several minutes. **C**) Mineral structure formed upon the injection of NaOH into a ferrous ocean and **D**) Structures forming upon injection of NaOH + Na_2S into a ferrous ocean using a microfluidic device.

All these, however, only present estimations based on on observation on the colours of the emerging precipitates. For a definitive characterisation, thorough analysis with RAMAN spectroscopy or Scanning Electron Microscopy (SEM) would be necessary.

Chapter

5

Nucleoside Synthesis from Early Organic Building Blocks in Dynamic Environments

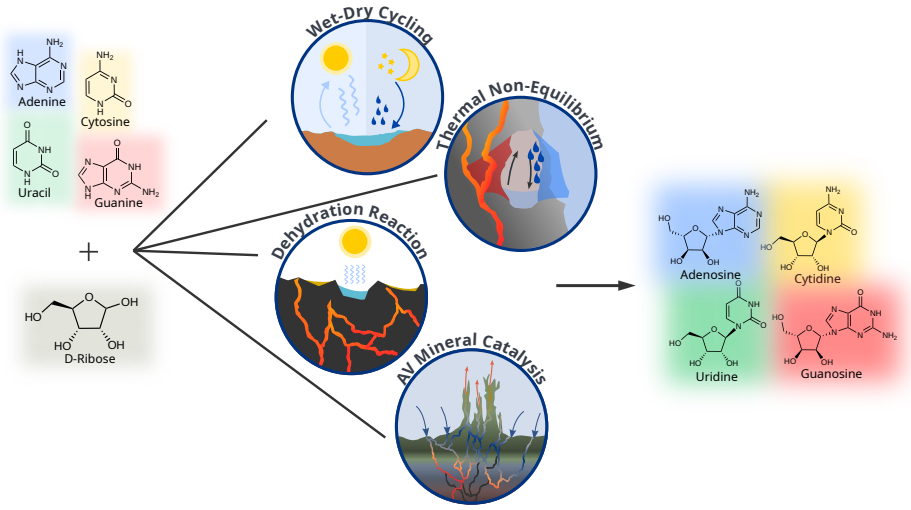

Summary: One key requirement for modern life are the information storing polymers RNA and DNA. Nucleotides, which are build up from nucleosides and phosphate, make up the structure of RNA and DNA.. Their synthesis from prebiotic feed-stock molecules, however, is challenging and approaches by various scientist have not yet found a universal pathway for all of the nucleosides in sufficient yield.

Prebiotic nucleoside synthesis was first explored in the early 60s and puzzled scientists since then [106–108]. This chapter explores the formation of RNA-nucleosides form its primary building blocks, nucleobase and D-ribose under various conditions and parameters to give an overview of potentially positive effects on the synthesis. As a first steps, the catalytic capabilities of alkaline vent minerals were studied upon addition to the reaction mixture. Further, thermal non-equilibrium, dry-state reaction and wet-dry cycling are studied. Besides those different conditions, the addition of carbonate and amino acids was probed, together with the influence of the temperature of the sample. The experiments are intended to screen many possible conditions and assess the results for starting conditions of future studies.

To analyse the samples and characterise the nucleosides High Performance Liquid Chromatography (HPLC) together with Orbitrap Mass-Spectrometry was used. Obtained α- and β-nucleosides where distinguished by comparison to standards.

5.1 Introduction

Information storing molecules are the backbone for the complexity of life as we know it today. Long RNA and DNA polymers are storing the blueprints for protein-biosynthesis, that forms the matter of life. The long biopolymers therefore apply a four letter code that is built on their four different monomeric subunits, the nucleotides, respectively. Nucleotides, in turn, consist of 3 precursor molecules, namely a nucleobase, a sugar and a phosphate group. Nucleosides, the simpler precursor of nucleotides, only consist of nucleobase and sugar.

While it is clear that both RNA and DNA fulfil major functions in modern life, it is anticipated that RNA played a major role along the emergence of genetic information and acted as a precursor molecule [96]. The so called RNA world hypothesis [38] therefore proposes an information-first approach, according to which RNA would have emerged from a diluted prebiotic soup as one of the first molecules for the evolution of life. This scenario benefits from the two major capabilities of RNA: On the one hand, it offers the capability to store and transfer genetic information, but is on the other hand also able to catalyse its own replication [109, 110]. Even though there are some limitations to this theory, especially when is comes to peptide genesis, it is well established that RNA must have played an important role in one way or another [96, 108].

Most of the attempts to find possible ways for prebiotically compatible RNA synthesis, start form the assembly of nucleotides form their three principal building blocks: base, sugar and phosphate [63, 106, 111, 112]. There have been found plausible origins of nucleobases on earth by either synthesis under UV exposure [113], delivery from meteorites [114, 115] or under the reducing conditions of alkaline hydrothermal vents [116]. The assembly, however, to first nucleosides together from D-ribose and their respective nucleobase poses one of the most challenging hurdles in prebiotic chemistry [96, 108] and is therefore often referred to as the "nucleoside problem" [107]. The linkage of ribose and a nucleobase requires a condensation reaction to form a glycosidic bond between the 1'C of ribose and either the 9N atom in purines or the 1N atom in pyrimidines. This reaction, however, is thermodynamically not favoured, usually resulting only in low yields for the uncatalysed reaction [108, 112, 117].

Some of the first approaches on the building block assembly were carried out by Orgel and coworkers [63, 111], who showed successful synthesis of purine nucleosides in the presence of various salts, but still achieved maximum yields of around 10 %. Alternative reaction pathways tried to circumvent this hurdle by multistep reaction pathways using an en route formation of the ribose [117] to achieve the synthesis of pyrimidine nucleotides, however only precursors of purine ones [118]. Also other approaches succeeded mostly only in one of the syntheses at at time, either for pyrimidines [117, 119] or purines [120], and so far only one path exists that could produce both [121].

All those pathways, however, only considered "ideal" conditions in the laboratory so far [122]. From an origin of life perspective, it is required that all single steps along the path to information storing molecule are compatible at the end and not only work in an isolated environment. This means on the one hand, that all potential synthesis reactions need to proceed in a prebiotically plausible environment [8, 122]. On the other hand, they also need to be compatible with the conditions necessary for any preceding or succeeding steps. In the case of nucleoside synthesis, this means that the proposed pathways at some point should have possibly functioned in the same environment and at least under comparable conditions as the processes forming the precursor molecules and especially following phosphorylation and polymerisation steps that connect nucleotides into longer chains. In any case, at the

moment none of the available pathways yields a sufficient approach towards the emergence of RNA [108, 123].

The following chapter is approaching the synthesis of nucleosides from their primary building blocks under different dynamic conditions. The idea, however, is not to start from the classical "mechanistic" chemical point of view, but rather form a combinatorics angle. The polymerisation of RNA has already been reported in sufficient yields under multiple conditions [11, 72, 104]. Therefore, the glycosidic bond formations, is not only studied in different physical conditions, but also applying a multitude of combined chemical settings, that haven been shown to work for subsequent polymerisation of RNA [11, 72, 124] or would be useful for subsequent phosphorylation of nucleosides due to the presence of phosphate [124].

The experiments will explore the impact of different physical conditions on the formation of nucleosides form their principal building blocks. Those include mainly a dynamic non-equilibrium setting at an air-water interface subjected to a temperature gradient, wet-dry cycling of reaction mixtures containing different additives as $MgCl_2$, TMP and NH_4Cl. Those will be compared to the classical approaches of a dehydration reaction on a heat plate, but studied at different temperatures and under the addition of K_2CO_3 and some amino acids. Lastly, the potential catalytic effects of green rust, preformed as chimney and added to the reaction mixtures as powder are tested at moderate temperatures (80 °C) comparable to alkaline vents. The analysis is carried out by high-resolution HPLC-Orbitrap MS and places the focus not only on effective yields of the desired β-ribonucleosides, but also on their ratio to the corresponding and co-forming α-anomers. All yields are calculated in reference to the starting concentration of the nucleobase.

5.2 Results

The following experiments are based on some of the first approached to prebiotic nucleoside synthesis done by Orgel and coworkers [63, 111] in 1972. While starting form a similar chemical compositions using a mixture of nucleobases and D-ribose in 15-fold excess, the reaction will be carried out under different environmental conditions and chemical additives. The exact choice of conditions is thereby intended to screen for a possible combinations that is compatible with subsequent steps along the way to RNA, e.g. the polymerisation of nucleotides. Starting from the usual dehydration reaction, it is tried at lower temperature, in dynamic wet-dry cycling conditions, in evaporation-condensation cycles and under the influence of reactive green rust surfaces. Additionally, several different additives, like salts and amino acids, that turned out to be helpful for polymerisation, are incorporated in the reaction mixture.

5.2.1 Green Rust Catalysis

To study the potential catalysing effects of green rust on the formation of ribonucleosides, pulverised minerals are added to a low concentration reaction mixture (1 mM nucleobase concentration). The minerals have been obtained form injection of NaOH into a ferruginous solution. The resulting chimney-like structures have been dried under anoxic conditions and pulverised. Approximately 3.8 mg were then added to the sample solutions containing 1 mM nucleobase, 15 mM D-ribose and 10 mM $MgCl_2$. The samples were adjusted to pH 10

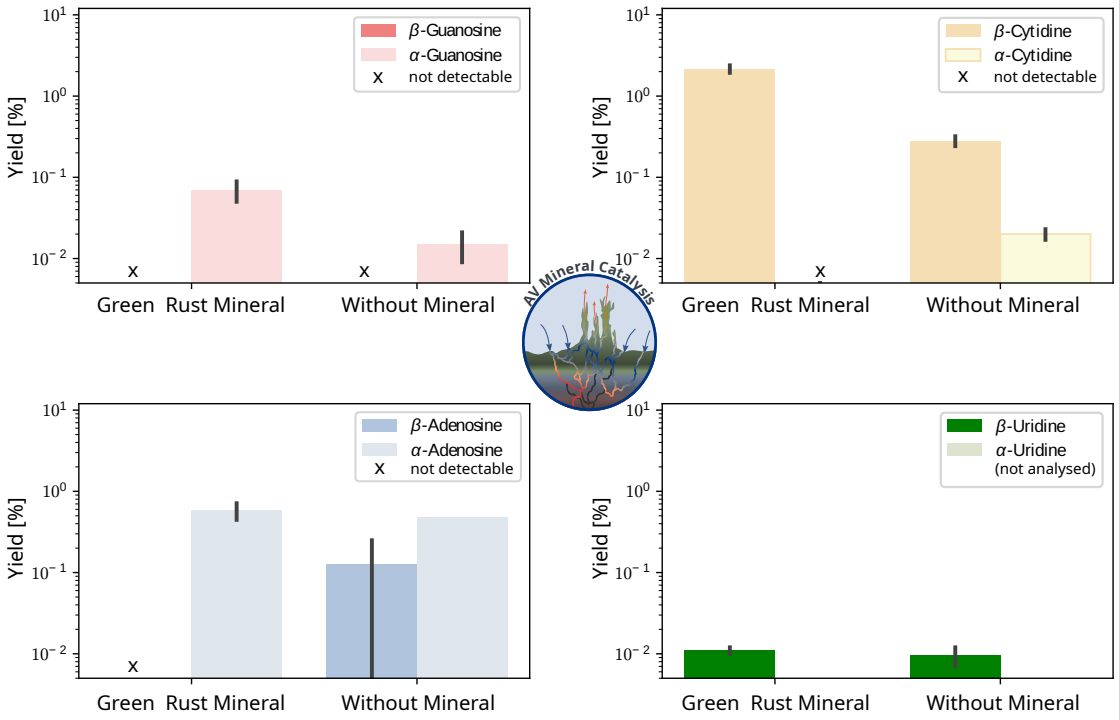

Figure 5.1: Nucleoside synthesis in the presence of alkaline vent minerals. 1 mM of each nucleobase reacted with 15 mM D-ribose in the presence of 10 mM $MgCl_2$ and with or without the presence of ∼3.8 mg of dried and pulverised chimney mineral (mostly green rust and its oxidation products). All samples were dried in test tubes at 80 °C for 20 h). Relative yields for α- and β-nucleosides were calculated with respect to the nucleobase starting concentration.

prior to mineral addition. All samples, with and without minerals, were evaporated in open 1.5 mL test tubes in an aluminium sample block at 80 °C with continued heating for 20 h.

Reaction yields are shown in **Figure 5.1** and calculated with respect to the nucleobase concentration in the initial sample. All of the four canonical nucleosides show overall low yields beyond 1%. β-guanosine could not be detected in either sample, with or without mineral, its anomer, however, α-guanosine was observed at slightly higher concentration with mineral. Cytidine reached comparable yields for its β-form under both conditions, with slightly higher results in presence of the mineral, which made it the only nucleoside reaching a yield above 1%. While similar yields have been detected for α-adenosine and β-adenosine without mineral, the latter could not be detected in the presence of the mineral. Similarly to guanosine, α-adenosine formation seemed to be enhanced with mineral. Uridine showed insignificant, but comparable yields in both cases. α-uridine could not be analysed due to the lack of an authentic standard.

5.2.2 Air-Water Interfaces in Thermal Non-Equilibria

Continuous highly dynamic evaporation-condensation cycles are generated by temperature gradient across a thin enclosed chamber of 500 µm. Air-water interfaces within the chamber exhibit a highly dynamic behaviour of ongoing evaporation and condensation as described

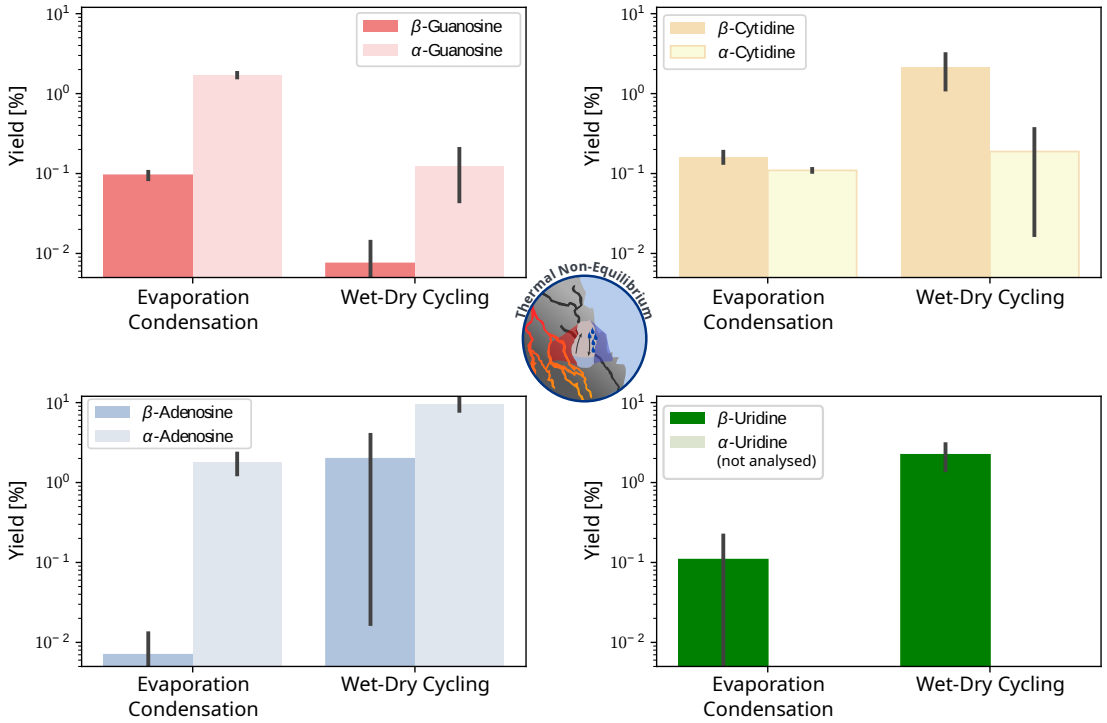

Figure 5.2: Nucleoside formation at at air-water interfaces in a temperature gradient. 1 mM of each nucleobase reacted with 15 mM D-ribose in the presence of 10 mM $MgCl_2$. All samples were incorporated in a microfluidic chamber hosting an air water interface in a temperature gradient of 20–80 °C for 20 h or subjected to a total of 3 wet-dry cycles (80 °C evaporation and rewetting after 20 h). Relative yields for α- and β-nucleosides were calculated with respect to the nucleobase starting concentration.

in section 2.3.2. This facilitates further the concentration of dissolved species at the warm side of the air-water interface, where it is subject to periodic drying and rewetting. Because of the active concentration mechanism the sample solution will be prepared at low concentration of 1 mM nucleobase and 15 mM D-ribose at pH 10. While the mircofluidic chamber was operated in a gradient between 20 °C (cold) and 80 °C (hot) for 20 h, the control samples were subjected to 3 wet-dry cycles at 80 °C with rewetting after 14 h.

Figure 5.2 show the yields for α- and β-form of the four canonical nucleisides. At least small amounts of nucleosides could be detected in all samples. For the samples run in the continuous evaporation-condensation system, a clear excess of the α-form nucleosides is shown for guanosine and adenosine, reaching slightly more than 1% in both cases. While the amounts of β-adenosine are was only barely above the detection limit, clear detection of guanosine was possible for synthesis in a temperature gradient, showing an almost ten-fold higher value as for the sample obtained from wet-dry cycling. Lastly, cytidine showed about equal yields for both forms with no significant preference, but still less than 1%. Apart from guanine, all other nucleosides showed lower yields in the samples subjected to a temperature gradient. α-uridine could not be analysed due to the lack of a commercially available standard.

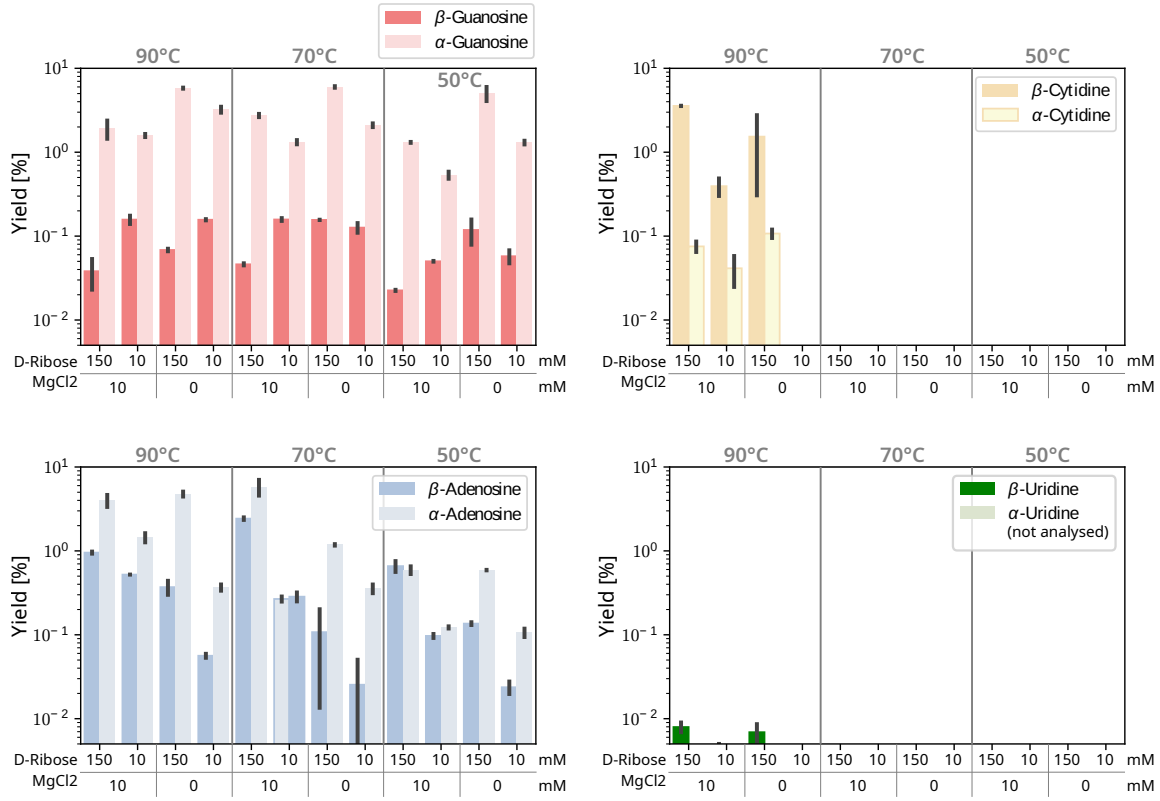

Figure 5.3: Dehydration reaction in the presence of K_2CO_3 at different temperatures. 10 mM of each nucleobase reacted with either 10 mM or 150 mM D-ribose in the presence of either 10 mM or no $MgCl_2$ in the presence of 100 mM K_2CO_3. All samples are dried at 90 °C, 70 °C and 50 °C for 20 h. Relative yields for α- and β-nucleosides were calculated with respect to the nucleobase starting concentration.

5.2.3 Temperature, Carbonate and Amino-Acids in Dehydration Reactions

As already attempted by Orgel and coworkers [63, 111], dehydrating conditions are the most likely conditions that could overcome the thermodynamically unfavoured glycosidic bond formation to link nucleobase and ribose [96, 107]. The following conditions start from Orgels early work on nucleoside synthesis and try the dehydration reactions under different conditions, such as temperature, salts and the additions of amino acids.

The first experimental set described below focused on the addition of carbonate in the form of K_2CO_3 (100 mM) to the reaction mixture. Additionally, all the synthesis of all four canonical nucleosides was tested with and without $MgCl_2$ (10 mM) and D-ribose in equal amount or in 15-fold excess to the base concentration (10 mM). All samples are evaporated in petri-dishes on a heat-plate at 90 °C, 70 °C and 50 °C respectively.

The results of the screening of carbonate under varying temperature, magnesium and ribose concentration is shown in **Figure 5.3**. The reactions of Cytosine and Uracil failed to produce any detectable amount of nucleosides for lower temperatures (70 °C and 50 °C), while adenine could be detected with overall low yields decreasing with temperature. The formation of guanosine did not show a dependency with temperature, however, yields were very low overall and far beyond 1%. Further, guanosine showed a clear excess of its α-form un-

der all conditions (>1%) in all samples with a slight tendency to higher yields in the absence of magnesium. The reverse effect could not be observed for β-guanosine. All nucleosides, except guanosine, showed lower yields for low ribose concentrations (equal to the nucleobase) as well as for the absence of magnesium in the reaction mixture. Cytosine could be contained in considerable yields above 1% at 90 °C, whereas uridine only showed negligible but similar yields with and without magnesium. α-uridine could not be evaluated since no commercial standard was available for the molecule.

The next experiments was attempted to test the implementation of amino-acids as potential catalysts. The screening was only done for the synthesis of guanosine its complementary nucleoside cytidine, as separate reaction mixtures (10 mM nucleobase) as well as in a mixture of both (5 mM of each nucleobase). All samples contained 150 mM of D- ribose and 40 mM of valine, lysine, proline or $MgCl_2$ respectively, where the latter is intended as control sample without amino-acid. The final smaple was then adjusted to pH 10. Again all mixtures were evaporated in petri-dishes on a heat-plate at 80 °C and 70 °C. The relative yields of guanosine and cytosine are shown in **Figure 5.4**.

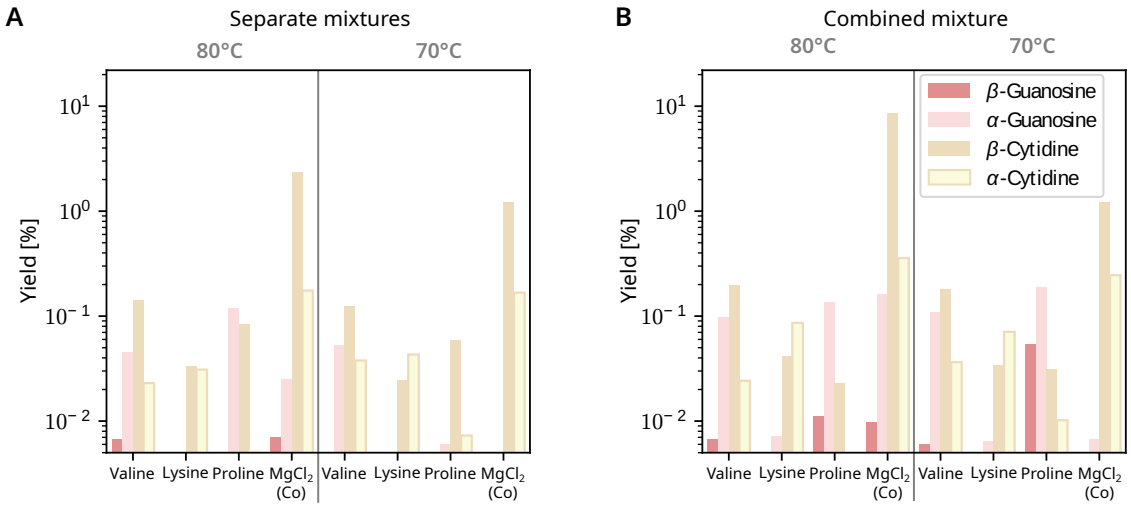

Figure 5.4: Dehydration reaction in the presence of valine, lysine and proline at different temperatures. 10 mM of either guanine, cytosine or 5 mM of each are reacted with 150 mM D-ribose in the presence of either 50 mM valine, lysine, proline or 40 mM $MgCl_2$ at initial pH 10. All reaction mixtures were evaporated at 80 °C with continued heating for 20 h. In **A**) the obtained yields are shown for separate reaction mixtures of guanine and cytosine, whereas **B**) shows the yields form co-formation in a combined mixture of the two. Relative yields for α- and β-nucleosides were calculated with respect to the nucleobase starting concentration.

Overall consideration of the plotted yields suggests no significant change form 80 °C to 70 °C, tendentiously yields, however, are slightly lower for lower temperature. β-guanosine could not be detected when reacted in a separated mixture with D-ribose at 70 °C. What can be seen from comparison of the plot for separate reaction mixtures and a combined mixture of guanine and cytosine, are higher overall yields for β-guanosine formed in the presence of cytosine. Cytidine shows overall lower yields in the presence of amino-acids compared to the presence of magnesium. In the latter case, however, yields are slightly higher in the presence of its complementary nucleoside.

5.2.4 Wet-Dry Cycling

Wet-Dry cycles have the capability to enhance the dynamics of a reaction compared to static heating in an aqueous solution. By repeated evaporation, dry-state heating, rewetting and renewed evaporation the phase transitions of the dissolved molecules in the usual dehydration reaction can be repeated multiple times over the course of the experiment's time. For the experiments low concentration reaction mixtures (1 mM nucleobase concentration with 15 mM D-ribose) are selectively mixed with 10 equivalents (10 mM of$MgCl_2$, TMP and NH_4Cl respectively and combinations of the three. This gives a total of 8 different conditions fore each sample.

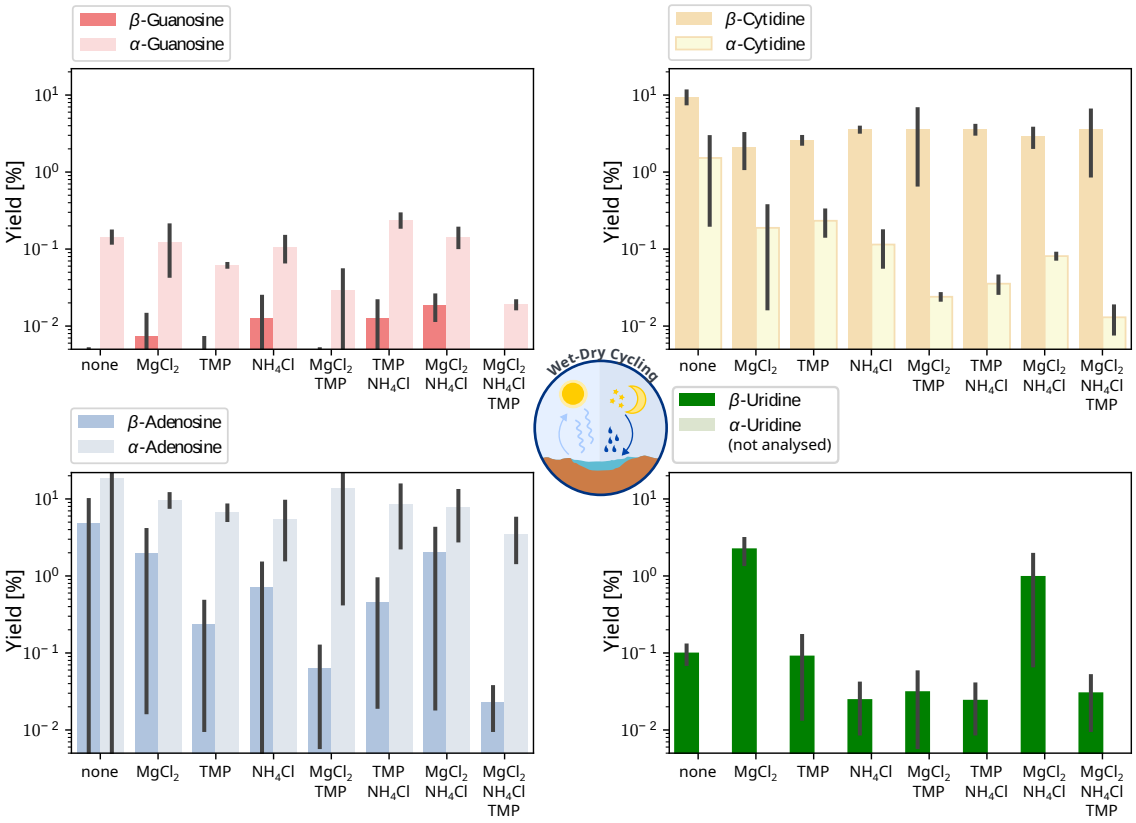

Figure 5.5: Synthesis of four canonical nucleosides under wet-dry cycling. 1 mM of each nucleobase reacted with 15 mM D-ribose in the presence of either 10 mM $MgCl_2$, NH_4Cl, TMP or combinations of the three at initial pH 10. Three cycles of drying at 80 °C and rewetting after 14 h were completed. Relative yields for α- and β-nucleosides were calculated with respect to the nucleobase starting concentration.

Apart from screening for canonical and singe nucleobases only, also non-canonical nucleobase hypoxanthine is studies aside the co-synthesis of mixtures of to complementary bases is investigated. The combinations therefore were adenine with uracil, guanine with cytosine and hypoxanthine with cytosine. All samples are prepared ad pH 10 and were heated in multi-well-plates to 80 °C. The solutions underwent a total of 3 cycles (3 dry and wet states)

with a cycle duration of 14h. After each cycle the samples were redissolved in nuclease-free water and evaporated again.

The results and relative yields are plotted in **Figure 5.5**. Overall all nucleosides could be detected for all conditions, except β-guanosine, was below detection limit for several of them. β-cytosine showed clear yields above 1% comparable for all conditions with a tendency to decreased amount of α-cytidine the more TMP, $MgCl_2$ and NH_4Cl are added to the sample. Uridine shows clearly identifiable yields, reaching even more than 1% when magnesium or TMP and ammonia were present. Adenine showed quite high excess of α-adenosine, reaching continuously average yields of 5-10%. Its β-form also reaches yields above 1%, however, yields seem to drop as soon as TMP is incorporated into the samples. Lastly, guanosine shows the usual excess in α-form, yields for the β-form very low. No molecule could be detected for the uncatalysed reaction and similar to adenosine, yields seemed even lower in the presence of TMP.

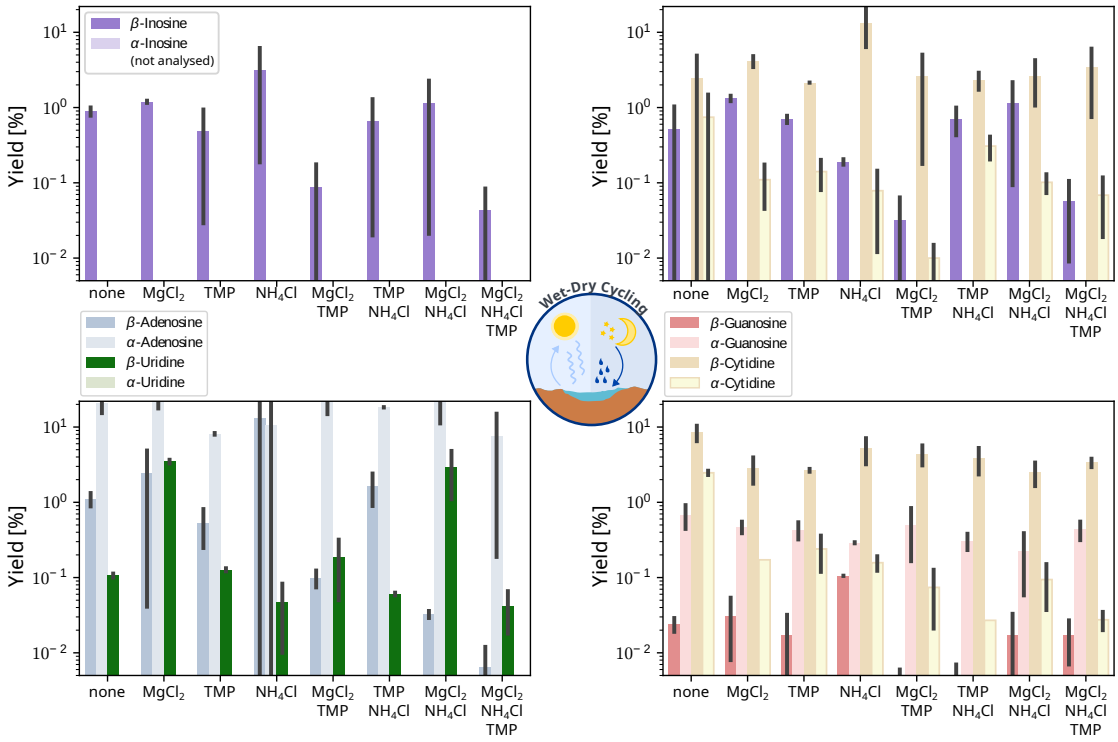

Figure 5.6: Synthesis of inosine and co-synthesis of complementary nucleobases in wet-dry-cycling. 1 mM of each nucleobase reacted with 15 mM D-ribose in the presence of either 10 mM $MgCl_2$, NH_4Cl, TMP or combinations of the three at initial pH 10. In samples studying the co-formation of two nucleosides, 10 mM of each nucleobase was added to the reaction mixture. Three cycles of drying at 80 °C and rewetting after 14 h were completed. Relative yields for α- and β-nucleosides were calculated with respect to the nucleobase starting concentration.

Apart form the individual samples for all the canonical nucleobases, this experimental set also included the non-canonical nucleobase hyopxanthine as well as mixtures of the canonical nucleobases. The additional yields are plotted and shown in **Figure 5.6**. The yields for inosine, the corresponding nucleoside to the base hypoxanthine, was clearly detectable un-

der all conditions and shows significant yields around and above 1%. Similar to adenosine and guanosine in **Figure 5.5**, the lowest yields have been reached from all the samples that contained TMP in the initial mixture. The values overall seem to be consistent with the co-formation of Cytidine in the combined mixture and do not show any noticeable in- or decrease. The amount of *alpha*-inosine could not be assessed due to the lack of a commercial standard. Inspecting the cytidine yields in the mixture with inosine, a similar behaviour is observed. The overall yields are consistent with the ones obtained form the single mixture and show no significant change, however also none of the two nucleosides shows a significant negative impact on the formation of the other one. The same is applicable to the mixture with guanosine. For β-guanosine itself, however, it appears that overall yields were improved in the presence of cytosine, even though the amount is still low quite low. Same can be observed for α-guanosine, as it also exhibits slightly increased yields across all conditions. Finally, the yields for combined formation for adenosine and uridine, also seemed barley impacted by co-formation with each other. The overall yield profiles look mainly similar to the ones obtained from the single sample mixtures with probably slightly increased average yields.

5.3 Materials and Methods

For the testing of nucleoside synthesis under various conditions, different experimental approaches are applied. Periodical evaporation-condensation cycles are studied in a custom build flow cell that allows the precise control of temperature gradients across the thickness of the chamber. The dehydration reactions are carried out in petri-dished on a heat plate, while the wet-dry cycling is done in 96-multi well-plates. Lastly, the incorporation of alkaline vent minerals is accomplished by adding a fixed amount of dried and pulverised mineral to the samples in test tubes to evaporate them to dryness on a digital heating block. All samples have been studied with 15-fold excess of D-ribose over the nucleobase.

5.3.1 Sample Preparation

Fresh solutions of ribose and nucleobases were prepared for each experimental run to avoid degradation in aqueous solution. For experiments using 10 mM nucleobase concentration in the final sample, adenine, guanine, uracil (all Sigma-Aldrich, USA) and cytosine (Carl Roth, Germany) were dissolved in nuclease-free water (Invitrogen, Thermo Fisher Scientific, USA) to the final concentration. As the nucelobases are hard to dissolve, the solutions were stored in a closed 1.5 mL sample tube and sonicated (Elmasonic P, Elma, Germany) at 30 °C for 29 min. All remaining chemicals as D-ribose (Carbosynth, UK), magnesium chloride [$MgCl_2$], potassium chloride [KCl], calcium carbonate [K_2CO_3], ammonium chloride [NH_4Cl] or sodium trimetaphosphate [$Na_3P_3O_9$] (all Carl Roth, Germany) were weight into one sample tube and then dissolved with the prepared solutions of the respective bases. For all other experiments using a lower final base concentrations, higher concentrated stock solutions were prepared for each compound and then pipetted together proportionally, in order to get the desired final concentration. Added amino acids; valine, lysine (Sigma-Aldirch, USA) and proline (Fisher Scientific, USA) were dissolved in nuclease-free water as stock solutions at 100 mM or 250 mM.

For pH adjusting of the samples a micro pH electrode (Orion Star A211, Orion Instruments, Thermo Scientific, USA) was used together with 1 M volumetric standard solutions of NaOH or KOH or HCl (Carl Roth, Germany).

5.3.2 Evaporation-Condensation Cycles in Thermal Non-Equilibrium

A custom built microfluidic device is constructed, so that it can host two cells of 11 mm width and 16 mm height with a thickness of 500 µm. The chambers itself is constructed in a similar way as described in **Figure 3.6** in chapter 1. It is built up form a Fluorinated ethylene propylene (FEP) sheet that is squeezed between two sapphire plates. The FEP sheet sets the thickness and hosts a cutout of the two rectangular chambers including inlet and outlet channels, made by a two-dimensional plotter (CE-6000, Graphtec, Japan) according to drawing created with the aid of a CAD software (Inventor 2021, Autodesk, USA). Additionally, an ultra-thin FEP sheet (50 µm is placed between the lower sapphire the FEP cutout to provide a hydrophobic surface on the inner side of the chamber, that will later be cooled. The assembly is held together by a steel frame that is screed tightly onto an aluminium base with six M2 screws. The bottom sapphire as well as aluminium base, have four holes aligning with the channel in the FET cutout and therefore allow microfluidic access to the two chambers (one inlet and outlet each). Through threads in the holes of the base, Polytetrafluorethylen (PTFE) tubings with an inner diameter of 180 µm are connected with standard low-pressure fittings and ferrules.

For each experiment the chambers are filled with to approximately $\frac{2}{3}$ of their height with the sample solution to allow sufficient evaporation and condensation. To fill in the samples, a high-precision syringe pump (Nemesys S, Cetoni, Germany) is equipped with a 1 mL glass syringe (SETonic, Germany) an connected to the top outlet of one of the chambers. A tubing connected to the lower inlet of the chamber is placed within a vial with the samples solution while volume is retrieved with the syringe pump at flow rate of 2 mL h^{-1} until the fluid front can be seen at the junction between inlet channel and chamber interior on the FEP cutout. Then a fixed volume of 50 µL is sucked into the chamber. After the filling process is completed, all tubings connected to the chamber are sealed tightly with end-caps, so that no liquid can evaporate outside the chamber.

To ensure sufficient heat conduction, the aluminium base and the top sapphire are covered with a thin graphite foil and then connected to an aluminium back panel that is cooled by a heat bath (R52, Grant Instruments, UK) to 10 °C. On the top part of the chamber, an aluminium block with electrical heater set to 80 °C is screwed on, so that is tightly presses on the graphite foil to the top sapphire. The experiment is then run for 20 h in this configuration.

After completion of the experiment, heating block is detached and the chamber removed from the cooling plate. Now the bottom tubing of the chambers is places in a sample collection tube and air is pushed through the upper channel to flush the sample from the chamber to the tube.

5.3.3 Mineral Catalysis

Alkaline vent chimney are grown under anoxic conditions in a glovebox (MBraun, Germany) from a ferruginous ocean containing 100 mM $Fe(II)Cl_2$ with an injection of 100 mM NaOH. After the chimney was completed, the remaining ocean has been retrieved and the chimney precipitates were dried under inert gas (nitrogen). The dried mineral has then been roughly pulverised with a spatula and (3.8 ± 0.4) mg were added to each sample tube. Then 200 µL

of the premixed sample solutions was pipetted on top of the minerals and the mixture was vortexed. All tubes have then been placed in a aluminium block heater and heated at 80 °C with open lid for 20 h. After finishing the experiment, all samples were resuspended in 200 µL of nuclease-free water, vortext an centrifuged. The supernatant was then analysed by HPLC-Orbitrap MS.

5.3.4 Dehydration Reactions

Aliquotes of 200 µL volume of each sample solution were pipetted onto a petri-dish of 40 mm diameter and placed on a heat plate (Heidolph, Germany) at 80 °C. The solution evaporated to dryness within 2 min and was then heated for 20 h. Afterwards, the dried sample was resuspended in 1 mL of nuclease-free water, dissolved by repeated motion of the pipette and then measured by HPLC-Orbitrap MS.

5.3.5 Wet-Dry Cycling

For wet-dry cycling 100 µL of experimental samples were directly mixed in 96-multi well-plates with flat bottom form concentrated stock solutions to 1 mM final nucleobase concentration. Stock solutions have been adjusted to pH 10 individually to give a final pH of 10 of the sample solutions after mixing by repeated pipetting motion in the wells. The well plates have been placed on an aluminium block that was directly flush with the bottom of the wells and placed on a heat plate (Heidolph, Germany) at 80 °C well temperature, adjusted with with an infrared camera to get an homogeneous target temperature in each well. In total three wet-dry cycles were completed by rewetting of the dried samples with 70 µL nuclease-free water after 15–20 h, to dissolve the dried powder by perpetual pipetting motion within the well. Finally, the sample was redissolved in 100 µL nuclease-free water and prepared for analysis by HPLC-Orbitrap MS.

5.3.6 UHPLC-Orbitrap MS Analysis

All samples were analysed by ultra high performance liquid chromatography [UHPLC] (Vanquish, Thermo Fisher Scientific, USA) couples to an Orbitrap mass spectrometer [MS] (Q Exactive Plus, Thermo Fisher Scientific, USA). For chromatographic separation a C18 reversed-phase column (Waters Symmetry, Waters, USA) with 4.6x250 mm and 5 µm particle size was used and operated constantly at 30 °C. Water (eluent A) and acetonitrile (eluent B) were used as mobile phase and were modified by the addition of 0.1% formic acid (all Optima LC/MS Grade, Fisher Chemical, USA). Acquisitions was started with 0% B for the first 3 min then gradually increased to 5% B over the course of 4 min, followed by a sharp increase to 40% B within 0.05 min and held constant for 0.9 min. To clean flush the colum, a subsequent increase to 100% organic phase (B) within 0.05 min was held constant for 0.95 min, followed by a reset to 0% B within 0.05 min and continued for 3 min to re-equilibrate the column for the next measurement. The flow rate was kept constant at 0.3 mL min^{-1} for the total acquisition time of 12 min.

Mass acquisition on the orbitrap was running in parallel to the first 10 min minutes of the LC method. The instruments was operated in positive-ion mode acquiring Full MS scans in the range of 100–1500 m/z at a resolution of 140,000. The automatic gain control (ACG target) was set to 3e6 and a maximum integration time of 150 ms was applied. General instrument

parameters were set as follows: Sheath gas flow 2 L min^{-1}, auxiliary gas flow rate 0 L min^{-1}, spray voltage 2.9 kV, S-Lens RF level 50.0 and capillary temperature 320 °C.

5.3.7 Molecule Identification and Quantification

Target molecules are identified by mass and chromatographic retention time in comparison to authentic standards. Analysis of standard mixtures of different concentration were also used for quantification of resulting nucleoside amounts. All data have been analysed in the instrument manufacturers software (Chromeleon 7, Thermo Fisher, USA). Commercial standards have been available for the following molecules: β-cytidine, β-guanosine, β-adenine, β-uridine and β-inosine (all Sigma-Aldrich, USA) as well as for α-cytidine, α-guanosine (MedChemExpress, USA) and α-adenosine (Santa Cruz Biotechnology, USA).

5.4 Discussion

The experiments in this section were intended to explore nucleoside synthesis from their primary building blocks, nucleobase and ribose. The focus thereby was set on wide ranged screenings to test a multitude of different physical and chemical conditions that could be compatible with a prebiotic Earth, but also with other scenarios along the path to the origin of life. The results should therefore give a rough overview over plausible conditions and serve as base for the constructions of future studies and investigations.

In that sense, the physical conditions investigated were simple dehydration by evaporation and heating at different temperatures, wet-dry cycling in low volumes and the high dynamic evaporation-condensation cycles at air-water interfaces in a thermal gradient. Within those boundaries, the incorporation of geological material (green rust) as studied in alkaline vent settings, higher concentrations of K_2CO_3, as well as different combinations of $MgCl_2$, NH_4Cl and TMP or of exemplary amino acids was tried.

Experimental results within the tested conditions showed overall very low yields and the best cases values around 2-3%, which seems comparable to the results of this kind of reaction from precious literature [96, 108]. Highest overall yields for all of the tested nucleosides, could be observed for wet-dry cycling of the reaction mixtures. While amounts for guanosine were the lowest over all tested conditions and mostly even below the detection limit, the highest yields could be obtained for simple dehydration in the presence of carbonate. While in general, the rapid evaporation-condensation cycling in a temperature gradient did not appear to have ah positive effect on β-nucleoside formation, for guanosine 10-fold higher yields could be achieved compared to similar conditions in slow wet-dry cycling. Presence of green rust, on the other hand suggest slightly higher yields in presence of the mineral, however, all the other nucleosides are either not even detectable (guanosine, adenosine) or form in comparable low yields as the control (uridine). The tested amino acids, valine, lysine and proline, did not seem to have any positive impact on the β-nucleoside synthesis. Co-synthesis of two complementary nucleosides, showed overall very low effect, with a slight tendency to improved yields. Guanosine, however, showed increased yields in the presence of proline as well as in wet-dry cycling together with cytosine.

Amino acids have been shown to have catalytic activity on chemical reactions to form sugars or nucleotides [112, 125]. While Suarez et al. [112] found that primarily glycine had a positive effect on the stereo-chemistry of nucleotide synthesis, the exemplary used valine,

lysine and proline did not show an improved yield of β-nucleosides. However, more experiments would be required here together with a deeper analysis of potentially co-synthesised nucleoside-isomers.

Alkaline vents are a promising location for the origin of life and green rust has likely been formed on an early Earth [56] (see also chapter 3 & 4). Especially iron-ions, have multiple positive effects when it comes to RNA, as they stabilise nucleotides and can replace Mg_2^+ during catalytic RNA functions [126–128]. Samples of green rust minerals, however, could not show a huge impact on nucleoside synthesis in the experiments. This, however, might have multiple reasons and should still be investigated in more detail. Although the minerals were grown in anoxic conditions, the experiment itself could only be conducted under ambient conditions, leading to eventual oxidation of the mineral. Apart form that, it is plausible, that iron complexes form together with the dissolved molecules, which might require more extraction steps prior to analysis. Also, a more prebiotically plausible environment as the laboratory recreation of an alkaline vent could benefit the potential of the mineral, as a dry environment in combination with alkaline vents is rather unlikely.

Dehydrating conditions have been found to improve the thermodynamic favorability of the glycosidic bond formation between ribose an nucleobase [96, 107]. Taking it one step further, the repeated evaporation in combination with intermediate rewetting therefore seems to be a logical connection. Wet-dry cycles are proposed as another plausible location for origin of life processes usually in the environment of warm little ponds and have been shown to improve prebiotic reactions such as polymerisation [104, 105, 129] or nucleotide formation [112]. Screenings of different chemical conditions in 3 wet-dry cycles showed amongst the highest yields of nucleosides overall in the conducted experiments, which can probably be explained by the repeated dehydration after redissolving the dried sample. While most β-nucleosides showed lower yields in the presence of TMP, this could in fact be due to a further progress towards the formation of nuclotides by either phosphorylation of nucleosides or more likely the coupling of before phosphorylated ribose to the nucleobases, a process also shown by [112]. Apart from that, also the formation of the non-canonical nucleoside inosine, could be shown in significant yields ($\geq$1%) and therefore in much higher amount than guanosine under all other conditions. This would support the hypothesis, that inosine could have been a precursor molecule and alternative predecessor to guanosine in the genetic alphabet, as is was also shown to basepair with cytidine [61–63].

Especially as carbonate presence showed a significantly improved yield for guanosine, the combination with phosphate could pose a promising path. Availability of high concentrations of phosphate on early Earth is debated, but carbonate-rich lakes have been shown to be capable of concentrating dissolved phosphate [124]. Thus, they could not only provide the material for the subsequent phosphorylation of nucleoside, but offer also the presence of carbonate.

Pushing the dynamics of wet-dry cycles even further, a rapid cycle of evaporation and condensation can be realised at an air-water interface subjected to a thermal gradient. This system has been shown to facilitate the concentration of dissolved molecules and create periodic wet-dry states [16, 65]. Experiments for nucleoside synthesis, however, showed no further improvement of yields compared to the dry-wet cycling under similar conditions, except for β-guanosine. The latter could even be obtained in roughly 10-fold higher yield, although still rather low amount. Considering the fact, that guanosine was even below detection limit form many of the experiments, further experiments should test this highly dynamic system with addition of carbonate and TMP to test for potential nucleotide formation.

One key problem, in the synthesis of nucleosides from their building blocks, is the lack of regio- and stereo-selectivity of the reaction [108]. This creates not only a high amount of side products during the reaction, diminishing the yields of the target molecules, but also make them difficult to analyse. In the described experiments, the products were identified and quantified by HPLC-MS, based on their chromatographic retention time based on commercial standards as well are their mass. While all different target-nucleosides and their could be well separated (**Figure 5..2**), it could clearly be seen that many molecules co-eluted with identical masses and sometimes only minor shift in retention time. As cytidine was one of the most difficult nucleosides to separate, becoming apparent by is early elution and close proximity to the its α-from, it was also most difficult to identify, amongst many smaller peaks in close proximity with identical mass. Therefore, it needs to be stated, that the amounts of cytidine given in the plots above, might not be full accurate, due to the limitations of the applied analysis methods. Given the surprisingly high yields for β-cytidine overall, this an overlap in retention time with other regio- or stereo-isomers seems plausible, especially as previous literature state that the reaction barely works for pyrimidine nucleobases [63, 96, 108]. For a definitive identification of all nucleoside therefore further analysis methods, such as isotope fragmentation analysis in MS2 measurements or nuclear magnetic resonance (NMR) spectroscopy, will be required.

Another limiting factor in this synthesis pathway, is the stability of ribose. Apart form the fact that prebiotic ribose synthesis is another challenge on its own [108, 130], ribose is also unstable in aqueous solutions and especially under alkaline conditions [108, 131]. While this is one key factor that potentially reduces the yield of actual β-form nucleosides, phosphorylation of ribose prior to condensation with the nucleobase could reduce this problem also shown by the application of D-ribose-5'-phosphate in [112]. A potential phosphorylation of ribose should therefore be investigated and also checked in the experiments using TMP in the reaction mixture. The reduced nucleoside yield in the presence of TMP could be a hint in or either ribose or nucleosides with phosphate. Phosphorylation or ribose would be beneficial, since this could not only provide a route to nucleotide, but also reduce the number of regio-isomers in the reaction.

5.5 Conclusion

Prebiotic synthesis of nucleosides is one of the major hurdles along the path to first ribonucleic-acids and therefore referred to as the "nucleoside problem" [96, 107]. The experiments here were intended to screen many prebiotically plausible conditions, physical and chemical, to get an estimate about potential conditions for future investigations.

Amongst overall low yields, wet-dry cycling showed highest product amounts for all of the four canonical nucleosides as well as the non-canonical inosine. Guanosine was mostly obtained in negligible amounts close to the detection limit. However, highest yields were obtained in a dehydration reaction in the presence of carbonate and also exposure to an air-water interface in a temperature gradient, could improve the yield 10-fold compared to similar conditions in wet-dry cycling. Based on those findings, future experiments should investigate nucleoside synthesis under wet-dry cycling, and the addition of carbonate and phosphate. To boost the wet-dry conditions even further subsequent steps could then enhance the dynamic by integration of the system into temperature gradients.

To draw any conclusion about which conditions might actually boost the formation of β-nucleosides, further investigations are necessary with more detailed analysis of reaction mechanisms and obtained stereo-isomers.

Addendum 5

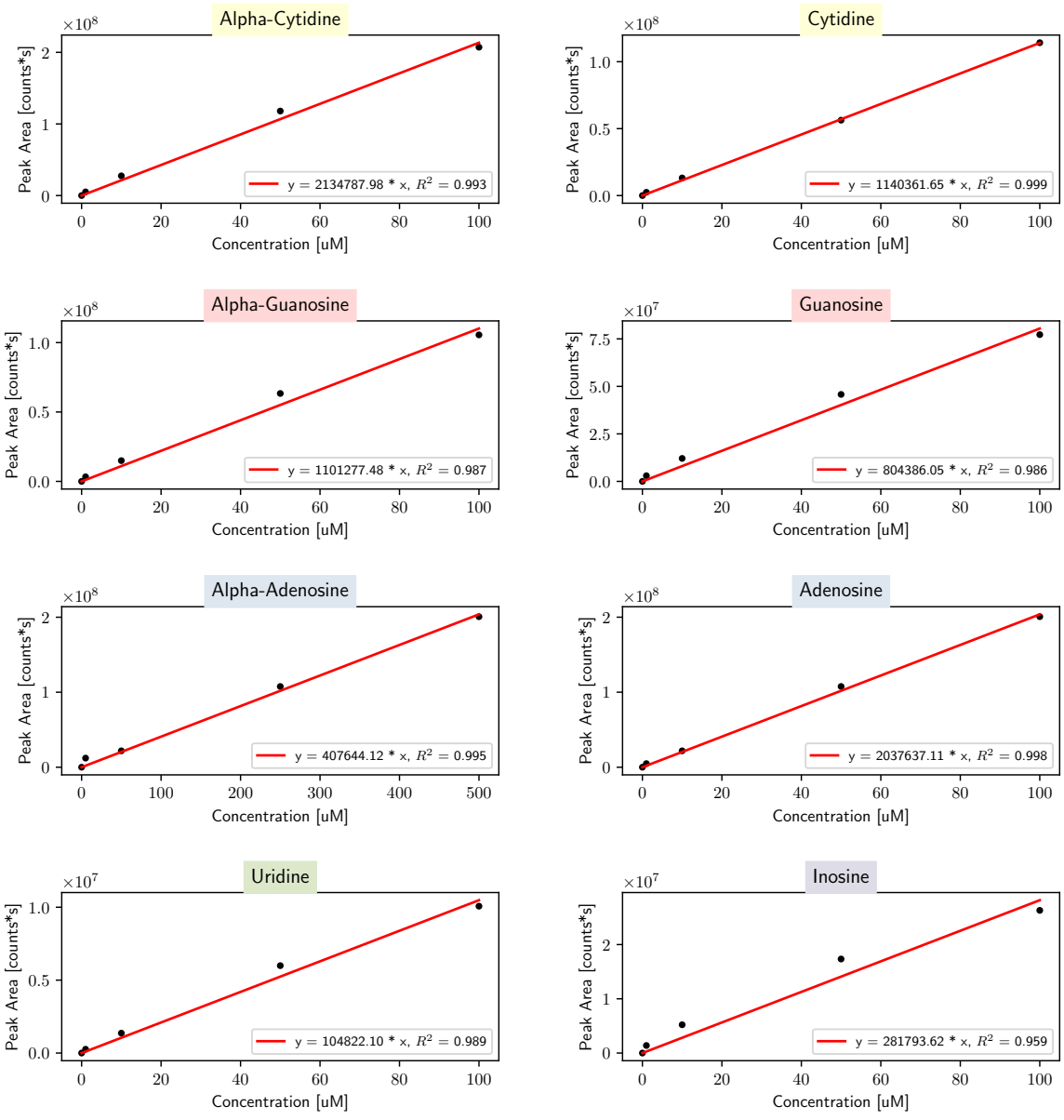

Figure 5..1: Calibration for Orbitrap-MS measurements. The linear regression was obtain from serial dilution of authentic standards for all available nucleosides and used for the quantification and determination of the relative nucleoside-yield in the wet-dry cycling experiments.

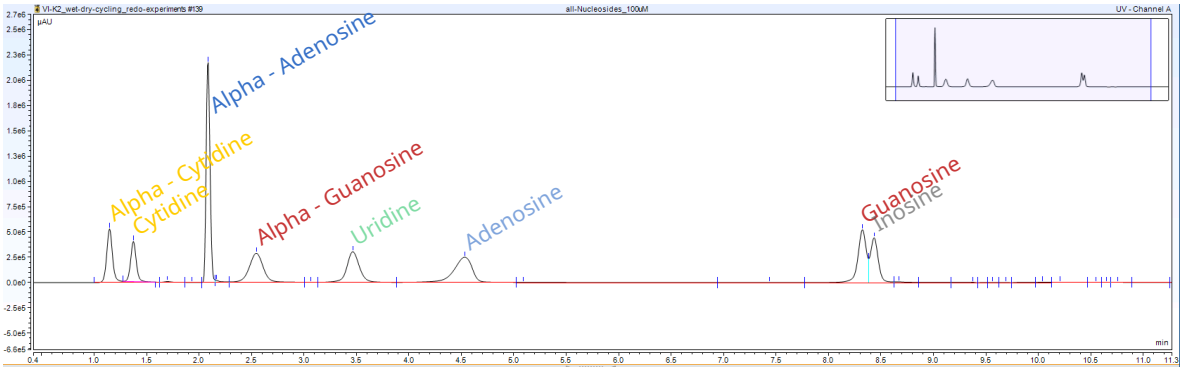

Figure 5..2: Separation of nucleoside-standards and selected anomers by HPLC. The retention times for α-uridine and α-inosine could not bet assessed due to the lack of a commercial standard.

Chapter 6 Conclusion and Outlook

The origin of life on Earth is still a mystery that is not yet solved. While we do not know the exact mechanisms that lead to the transition from non living matter to the first living organisms, the only thing we know for sure, that it did happen in one or the other way. The combination of the knowledge we have about modern life today together with the evidence form earlier aeons of the Earth, we can build hypotheses and try to connect the dots to find plausible paths how it might have happened. One of the key requirements, however, is that any process leading towards life, had to have happened in agreement with the preexisting geological environment on an early Earth. A major implication that comes with that premise, poses that all kinds of molecules needed a way to overcome the high dilutions of the prebiotic oceans. This makes an effective mechanism to concentrate and localise dissolved species a key requirement for potential locations for the origin of life.

Within this thesis, it could be shown that mineral chimneys formed in alkaline vent mimics, have the capability to accumulate dissolved nuclei acids form a solution simulating a prebiotic ocean. The development and application of a microfluidic flow cell, could further show, that the precipitation process known from alkaline vents, can produce various different mineral morphologies when proceeding in quasi-two-dimensional spaces. Depending on the precise parameters, these confined geometries can produce structures allowing the formation and maintenance of micro-scale pH gradients across thin mineral membranes. Accumulation of diapered beads in minerals could also confirm the potential fo alkaline vents to overcome high dilutions. Lastly, the synthesis of nucleosides form their principal building blocks, appeared to work slightly better, when the dynamics of wet-dry cycling are applied, supporting even more the importance of dynamic environments.

While the accumulation of nucleic acids presents already a possible solution to the concentration problem at the origin of life, a next step would now be to check for potential selection pressure within the same environments. At some point, longer polymers of RNA and DNA had to be selected, possible selection in accumulation could therefore foster the survival of long strands or at some point maybe even certain sequences. The microfluidic flow cell could therefore offer more control for the study of accumulation of dispersed molecules or nucleic acids. Its capabilities, providing full optical access, can further be used to study and analyse the formation of different mineral compositions and the structural consequences that the confined geometry could bring. In terms of prebiotic reactions, such a setting could further be used as a flow reactor offering the potential of reactive mineral surfaces along the stream, that could not only promote a reaction but potentially select for emerging products by selective accumulation as well. Nucleoside synthesis benefited form an enhances dynamic in the reaction environment. As already shown for guanosine, this effect could potentially be further improved by the non-equilibrium conditions of thermal gradients. While wet-dry cycles are usually proposed for environments on Earths surface, confined spaces with trapped gas bubbles could existing within the temperature differences in alkaline vent systems. This could make alkaline vents also a plausible location for the emergence of first information storing molecules.

Bibliography

[1] J. William Schopf. Microfossils of the early archean apex chert: New evidence of the antiquity of life. *Science*, 260:640–646, 4 1993.

[2] Matthew S. Dodd, Dominic Papineau, Tor Grenne, John F. Slack, Martin Rittner, Franco Pirajno, Jonathan O'Neil, and Crispin T.S. Little. Evidence for early life in earth's oldest hydrothermal vent precipitates. *Nature 2017 543:7643*, 543:60–64, 3 2017.

[3] S. J. Mojzsis, G. Arrhenius, K. D. McKeegan, T. M. Harrison, A. P. Nutman, and C. R.L. Friend. Evidence for life on earth before 3,800 million years ago. *Nature 1996 384:6604*, 384:55–59, 1996.

[4] W. F. Bottke, D. Vokrouhlický, S. Marchi, T. Swindle, E. R.D. Scott, J. R. Weirich, and H. Levison. Dating the moon-forming impact event with asteroidal meteorites. *Science*, 348:321–323, 4 2015.

[5] R. Brasser, S. C. Werner, and S. J. Mojzsis. Impact bombardment chronology of the terrestrial planets from 4.5ga to 3.5ga. *Icarus*, 338:113514, 3 2020.

[6] Frances Westall, André Brack, Alberto G. Fairén, and Mitchell D. Schulte. Setting the geological scene for the origin of life and continuing open questions about its emergence. *Frontiers in Astronomy and Space Sciences*, 9:1095701, 1 2023.

[7] Stephen J. Mojzsis, T. Mark Harrison, and Robert T. Pidgeon. Oxygen-isotope evidence from ancient zircons for liquid water at the earth's surface 4,300myr ago. *Nature 2001 409:6817*, 409:178–181, 1 2001.

[8] Daniel Whitaker and Matthew W. Powner. Prebiotic nucleic acids need space to grow. *Nature Communications*, 9:5172, 12 2018.

[9] S. Marchi, N. Drabon, T. Schulz, L. Schaefer, D. Nesvorny, W. F. Bottke, C. Koeberl, and T. Lyons. Delayed and variable late archaean atmospheric oxidation due to high collision rates on earth. *Nature Geoscience 2021 14:11*, 14:827–831, 10 2021.

[10] Christian De Duve and Richard De Neufville. *Blueprint for a cell: the nature and origin of life*. Carolina Biological Supply Company, 1991.

[11] Christina F. Dirscherl, Alan Ianeselli, Damla Tetiker, Thomas Matreux, Robbin M. Queener, Christof B. Mast, and Dieter Braun. A heated rock crack captures and polymerizes primordial DNA and RNA. *Physical Chemistry Chemical Physics*, pages 3375–3386, 2023.

[12] Christof B Mast and Dieter Braun. Thermal trap for DNA replication. *Physical review letters*, 104(18):188102, 2010.

[13] Christof B. Mast, Severin Schink, Ulrich Gerland, and Dieter Braun. Escalation of polymerization in a thermal gradient. *Proceedings of the National Academy of Sciences of the United States of America*, 110(20):8030–8035, 2013.

[14] Thomas Matreux, Bernhard Altaner, Johannes Raith, Dieter Braun, Christof B Mast, and Ulrich Gerland. Formation mechanism of thermally controlled ph gradients. *Communications Physics*, 6(1):14, 2023.

[15] Matthias Morasch, Jonathan Liu, Christina F. Dirscherl, Alan Ianeselli, Alexandra Kühnlein, Kristian Le Vay, Philipp Schwintek, Saidul Islam, Mérina K. Corpinot, Bettina Scheu, Donald B. Dingwell, Petra Schwille, Hannes Mutschler, Matthew W. Powner, Christof B. Mast, and Dieter Braun. Heated gas bubbles enrich, crystallize, dry, phosphorylate and encapsulate prebiotic molecules. *Nature Chemistry*, 11:779–788, 2019.

[16] Annalena Salditt, Leonie Karr, Elia Salibi, Kristian Le Vay, Dieter Braun, and Hannes Mutschler. Ribozyme-mediated rna synthesis and replication in a model hadean microenvironment. *Nature Communications 2023 14:1*, 14:1–8, 3 2023.

[17] Emil Agerschou, Christof Mast, and Dieter Braun. Emergence of life from trapped nucleotides? non-equilibrium - behavior of oligonucleotides in thermal gradients. *Synlett*, pages 56–63, 12 2016.

[18] Stephen Ornes. How nonequilibrium thermodynamics speaks to themystery of life. *Proceedings of the National Academy of Sciences of the United States of America*, 114:423–424, 1 2017.

[19] Erwin Schrödinger. *What is life? The physical aspect of the living cell*. Cambridge Univ. Press, repr edition, 1944.

[20] John B. Corliss, Jack Dymond, Louis I. Gordon, John M. Edmond, Richard P. Von Herzen, Robert D. Ballard, Kenneth Green, David Williams, Arnold Bainbridge, Kathy Crane, and Tjeerd H. Van Andel. Submarine thermal springs on the galápagos rift. *Science*, 203:1073, 3 1979.

[21] John A. Baross and Sarah E. Hoffman. Submarine hydrothermal vents and associated gradient environments as sites for the origin and evolution of life. *Origins of Life and Evolution of the Biosphere*, 15:327–345, 12 1985.

[22] William Martin and Michael J. Russell. On the origin of biochemistry at an alkaline hydrothermal vent. *Philosophical Transactions of the Royal Society B: Biological Sciences*, 362(1486):1887–1926, oct 2007.

[23] Laura M. Barge, Erika Flores, Marc M. Baum, David G.Vander Velde, and Michael J. Russell. Redox and pH gradients drive amino acid synthesis in iron oxyhydroxide mineral systems. *Proceedings of the National Academy of Sciences of the United States of America*, 116(11):4828–4833, 2019.

[24] William Martin, John Baross, Deborah Kelley, and Michael J. Russell. Hydrothermal vents and the origin of life. *Nature Reviews Microbiology 2008 6:11*, 6(11):805–814, sep 2008.

[25] M. J. Russell and A. J. Hall. The emergence of life from iron monosulphide bubbles at a submarine hydrothermal redox and pH front. *Journal of the Geological Society*, 154(3):377–402, may 1997.

[26] Victor Sojo, Barry Herschy, Alexandra Whicher, Eloi Camprubí, and Nick Lane. The Origin of Life in Alkaline Hydrothermal Vents. *Astrobiology*, 16(2):181–197, 2016.

[27] Nils G. Holm. Why are Hydrothermal Systems Proposed as Plausible Environments for the Origin of Life? *Marine Hydrothermal Systems and the Origin of Life*, pages 5–14, 1992.

[28] N. H. Sleep, A. Meibom, Th Fridriksson, R. G. Coleman, and D. K. Bird. H2-rich fluids from serpentinization: Geochemical and biotic implications. *Proceedings of the National Academy of Sciences*, 101(35):12818–12823, aug 2004.

[29] Wolfgang Bach, Holger Paulick, Carlos J. Garrido, Benoit Ildefonse, William P. Meurer, and Susan E. Humphris. Unraveling the sequence of serpentinization reactions: petrography, mineral chemistry, and petrophysics of serpentinites from MAR 15°N (ODP Leg 209, Site 1274). *Geophysical Research Letters*, 33(13):13306, jul 2006.

[30] Deborah S. Kelley, Jeffrey A. Karson, Donna K. Blackman, Gretchen L. Früh-Green, David A. Butterfield, Marvin D. Lilley, Eric J. Olson, Matthew O. Schrenk, Kevin K. Roe, Geoff T. Lebon, and Pete Rivizzigno. An off-axis hydrothermal vent field near the Mid-Atlantic Ridge at 30° N. *Nature 2001 412:6843*, 412(6843):145–149, jul 2001.

[31] Friederike M. Möller, Franziska Kriegel, Michael Kieß, Victor Sojo, and Dieter Braun. Steep pH Gradients and Directed Colloid Transport in a Microfluidic Alkaline Hydrothermal Pore. *Angewandte Chemie - International Edition*, 56(9):2340–2344, 2017.

[32] Martina Preiner, Joana C. Xavier, Filipa L. Sousa, Verena Zimorski, Anna Neubeck, Susan Q. Lang, H. Chris Greenwell, Karl Kleinermanns, Harun Tüysüz, Tom M. McCollom, Nils G. Holm, and William F. Martin. Serpentinization: Connecting Geochemistry, Ancient Metabolism and Industrial Hydrogenation. *Life 2018, Vol. 8, Page 41*, 8(4):41, sep 2018.

[33] María Colín-García, Alejandro Heredia, Guadalupe Cordero, Antoni Camprubí, Alicia Negrón-Mendoza, Fernando Ortega-Gutiérrez, Hugo Beraldi, Sergio Ramos-Bernal, María Colín-García, Alejandro Heredia, Guadalupe Cordero, Antoni Camprubí, Alicia Negrón-Mendoza, Fernando Ortega-Gutiérrez, Hugo Beraldi, and Sergio Ramos-Bernal. Hydrothermal vents and prebiotic chemistry: a review. *Boletín de la Sociedad Geológica Mexicana*, 68:599–620, 2016.

[34] Barry Herschy, Alexandra Whicher, Eloi Camprubi, Cameron Watson, Lewis Dartnell, John Ward, Julian R.G. Evans, and Nick Lane. An origin-of-life reactor to simulate alkaline hydrothermal vents. *Journal of Molecular Evolution*, 79(5-6):213–227, nov 2014.

[35] Akira Yamaguchi, Masahiro Yamamoto, Ken Takai, Takumi Ishii, Kazuhito Hashimoto, and Ryuhei Nakamura. Electrochemical CO2 Reduction by Ni-containing Iron Sulfides: How Is CO2 Electrochemically Reduced at Bisulfide-Bearing Deep-sea Hydrothermal Precipitates? *Electrochimica Acta*, 141:311–318, sep 2014.

Bibliography

[36] Everett L. Shock. Geochemical constraints on the origin of organic compounds in hydrothermal systems. *Origins of Life and Evolution of the Biosphere*, 20:331–367, 5 1990.

[37] Norio Kitadai, Ryuhei Nakamura, Masahiro Yamamoto, Ken Takai, Naohiro Yoshida, and Yoshi Oono. Metals likely promoted protometabolism in early ocean alkaline hydrothermal systems. *Science Advances*, 5, 2019.

[38] Walter Gilbert. The rna world. *Nature*, 319:618, 1986.

[39] Michael P. Robertson and Gerald F. Joyce. The origins of the rna world. *Cold Spring Harbor Perspectives in Biology*, 4:a003608, 5 2012.

[40] Martina Preiner, Kensuke Igarashi, Kamila B. Muchowska, Mingquan Yu, Sreejith J. Varma, Karl Kleinermanns, Masaru K. Nobu, Yoichi Kamagata, Harun Tüysüz, Joseph Moran, and William F. Martin. A hydrogen-dependent geochemical analogue of primordial carbon and energy metabolism. *Nature Ecology & Evolution 2020 4:4*, 4(4):534–542, mar 2020.

[41] F. N. Spiess, Ken C. Macdonald, T. Atwater, R. Ballard, A. Carranza, D. Cordoba, C. Cox, V. M. Diaz Garcia, J. Francheteau, J. Guerrero, J. Hawkins, R. Haymon, R. Hessler, T. Juteau, M. Kastner, R. Larson, B. Luyendyk, J. D. Macdougall, S. Miller, W. Normark, J. Orcutt, and C. Rangin. East pacific rise: Hot springs and geophysical experiments. *Science*, 207:1421–1433, 3 1980.

[42] K. L. Von Damm. Controls on the chemistry and temporal variability of seafloor hydrothermal fluids. *Geophysical Monograph Series*, 91:222–247, 1995.

[43] Deborah S. Kelley, Jeffrey A. Karson, Gretchen L. Früh-Green, Dana R. Yoerger, Timothy M. Shank, David A. Butterfield, John M. Hayes, Matthew O. Schrenk, Eric J. Olson, Giora Proskurowski, Mike Jakuba, Al Bradley, Ben Larson, Kristin Ludwig, Deborah Glickson, Kate Buckman, Alexander S. Bradley, William J. Brazelton, Kevin Roe, Mitch J. Elend, Adélie Delacour, Stefano M. Bernasconi, Marvin D. Lilley, John A. Baross, Roger E. Summons, and Sean P. Sylva. A serpentinite-hosted ecosystem: The Lost City hydrothermal field. *Science*, 307(5714):1428–1434, mar 2005.

[44] Wolfgang Bach, Neil R. Banerjee, Henry J. B. Dick, and Edward T. Baker. Discovery of ancient and active hydrothermal systems along the ultra-slow spreading southwest indian ridge 10°–16°e. *Geochemistry, Geophysics, Geosystems*, 3:1–14, 7 2002.

[45] Vanessa Helmbrecht, Maximilian Weingart, Frieder Klein, Dieter Braun, and William D Orsi. White and green rust chimneys accumulate rna in a ferruginous chemical garden. *Geobiology*, 21(6):758–769, 2023.

[46] Joti Rouillard, J-M García-Ruiz, J Gong, and Mark A Van Zuilen. A morphogram for silica-witherite biomorphs and its application to microfossil identification in the early earth rock record. *Geobiology*, 16(3):279–296, 2018.

[47] Lauren M. White, Rohit Bhartia, Galen D. Stucky, Isik Kanik, and Michael J. Russell. Mackinawite and greigite in ancient alkaline hydrothermal chimneys: Identifying potential key catalysts for emergent life. *Earth and Planetary Science Letters*, 430:105–114, nov 2015.

[48] E. G. Nisbet. The Geological Setting of the Earliest Life Forms. *Journal of Molecular Evolution*, 21:289–298, 1985.

[49] James F. Kasting. Earth's early atmosphere. *Science*, 259:920–926, 2 1993.

[50] James C.G. Walker. Carbon dioxide on the early earth. *Origins of Life and Evolution of the Biosphere*, 16:117–127, 6 1985.

[51] M. J. Russell, A. J. Hall, and W. Martin. Serpentinization as a source of energy at the origin of life. *Geobiology*, 8(5):355–371, dec 2010.

[52] Simon W. Poulton and Donald E. Canfeld. Ferruginous Conditions: A Dominant Feature of the Ocean through Earth's History. *Elements*, 7(2):107–112, apr 2011.

[53] Gordon Macleod, Christopher McKeown, Allan J. Hall, and Michael J. Russell. Hydrothermal and oceanic pH conditions of possible relevance to the origin of life. *Origins of Life and Evolution of the Biosphere*, 24(1):19–41, feb 1994.

[54] I. Halevy and A. Bachan. The geologic history of seawater pH. *Science*, 355(6329):1069–1071, mar 2017.

[55] Elizabeth D. Swanner, Nicholas Lambrecht, Chad Wittkop, Chris Harding, Sergei Katsev, Joshua Torgeson, and Simon W. Poulton. The biogeochemistry of ferruginous lakes and past ferruginous oceans. *Earth-Science Reviews*, 211:103430, dec 2020.

[56] Michael J. Russell. Green Rust: The Simple Organizing 'Seed' of All Life? *Life 2018, Vol. 8, Page 35*, 8(3):35, aug 2018.

[57] Fabienne Trolard, Simon Duval, Wolfgang Nitschke, Bénédicte Ménez, Céline Pisapia, Jihaine Ben Nacib, Muriel Andréani, and Guilhem Bourrié. Mineralogy, geochemistry and occurrences of fougerite in a modern hydrothermal system and its implications for the origin of life. *Earth-Science Reviews*, 225:103910, 2022.

[58] Laura M. Barge, Silvana S.S. Cardoso, Julyan H.E. Cartwright, Geoffrey J.T. Cooper, Leroy Cronin, Anne De Wit, Ivria J. Doloboff, Bruno Escribano, Raymond E. Goldstein, Florence Haudin, David E.H. Jones, Alan L. Mackay, Jerzy Maselko, Jason J. Pagano, J. Pantaleone, Michael J. Russell, C. Ignacio Sainz-Díaz, Oliver Steinbock, David A. Stone, Yoshifumi Tanimoto, and Noreen L. Thomas. From Chemical Gardens to Chemobrionics. *Chemical Reviews*, 115(16):8652–8703, 2015.

[59] Thiago Altair, Luiz G.F. Borges, Douglas Galante, and Hamilton Varela. Experimental Approaches for Testing the Hypothesis of the Emergence of Life at Submarine Alkaline Vents. *Life 2021, Vol. 11, Page 777*, 11(8):777, jul 2021.

[60] Maximilian Weingart, Siyu Chen, Clara Donat, Vanessa Helmbrecht, William D. Orsi, Dieter Braun, and Karen Alim. Alkaline vents recreated in two dimensions to study ph gradients, precipitation morphology, and molecule accumulation. *Science Advances*, 9, 9 2023.

[61] Mahipal Yadav, Ravi Kumar, and Ramanarayanan Krishnamurthy. Chemistry of abiotic nucleotide synthesis. *Chemical Reviews*, 120:4766–4805, 6 2020.

[62] Seohyun Chris Kim, Derek K. O'Flaherty, Lijun Zhou, Victor S. Lelyveld, and Jack W. Szostak. Inosine, but none of the 8-oxo-purines, is a plausible component of a primordial version of rna. *Proceedings of the National Academy of Sciences of the United States of America*, 115:13318–13323, 12 2018.

[63] William D. Fuller, Robert A. Sanchez, and Leslie E. Orgel. Studies in prebiotic synthesis. vi. synthesis of purine nucleosides. *Journal of Molecular Biology*, 67:25–33, 6 1972.

[64] Suin Shim. Diffusiophoresis, diffusioosmosis, and microfluidics: Surface-flow-driven phenomena in the presence of flow. *Chemical Reviews*, 122:6986–7009, 4 2022.

[65] Alan Ianeselli, Miguel Atienza, Patrick W. Kudella, Ulrich Gerland, Christof B. Mast, and Dieter Braun. Water cycles in a hadean co2 atmosphere drive the evolution of long dna. *Nature Physics 2022 18:5*, 18:579–585, 3 2022.

[66] R. Savino, D. Paterna, and N. Favaloro. Buoyancy and marangoni effects in an evaporating drop. *https://doi.org/10.2514/2.6716*, 16:562–574, 5 2012.

[67] Stefan Duhr and Dieter Braun. Why molecules move along a temperature gradient. *Proceedings of the National Academy of Sciences of the United States of America*, 103(52):19678–19682, 2006.

[68] Laura M. Barge, Yeghegis Abedian, Ivria J. Doloboff, Jessica E. Nuñez, Michael J. Russell, Richard D. Kidd, and Isik Kanik. Chemical gardens as flow-through reactors simulating natural hydrothermal systems. *Journal of Visualized Experiments*, 2015(105), nov 2015.

[69] Qingpu Wang, Keeley S. Hernesman, and Oliver Steinbock. Flow-Driven Precipitation Patterns with Microemulsions in a Confined Geometry. *ChemSystemsChem*, 2(2):e1900037, apr 2020.

[70] Lorenz Keil, Michael Hartmann, Simon Lanzmich, and Dieter Braun. Probing of molecular replication and accumulation in shallow heat gradients through numerical simulations. *Physical Chemistry Chemical Physics*, 18(30):20153–20159, jul 2016.

[71] Ulysse Pedreira-Segade, Cécile Feuillie, Manuel Pelletier, Laurent J. Michot, and Isabelle Daniel. Adsorption of nucleotides onto ferromagnesian phyllosilicates: Significance for the origin of life. *Geochimica et Cosmochimica Acta*, 176:81–95, mar 2016.

[72] Avinash Vicholous Dass, Sreekar Wunnava, Juliette Langlais, Beatriz von der Esch, Maik Krusche, Lennard Ufer, Nico Chrisam, Romeo C. A. Dubini, Florian Gartner, Severin Angerpointner, Christina F. Dirscherl, Petra Rovó, Christof B. Mast, Judit E. Šponer, Christian Ochsenfeld, Erwin Frey, and Dieter Braun. RNA Oligomerisation without Added Catalyst from 2',3'-Cyclic Nucleotides by Drying at Air-Water Interfaces**. *ChemSystemsChem*, 5(1), jan 2023.

[73] Victor Sojo, Aya Ohno, Shawn E. McGlynn, Yoichi M.A. Yamada, and Ryuhei Nakamura. Microfluidic reactors for carbon fixation under ambient-pressure alkaline-hydrothermal-vent conditions. *Life*, 9(1), 2019.

Bibliography

[74] Bradley T. Burcar, Laura M. Barge, Dustin Trail, E. Bruce Watson, Michael J. Russell, and Linda B. McGown. RNA Oligomerization in Laboratory Analogues of Alkaline Hydrothermal Vent Systems. *Astrobiology*, 15(7):509–522, jul 2015.

[75] Julyan H.E. Cartwright, Juan Manuel García-Ruiz, María Luisa Novella, and Fermín Otálora. Formation of Chemical Gardens. *Journal of Colloid and Interface Science*, 256(2):351–359, dec 2002.

[76] Stéphane Leduc. *The Mechanism of Life*. Rebman, London, 1911.

[77] Florence Haudin, Julyan H.E. Cartwright, Fabian Brau, and A. De Wit. Spiral precipitation patterns in confined chemical gardens. *Proceedings of the National Academy of Sciences of the United States of America*, 111(49):17363–17367, dec 2014.

[78] Gábor Schuszter, Fabian Brau, and A. De Wit. Flow-driven control of calcium carbonate precipitation patterns in a confined geometry. *Physical Chemistry Chemical Physics*, 18(36):25592–25600, sep 2016.

[79] Luis A.M. Rocha, Lewis Thorne, Jasper J. Wong, Julyan H.E. Cartwright, and Silvana S.S. Cardoso. Archimedean Spirals Form at Low Flow Rates in Confined Chemical Gardens. *Langmuir*, 38(21):6700–6710, may 2022.

[80] David A. Stone, Braddon Lewellyn, James C. Baygents, and Raymond E. Goldstein. Precipitative growth templated by a fluid jet. *Langmuir*, 21(24):10916–10919, nov 2005.

[81] Edina Balog, Paszkál Papp, Ágota Tóth, Dezső Horváth, and Gábor Schuszter. The impact of reaction rate on the formation of flow-driven confined precipitate patterns. *Physical Chemistry Chemical Physics*, 22(24):13390–13397, jun 2020.

[82] C. Ignacio Sainz-Díaz, Elizabeth Escamilla-Roa, and Julyan H.E. Cartwright. Growth of Self-Assembling Tubular Structures of Magnesium Oxy/Hydroxide and Silicate Related With Seafloor Hydrothermal Systems Driven by Serpentinization. *Geochemistry, Geophysics, Geosystems*, 19(8):2813–2822, aug 2018.

[83] Yang Ding, Carlos M. Gutiérrez-Ariza, Mingchuan Zheng, Amy Felgate, Anna Lawes, C. Ignacio Sainz-Díaz, Julyan H.E. Cartwright, and Silvana S.S. Cardoso. Downward fingering accompanies upward tube growth in a chemical garden grown in a vertical confined geometry. *Physical Chemistry Chemical Physics*, 24(29):17841–17851, jul 2022.

[84] Reuben Hudson, Ruvan de Graaf, Mari Strandoo Rodin, Aya Ohno, Nick Lane, Shawn E. McGlynn, Yoichi M.A. Yamada, Ryuhei Nakamura, Laura M. Barge, Dieter Braun, and Victor Sojo. CO2 reduction driven by a pH gradient. *Proceedings of the National Academy of Sciences of the United States of America*, 117(37):22873–22879, sep 2020.

[85] Qingpu Wang, Laura M. Barge, and Oliver Steinbock. Microfluidic Production of Pyrophosphate Catalyzed by Mineral Membranes with Steep pH Gradients. *Chemistry - A European Journal*, 25(18):4732–4739, 2019.

[86] Bruno C. Batista and Oliver Steinbock. Growing inorganic membranes in microfluidic devices: chemical gardens reduced to linear walls. *Journal of Physical Chemistry C*, 119(48):27045–27052, 2015.

[87] Qingpu Wang and Oliver Steinbock. Materials Synthesis and Catalysis in Microfluidic Devices: Prebiotic Chemistry in Mineral Membranes. *ChemCatChem*, 12(1):63–74, 2020.

[88] Vincent P. Aguirre, Simonne Jocic, Paul Webster, Christopher Buser, John A. Moss, Laura M. Barge, Yijie Tang, Yisong Guo, and Marc M. Baum. Synthesis and characterization of mixed-valent iron layered double hydroxides ("green rust"). *ACS Earth and Space Chemistry*, 5:40–54, 2021.

[89] Tuğçe Beyazay, Kendra S. Belthle, Christophe Farès, Martina Preiner, Joseph Moran, William F. Martin, and Harun Tüysüz. Ambient temperature CO2 fixation to pyruvate and subsequently to citramalate over iron and nickel nanoparticles. *Nature Communications 2023 14:1*, 14(1):1–11, feb 2023.

[90] Tuğçe Beyazay, Cristina Ochoa-Hernández, Youngdong Song, Kendra S. Belthle, William F. Martin, and Harun Tüysüz. Influence of Composition of Nickel-Iron Nanoparticles for Abiotic CO2 Conversion to Early Prebiotic Organics. *Angewandte Chemie International Edition*, 62(22):e202218189, may 2023.

[91] Katalin Viktória Bere, Emilie Nez, Edina Balog, László Janovák, Dániel Sebők, Ákos Kukovecz, Clément Roux, Veronique Pimienta, and Gábor Schuszter. Enhancing the yield of calcium carbonate precipitation by obstacles in laminar flow in a confined geometry. *Physical Chemistry Chemical Physics*, 23(29):15515–15521, jul 2021.

[92] Alessandro Comolli, A De Wit, and Fabian Brau. Dynamics of $A + B \rightarrow C$ reaction fronts under radial advection in a Poiseuille flow. *PHYSICAL REVIEW E*, 104:44206, 2021.

[93] M. Usman, J. M. Byrne, A. Chaudhary, S. Orsetti, K. Hanna, C. Ruby, A. Kappler, and S. B. Haderlein. Magnetite and green rust: Synthesis, properties, and environmental applications of mixed-valent iron minerals. *Chemical Reviews*, 118:3251–3304, 2018.

[94] Norman H. Sleep, Kevin J. Zahnle, and Roxana E. Lupu. Terrestrial aftermath of the moon-forming impact. *Philosophical Transactions of the Royal Society A: Mathematical, Physical and Engineering Sciences*, 372, 9 2014.

[95] Kevin J. Zahnle, Roxana Lupu, Anthony Dobrovolskis, and Norman H. Sleep. The tethered moon. *Earth and Planetary Science Letters*, 427:74–82, 10 2015.

[96] Orgel Leslie E. Prebiotic chemistry and the origin of the rna world. *Critical Reviews in Biochemistry and Molecular Biology*, 39:99–123, 1 2004.

[97] William Martin, Michael J. Russell, D. Horner, R. Blankenship, T. Cavalier-Smith, and E. Nisbet. On the origins of cells: a hypothesis for the evolutionary transitions from abiotic geochemistry to chemoautotrophic prokaryotes, and from prokaryotes to nucleated cells. *Philosophical Transactions of the Royal Society of London. Series B: Biological Sciences*, 358:59–85, 1 2003.

[98] Elisa Biondi, Yoshihiro Furukawa, Jun Kawai, and Steven A. Benner. Adsorption of rna on mineral surfaces and mineral precipitates. *Beilstein Journal of Organic Chemistry 13:42*, 13:393–404, 3 2017.

[99] Ryo Mizuuchi, Alex Blokhuis, Lena Vincent, Philippe Nghe, Niles Lehman, and David Baum. Mineral surfaces select for longer rna molecules. *Chemical Communications*, 55:2090–2093, 2019.

[100] Ömer K Coskun, Volkan Özen, Scott D Wankel, and William D Orsi. Quantifying population-specific growth in benthic bacterial communities under low oxygen using h 2 18 o. *The ISME Journal*, 13:1546–1559, 2019.

[101] William D. Orsi, Susanne Wilken, Javier del Campo, Thierry Heger, Erick James, Thomas A. Richards, Patrick J. Keeling, Alexandra Z. Worden, and Alyson E. Santoro. Identifying protist consumers of photosynthetic picoeukaryotes in the surface ocean using stable isotope probing. *Environmental Microbiology*, 20:815–827, 2 2018.

[102] James S. Beard, B. Ronald Frost, Patricia Fryer, Andrew McCaig, Roger Searle, Benoit Ildefonse, Pavel Zinin, and Shiv K. Sharma. Onset and Progression of Serpentinization and Magnetite Formation in Olivine-rich Troctolite from IODP Hole U1309D. *Journal of Petrology*, 50(3):387–403, mar 2009.

[103] H. James Cleaves, Ellen Crapster-Pregont, Caroline M. Jonsson, Christopher L. Jonsson, Dimitri A. Sverjensky, and Robert A. Hazen. The adsorption of short single-stranded dna oligomers to mineral surfaces. *Chemosphere*, 83:1560–1567, 2011.

[104] Bruce Damer and David Deamer. The hot spring hypothesis for an origin of life. *Astrobiology*, 20:429–452, 4 2020.

[105] Ben K.D. Pearce, Ralph E. Pudritz, Dmitry A. Semenov, and Thomas K. Henning. Origin of the rna world: The fate of nucleobases in warm little ponds. *Proceedings of the National Academy of Sciences of the United States of America*, 114:11327–11332, 10 2017.

[106] Geoffrey Zubay and Timothy Mui. Prebiotic synthesis of nucleotides. *Origins of life and evolution of the biosphere : the journal of the International Society for the Study of the Origin of Life*, 31:87–102, 2001.

[107] J P Colins and Nicholas V. Hud. Prebiotic synthesis of pyrimidine nucleosides. *School of Chemistry and Biochemistry*, 2005.

[108] Annabelle Biscans. Exploring the emergence of rna nucleosides and nucleotides on the early earth. *Life*, 8, 2018.

[109] Thomas R Cech, Arthur J Zaug, and Paula J Grabowski. In vitro splicing of the ribosomal rna precursor of tetrahymena: Involvement of a guanosine nucleotide in the excision of the intervening sequence. *Cell*, 27:487–496, 1981.

[110] Sidney Altman. Aspects of biochemical catalysis. *Cell*, 36:237–239, 2 1984.

[111] W. D. Fuller, R. A. Sanchez, and L. E. Orgel. Studies in prebiotic synthesis. vii. *Journal of Molecular Evolution*, 1:249–257, 9 1972.

[112] Irene Suárez-Marina, Yousef M. Abul-Haija, Rebecca Turk-MacLeod, Piotr S. Gromski, Geoffrey J. T. Cooper, Andrea Olivé Olivé, Stephanie Colón-Santos, and Leroy Cronin. Author correction: Integrated synthesis of nucleotide and nucleosides influenced by amino acids. *Communications Chemistry*, 2:1–8, 2019.

Bibliography

[113] J. Oró. Synthesis of adenine from ammonium cyanide. *Biochemical and Biophysical Research Communications*, 2:407–412, 1960.

[114] Ben K.D. Pearce and Ralph E. Pudritz. Seeding the pregenetic earth: Meteoritic abundances of nucleobases and potential reaction pathways. *The Astrophysical Journal*, 807:85, 7 2015.

[115] Michael P. Callahan, Karen E. Smith, H. James Cleaves, Josef Ruzicka, Jennifer C. Stern, Daniel P. Glavin, Christopher H. House, and Jason P. Dworkin. Carbonaceous meteorites contain a wide range of extraterrestrial nucleobases. *Proceedings of the National Academy of Sciences of the United States of America*, 108:13995–13998, 8 2011.

[116] Martin A.A. Schoonen and Yong Xu. Nitrogen reduction under hydrothermal vent conditions: Implications for the prebiotic synthesis of c-h-o-n compounds. *https://home.liebertpub.com/ast*, 1:133–142, 7 2004.

[117] Matthew W Powner, Béatrice Gerland, and John D Sutherland. Synthesis of activated pyrimidine ribonucleotides in prebiotically plausible conditions. *Nature*, 459:239–242, 2009.

[118] Matthew W. Powner, John D. Sutherland, and Jack W. Szostak. Chemoselective multicomponent one-pot assembly of purine precursors in water. *Journal of the American Chemical Society*, 132:16677–16688, 11 2010.

[119] R. Sanchez, J. Ferris, and L. E. Orgel. Conditions for purine synthesis: Did prebiotic synthesis occur at low temperatures? *Science*, 153:72–73, 7 1966.

[120] Sidney Becker, Ines Thoma, Amrei Deutsch, Tim Gehrke, Peter Mayer, Hendrik Zipse, and Thomas Carell. A high-yielding, strictly regioselective prebiotic purine nucleoside formation pathway. *Science (New York, N.Y.)*, 352:833–836, 5 2016.

[121] Sidney Becker, Ines Thoma, Amrei Deutsch, Tim Gehrke, Peter Mayer, Hendrik Zipse, and Thomas Carell. Origin of life: A high-yielding, strictly regioselective prebiotic purine nucleoside formation pathway. *Science*, 352:833–836, 5 2016.

[122] John D. Sutherland. Ribonucleotides. *Cold Spring Harbor Perspectives in Biology*, 2:a005439, 4 2010.

[123] Michele Fiore and Peter Strazewski. Bringing prebiotic nucleosides and nucleotides down to earth. *Angewandte Chemie - International Edition*, 55:13930–13933, 11 2016.

[124] Jonathan D. Toner and David C. Catling. A carbonate-rich lake solution to the phosphate problem of the origin of life. *Proceedings of the National Academy of Sciences of the United States of America*, 117:883–888, 1 2020.

[125] Sandra Pizzarello and Arthur L. Weber. Prebiotic amino acids as asymmetric catalysts. *Science*, 303:1151, 2 2004.

[126] Shreyas S. Athavale, Anton S. Petrov, Chiaolong Hsiao, Derrick Watkins, Caitlin D. Prickett, J. Jared Gossett, Lively Lie, Jessica C. Bowman, Eric O'Neill, Chad R. Bernier, Nicholas V. Hud, Roger M. Wartell, Stephen C. Harvey, and Loren Dean Williams. Rna folding and catalysis mediated by iron (ii). *PloS one*, 7, 5 2012.

[127] Marcus S. Bray, Timothy K. Lenz, Jay William Haynes, Jessica C. Bowman, Anton S. Petrov, Amit R. Reddi, Nicholas V. Hud, Loren Dean Williams, and Jennifer B. Glass. Multiple prebiotic metals mediate translation. *Proceedings of the National Academy of Sciences of the United States of America*, 115:12164–12169, 11 2018.

[128] Jessica C Bowman, Timothy K Lenz, Nicholas V Hud, Loren Dean Williams, Jamie Williamson, and Jody Puglisi. Author's personal copy cations in charge: magnesium ions in rna folding and catalysis this review comes from a themed issue on nucleic acids edited by. *Current Opinion in Structural Biology*, 22:262–272, 2012.

[129] Ivar Svalheim Haugerud, Pranay Jaiswal, and Christoph A. Weber. Nonequilibrium wet-dry cycling acts as a catalyst for chemical reactions. *Journal of Physical Chemistry B*, 128:1724–1736, 2 2024.

[130] Robert Shapiro. Prebiotic ribose synthesis: A critical analysis. *Origins of Life and Evolution of the Biosphere*, 18:71–85, 3 1988.

[131] R Larralde, M P Robertson, and S L Miller. Rates of decomposition of ribose and other sugars: implications for chemical evolution. *Proceedings of the National Academy of Sciences*, 92:8158–8160, 8 1995.

List of Figures

List of Tables

List of Publications

In the following all publications during the course of this PhD are listed along the associated first author publications.

First Author Publications

Maximilian Weingart, Siyu Chen, Clara Donat, Vanessa Helmbrecht, William D. Orsi, Dieter Braun, Karen Alim. Alkaline vents recreated in two dimensions to study pH gradients, precipitation morphology, and molecule accumulation.
Science Advances (**2023**) doi.org/10.1126/sciadv.adi1884

Contributed Publications

Vanessa Helmbrecht, **Maximilian Weingart**, Frieder Klein, Dieter Braun, William D. Orsi. White and green rust chimneys accumulate RNA in a ferruginous chemical garden.
Geobiology (**2023**) doi.org/10.1111/gbi.12572

GEOPHYSICS

Alkaline vents recreated in two dimensions to study pH gradients, precipitation morphology, and molecule accumulation

Maximilian Weingart[1], Siyu Chen[2], Clara Donat[3], Vanessa Helmbrecht[4], William D. Orsi[4,5], Dieter Braun[1], Karen Alim[3,2]*

Alkaline vents (AVs) are hypothesized to have been a setting for the emergence of life, by creating strong gradients across inorganic membranes within chimney structures. In the past, three-dimensional chimney structures were formed under laboratory conditions; however, no in situ visualization or testing of the gradients was possible. We develop a quasi–two-dimensional microfluidic model of AVs that allows spatiotemporal visualization of mineral precipitation in low-volume experiments. Upon injection of an alkaline fluid into an acidic, iron-rich solution, we observe a diverse set of precipitation morphologies, mainly controlled by flow rate and ion concentration. Using microscope imaging and pH-dependent dyes, we show that finger-like precipitates can facilitate formation and maintenance of microscale pH gradients and accumulation of dispersed particles in confined geometries. Our findings establish a model to investigate the potential of gradients across a semipermeable boundary for early compartmentalization, accumulation, and chemical reactions at the origins of life.

INTRODUCTION

Investigating the origins of life necessarily leads to the question of which possible locations could have provided promising conditions for the emergence of living systems on a prebiotic Earth. One of the theories today focuses on alkaline vents (AVs) as a promising setting, providing unique chemical and geophysical conditions (*1*–*4*). AVs on the prebiotic seafloor are predicted to have formed chimney structures, where warm alkaline fluids were exhaled into an acidic ocean enriched in dissolved iron(II) (*5*, *6*). Upon contact of the fluids, highly reactive Fe(Ni)S minerals precipitate and enclose the alkaline fluid stream to form a tubular network that grows into chimney-like structures (*3*, *7*). The precipitate thereby acts as a permeable mineral membrane (*8*–*10*) that allows for the generation of steep gradients in pH, redox potential, and temperature, thus providing not only the nonequilibria that might have been crucial for the emergence of life (*11*–*13*) but also a potential energy source for early life forms (*2*, *9*). The mineral surfaces, at the same time, could serve as a catalytic site for abiotic organic synthesis reactions (*7*, *14*), while the inflowing water would provide a constant source of chemical nourishment (*2*). As shown in recent work (*15*), vent minerals could have also facilitated the localization and accumulation of dissolved RNA molecules. The physical nonequilibrium conditions provided by temperature gradients between the fluids can further boost accumulation of dissolved species and increase their local concentration manifold (*16*, *17*). The combination of those characteristics makes AVs also a very interesting location for inorganic catalytic reactions, polymerization or replication (*11*, *18*–*20*). On the other hand, the gradients in pH, separated by a semipermeable membrane, could have worked as an electrochemical reactor, providing a precursor setting for modern autotrophic cells (*1*–*3*, *8*, *21*), although recent publications showed only low yields of simple organic products (*21*–*23*). Which of the conditions provided by AVs, however, are critical or sufficient to drive molecular evolution at the origins of life is mostly unknown.

A well-studied example of AVs formed at moderate temperatures is the Lost City hydrothermal field near the mid-Atlantic spreading centers (*24*, *25*). In general, these vents emerge when ocean water percolates into cracks and fractures of Earth's upper mantle, which typically comprises minerals of ultramafic rock. Upon contact with water, a metamorphic chemical reaction (serpentinization) converts the ultramafic rock to serpentinite (*14*, *26*). The serpentinization-dominated system vents alkaline fluids at ambient temperatures, coprecipitating mainly calcium carbonates and brucite upon mixing with seawater (*24*). However, compared to modern oceans, prebiotic oceans of the Hadean and Archean were likely more acidic (*1*, *27*, *28*), due to saturation with CO_2 from the atmosphere (*8*) and ferruginous, i.e., anoxic conditions with high concentrations of dissolved iron (*5*, *8*, *29*). The acidity of prebiotic seawater (*1*) probably prevented the crystallization of acid-soluble minerals, like the characteristic minerals of Lost City (*25*). Therefore, Lost City–type chimneys were most certainly not present on early Earth; however, serpentinization and the overall mechanism were likely prevalent, particularly since ultramafic intrusions could have been more frequent (*6*), probably even more abundant. Experimental recreations of Hadean ocean chemistry and AVs have demonstrated the capacity for iron oxide and iron sulfide minerals in AV chimneys to accumulate nucleic acids including RNA (*30*). Notably, highly reactive surfaces of ferromagnesian phyllosilicates, especially at AVs, were found to concentrate nucleic acids or nucleotides by adsorption, which could save them from dilution in the prebiotic ocean (*31*). Moreover, "white and green rust"

[1]Systems Biophysics and Center for NanoScience (CeNS), Ludwig-Maximilians University Munich, Amalienstraße 54, 80799 München, Germany. [2]Max Planck Institute for Dynamics and Self-Organization, Am Faßberg 17, 37077 Göttingen, Germany. [3]TUM School of Natural Sciences, Department of Bioscience; Center for Protein Assemblies (CPA), Technical University of Munich, Ernst-Otto-Fischer-Str. 8, 85748 Garching b. München, Germany. [4]Department of Earth and Environmental Sciences, Ludwig-Maximilians University Munich, Richard-Wagner Straße 10, 80333 München, Germany. [5]GeoBio-CenterLMU, Ludwig-Maximilians University Munich, Richard-Wagner Straße 10, 80333 München, Germany.
*Corresponding author. Email: k.alim@tum.de

(amakinite and fourgerite) ferrous-ferric oxyhydroxide minerals that precipitate during the growth of chimneys in AVs under ferruginous conditions have been found to concentrate RNA within the chimney structure from surrounding ferruginous solution (*15*). This experimental results reflect the naturally occurring mineralogy of AV systems, where amakinite or "white rust" (the rare ferrous analog of brucite) was detected in the basement rocks below the Lost City hydrothermal field (*32*, *33*). In addition to iron oxyhydroxides, iron sulfide minerals also promote the RNA complexation concentration within AV hydrothermal chimney structures (*34*). NASA undertook several studies to recreate the conditions of prebiotic AVs in the laboratory but has so far only investigated the structures in three dimensions (*13*, *23*, *35*, *36*).

Controlled precipitation reactions have a long history, reaching back to early alchemists, and are now comprised in the field of chemobrionics (*37*). The resulting structures, often referred to as chemical gardens, can be seen as a simple example of self-organizing systems that exhibit all kinds of different morphologies under different chemical and physical conditions (*37*, *38*). Apart from precipitation and crystallization, structure growth is driven by fluid advection through either active injection (*39*–*42*) or osmosis and convection (*43*, *44*). In the past years, they have also been increasingly studied in quasi–two-dimensional (2D) settings using microfluidic devices like Hele-Shaw flow cells (*10*, *40*, *45*, *46*). The focus is not only mostly on reaction parameters that allow ordered structures like hollow cylinders but also on mathematical modeling of the resulting patterns (*39*, *46*, *47*). Because of their apparent similarity to living organisms (*37*), there was huge interest in chemical garden structures in the early stages of the origins of life field (*38*, *48*), but had been neglected since, until NASA researchers started to recreate hydrothermal vent analogs in the laboratory (*23*, *35*). However, so far, none of the chemical garden studies in confined geometries has attempted to recreate the conditions of the origins of life on Earth.

In our experiments, we use a thin, translucent microfluidic cell built up by a cutout from a Teflon sheet that is sandwiched between two sapphire slides and located horizontally on the stage of a microscope. The rectangular chamber is filled with an acidic iron solution to simulate the ocean, and a sodium hydroxide solution injected by a syringe pump simulates the venting of alkaline fluid (see Fig. 1). This setup of the flow cell allows for microscope imaging in bright-field and dark-field mode. Although the thin mineral membranes formed in hydrothermal vents have been studied in microfluidics before (*9*, *21*, *49*–*51*), only controlled single membranes were created by laminar coflow of the fluids. Our experiments, here, are designed to provide a 2D representation of the 3D physiology of AVs, where acidic and alkaline fluids come into contact.

Here, we show that our setup enables us to visualize the formation of pH gradients in a quasi-2D model of alkaline vents to study the effects of physical parameters like flow rate and fluid concentration on resulting morphologies and emerging gradients. Our results show that finger-like precipitation patterns at mediate flow and concentration facilitate the formation of pH gradients while at the same time allowing for the accumulation of dispersed particles on the reactive mineral surfaces. The confined microfluidic chamber can therefore be seen not only as a model for the geological analog but also as a simulation of potential mixing of the fluids that could already start in the cracks and fractures of the seafloor even before the alkaline fluid is vented into the ocean. Our setup therefore provides a way to simulate chemicophysical hydrothermal vent experiments in the laboratory in low volume.

RESULTS

To mimic mineral precipitation in hydrothermal vents, we used a custom-built microfluidic flow cell to inject alkaline fluids into acidic ocean water (fig. S1). This, on the one hand, enables us to get a spatiotemporal visualization of the resulting morphologies and, on the other hand, also serves as a model for potential precipitation processes already starting in the narrow rock pores in the seafloor. The microfluidic chamber of 500 μm thickness is prefilled with an acidic, iron-containing ocean analog, in which the alkaline fluid is injected at a constant flow rate using a high-precision syringe pump. Gradients and morphologies can be visualized with the aid of pH-sensitive dyes immersed into both fluids.

Variation of pH and flow rate

We found that the physical parameters influencing the resulting morphology are mainly flow rate and the alkalinity (i.e., the concentration) of the inflowing sodium hydroxide solution. By variation of these two parameters, we defined boundaries for each regime at which the final morphology is not altered by further changes in one of the parameters. The influence of flow rates and concentrations on the resulting morphologies is visualized using a universal pH indicator. The steady-state images, in which further inflow does not alter the morphology any more, are shown in Fig. 2. Different inflow rates of 2.0 to 10.0 ml hour^{-1} and alkaline concentrations from 0.2 to 1.0 M result in a diverse set of morphologies, from which three dominant structural patterns can be identified: "layers/rings," "precipitation fingers," and "flow fields." Flow fields form as large almost homogeneous areas of both fluids due to weak precipitation at low flow rate and/or low inflow concentrations, whereas layers and rings emerge as thick layered precipitates completely excluding the ocean fluid at high flow and strongly alkaline pH. In between the limits of both regimes, we observe precipitation fingers as parallel structures that maintain stable precipitation patterns. Higher concentrations of in-flowing sodium hydroxide, together with high flow rates, result in faster precipitation and stronger precipitate formation. The motion of the fluid flow entering the chamber is purely advection driven. Lowering flow and/or influx concentration further the initial motion gets increasingly diffusion governed. Therefore, the diffusive fields takes the longest time to reach the steady state since, even after complete filling of the chamber, intermixing of the fluids still continues via diffusion across the weak precipitate structures.

Time-dependent morphology formation

Variation of flow rate and concentration of the injected fluid showed that the three dominant morphologies emerge on different subsequent timescales. An even clearer visualization can be seen in Fig. 3, where the alkaline areas for each of the three morphologies are highlighted by a pH-dependent fluorescent dye [2′,7′-bis-(2-carboxyethyl)-5-(and-6)-carboxyfluorescein (BCECF)]. Among these three time-dependent patterns, layers/rings form within the first 10 to 15 s and fill up the complete chamber. For the mid-regime, initially thick layered precipitates grow until around 30 s, at which point the bulk flow is divided into multiple smaller flow trajectories that form the characteristic precipitation fingers. With

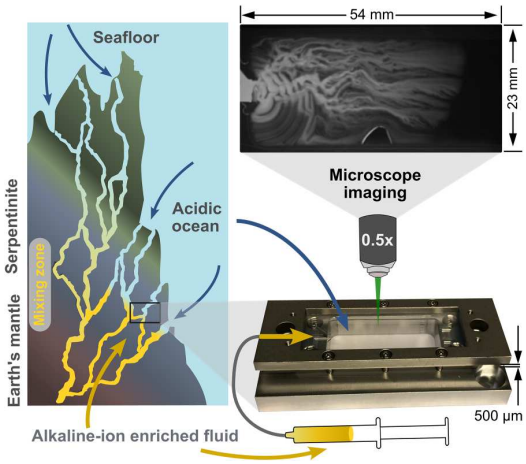

Fig. 1. Mixing of alkaline and acidic solutions in seafloor rock pores is mimicked in a microfluidic flow cell. Acidic ocean water percolates the narrow cracks and pores of the seafloor and is converted to an ion-enriched and strongly alkaline fluid by interaction with the surrounding rock. When this fluid is exhaled back into the ocean, rapid mineral precipitation happens upon contact with the ocean water. To mimic this scenario in the laboratory, an alkaline sodium-hydroxide solution is pumped at a controlled flow rate into a flat microfluidic chamber prefilled with an acidic iron solution. Microscope imaging with pH-dependent dyes allows the visualization of different morphologies, depending on inflow rate and OH^- concentration, and the assessment of emerging pH gradients.

increasing time, these precipitations get weaker and the fingers start to diffuse out perpendicularly to the flow direction until the top end of the chamber is reached. Similarly, in experiments revealing flow fields as dominating morphology, we observe the shaping of weak and thin finger-like precipitates within the first 120 s until the diffusive structure of the homogeneous flow fields dominates, due to mitigating precipitation. By varying OH^- ion concentration and inflow rate, we can control the timescales for the mineral precipitation pattern formation. The formation timescale gets longer for each of the dominating patterns and ranges from a few seconds (layers/rings) over 1 to 2 min (precipitation fingers) to above 3 min (flow fields), where no stable steady state could be observed within the measurement time. Comparing all three experiments, which exhibit one dominant morphology each (see Fig. 3), we can assess that the overall vent formation also scales over time.

pH-dependent dye and fluid flow

Apart from mapping the areas of different pH, the fluorescent dye also allows the tracing of flow and ion interchange over time (see Fig. 3). This is essential for the observation of two major features: gradient formation and their subsequent maintenance after entering the morphological steady state. Especially in the layers/rings, it can be seen that over time a main flow dominates through the center of the thick layers, leading to fading intensity of the fluorescent dye in the areas farther outside. This indicates a decrease in pH most likely due to ionic interchanges between the fluid and the mineral precipitates. However, this effect cannot be observed in the precipitation fingers as the flow is not bypassing earlier formed structures but rather divides into the smaller subflows forming the characteristic finger structures. The constant ion inflow maintains the fluorescence and, hence, the pH gradients even after reaching the steady state. The flow fields, on the other hand, show fading of the fluorescent dye by diffusing into the remaining ocean liquid due to weak and unstable mineral structures. This happens even though a similar subflow division as for the precipitation fingers can be seen in the beginning (Fig. 3). Because of this ongoing mixing of the two fluids by diffusion, all initially emerging gradients are equilibrating in the flow field morphology.

Potential for gradient formation

The potential of each morphology for the formation of gradients can be assessed from the final vent morphology of each time evolution in Fig. 3. The layer/ring structure does not allow for any gradients to form between alkaline fluid and acidic ocean analog, since all of the acidic liquid in the chamber is either consumed in precipitation or depleted from the chamber as it fills up with precipitate and alkaline solution. The only possible gradients would be the ones between shortcut flow and areas of fading pH as described above. However, those gradients would not be maintained and separated by a mineral membrane and thus equilibrate quickly by diffusion. This effect is shown in the plot of a cross-section through the chamber over time plot (Fig. 3C, right): The width of the blue (alkaline) areas decreases, as the fluorescence of the outer areas is depleted and a main flow forms. The same is valid for the flow field structures, since no steady state can be reached within the time of the experiment such that the fluids keep intermixing through the weak membranes forming between 30 and 200 s. Thus, the pH is equilibrating gradually, which can be seen by the faint edges of the precipitates in the dark-field images and the widening width of blue/white (alkaline) areas in the cross-section over time plot (Fig. 3A, right). In contrast to that, the precipitation finger structures show a clear pH difference of the fingers to the acidic solution in between. The strong precipitates act as a semipermeable mineral membrane that keeps high and low pH areas separated and, together with the continued inflow of OH^- ions, maintains the gradient even in the final state of the morphology. This can be clearly seen by the straight blue (alkaline) stripes in the cross-section versus time plot (Fig. 3B, right). Their width does not considerably vary over time, indicating a stable gradient between red (acidic) and blue (alkaline) areas. The maintenance of pH gradients across stable semipermeable membranes is a crucial feature for life as we know it today. The characteristic of pH gradient formation can only be observed for the precipitation fingers at mediate flow and concentration of inflowing fluid. Modern compartments, like cells, provide a similar setting: an alkaline interior separated by a membrane from an acidic surrounding. To keep the gradients across the membrane up, however, for cells mechanisms like transmembrane machines are needed to pump protons out of the cell (see fig. S2). In contrast, the finely finger-like structures in the microfluidic morphology would not require any active means or proton pumping as long as the flow of alkaline fluid continues.

Bead accumulation

The next step in testing the capabilities for compartmentalization is to check for potential accumulation of dissolved species in the fluids. We tested our different morphologies with fluorescent beads of 10 µm diameter. In Fig. 4, three experiments are shown with conditions yielding the dominant morphologies, but with dispersed fluorescent beads mixed in the inflowing fluid. It can be seen

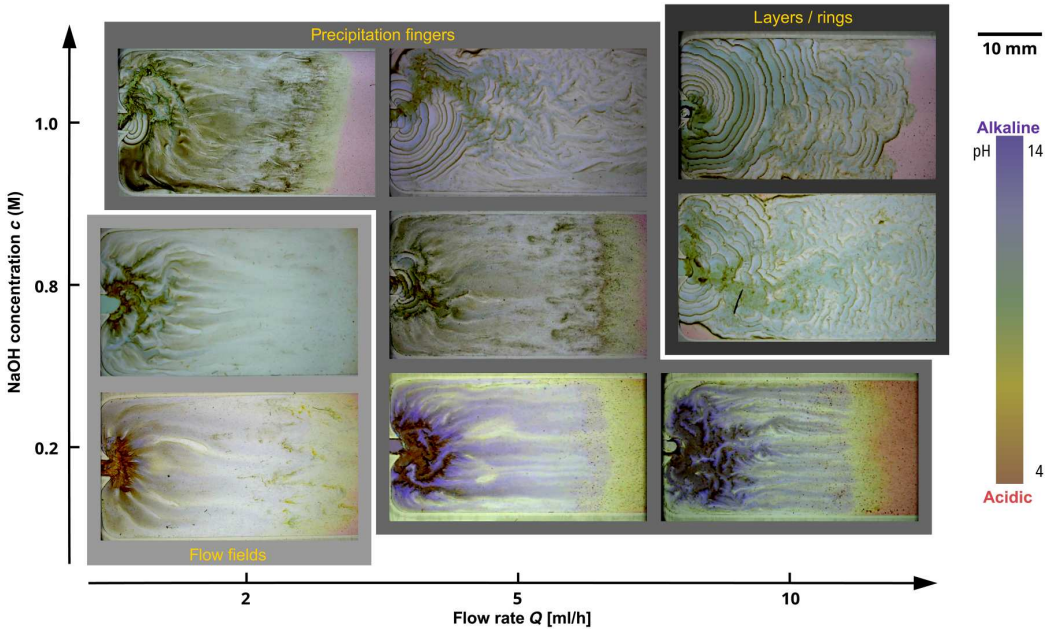

Fig. 2. Variation of inflow rate and concentration of the alkaline fluid. Injection of an NaOH solution into an ocean fluid containing 200 mM Fe(II)Cl_2 yields three dominant morphologies. Layers/rings form at high flow and concentrations, whereas diffusive fields persist at low values. In between both regimes, precipitate fingers form, which allow the formation and maintenance of steep pH gradients. At the higher limit, the acidic ocean is almost completely repressed by the precipitation front, and at the lower limit, both solution mix by diffusion due to weak precipitation. Therefore, no gradients can be formed or maintained in both limiting morphologies.

that beads are getting trapped inside the morphologies upon precipitation. In the flow fields (Fig. 4A), a very weak fluorescence signal indicates hardly any bead accumulation, which is most likely due to the weak precipitation and pH gradients. Although there appears to be a higher fluorescence signal in the layers/rings (Fig. 4C) due to their high inflow rate, most of the beads fade again over time as they are most likely flushed out. Nevertheless, beads are locally accumulated in some of the grooves along the fluid paths; however, they would not be subjected to any gradients or continued feeding after a shortcut flow forms after some time (see Fig. 3C). In the precipitation finger structures (Fig. 4B), we see that some beads are getting trapped in the precipitate upon formation, which forms local clusters of accumulated particles, increasing in fluorescence over time, which suggests continued accumulation over time as the influx persists. In this way, spots of locally increased concentration of accumulated particles form, which persist even after the precipitation process is finished.

DISCUSSION

Here, we showed that dominantly three different precipitation morphologies emerge in a quasi-2D AV model, which have different abilities to facilitate the emergence of pH gradients and accumulation of dispersed particles. In our studies, we identified flow rate and concentration of hydroxide ions (i.e., concentration of NaOH) in the inflowing fluid to be the critical parameters in structure formation and therefore focused on their variation in our experiments. Our data suggest that precipitation fingers, obtained at medium flow rates and medium concentrations of alkaline fluid within our boundaries, yield the steadiest gradients in terms of steepness and stability. Crucial for the formation of pH gradients is the subdivision of the flow into narrower "fingers" across the width of the chamber, which form strong mineral precipitates with the acidic solution in between. After reaching the morphological steady state, pH gradients are maintained by the continued inflow of hydroxide ions through all of the fingers. Although the layer/ring structures also exhibit strong precipitation barriers, they fail to generate gradients, since all of the ocean fluid is pushed out of the chamber by propagation of the precipitation front spanning across the whole chamber width (no acidic fluid enclosed). After some time, a main flow is established as a short cut through the morphologies, leading to fading fluorescence of the pH-dependent dye in the adjacent areas. This probably forms weak pH gradients between main flow and outer areas that are, however, not separated by a barrier. The lack of barriers seems also the problem for the flow fields as they hardly show any stable precipitate and therefore lack the ability to maintain gradients as the fluids just intermix through diffusion.

We observe that a change in the experimental parameters essentially corresponds to a shift of the morphology's formation timescale. This seems plausible, since precipitation happens more rapidly at higher concentrations and grows faster at higher flow rates. Therefore, we found that layers/rings form predominately within the first 20 s, then converge to the precipitation fingers between roughly 30 and 80 s, and finally fade into the diffusive fields after around 100 s as the local flow velocity ceases and diffusive movement dominates. In experiments exhibiting dominant precipitation fingers or flow fields, we can therefore observe small

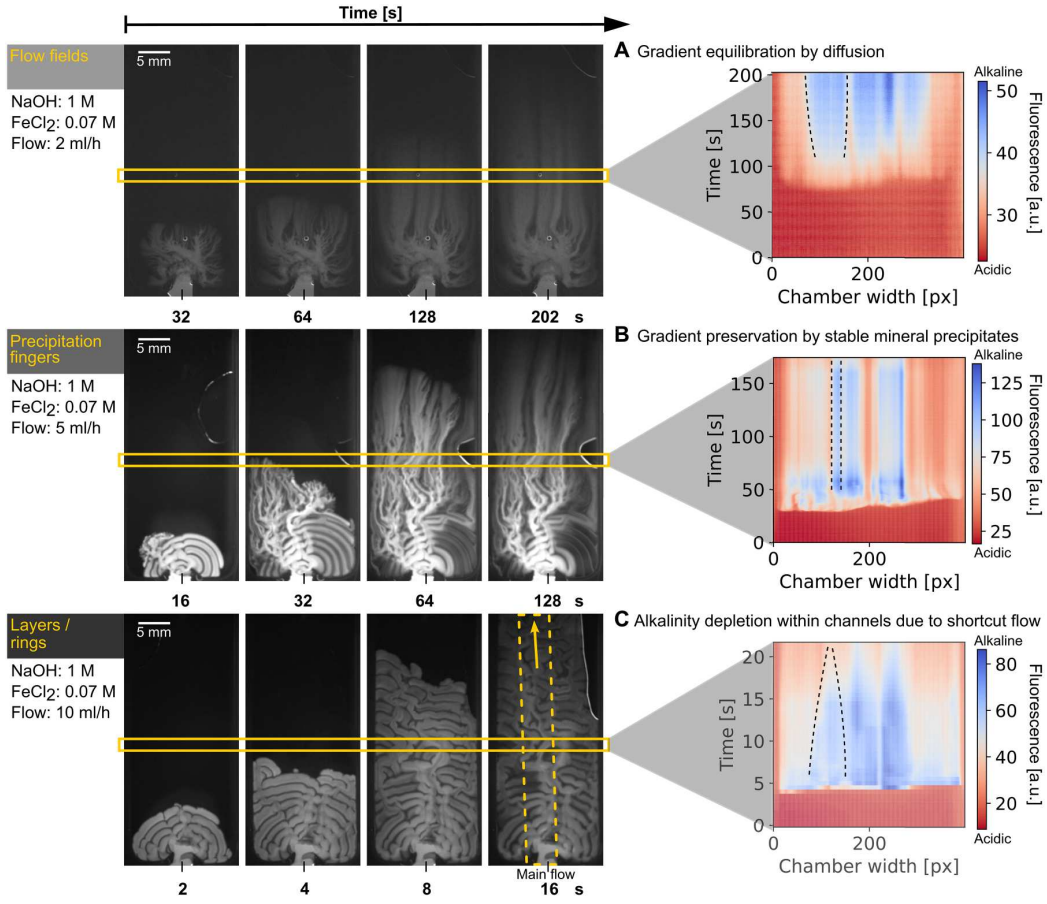

Fig. 3. Changes in inflow rate and concentration correspond to a timescale shift in morphology formation. Each of the three time series represents conditions that are dominated by one of the three morphologies. Layers/rings form predominately within the first 20 s, then converge to the finger structures between roughly 30 and 80 s, and finally fade into the flow fields after around 100 s. On the right, an average of 20 pixels in height over the cross-section of the chamber is plotted over time: (**A**) No steady state is reached and the fluids intermix by diffusion over time (blue areas become wider). (**B**) Stable gradients are formed between red (acidic) and blue (alkaline) areas and are maintained over time (straight blue stripes at persistent width). (**C**) In steady state, a dominant flow through the layers forms and fluorescence fades in adjacent structures, indicated by narrowing of the blue (alkaline) areas.

sections of the other two morphologies at the respective timescale. To promote the formation of gradients, precipitation fingers should be extended as far as possible, which works best by ensuring stable precipitates using medium to high OH^- concentration and medium flow rates.

In the experiments with fluorescent beads mixed into the inflowing solution, accumulation could only be deduced in the parallel precipitation finger structures and the layers/rings, which can be seen by the increasing fluorescence intensity of the agglomerates. While some of the beads are already trapped during the mineral precipitation process, more are accumulated as long as the inflow continues. This could be due to diffusiophoretic effects (*9*) or the advective flows through the resulting structures. However, in the layers/rings, the beads only seem to increase in the grooves and are thus not subject to either gradients or the continued inflow, after the shortcut flow establishes.

In the field of chemobrionics, confined quasi-2D flow setups (Hele-Shaw flow cells) are commonly used to study precipitation reactions and the resulting pattern formation. The experiments mostly use radial injection of the fluid (*10*, *41*, *42*, *45*–*47*) rather than injection from one side as in our setting. Although we used different injections and chemical compositions, Rocha *et al.* (*46*) showed the formation of similar morphologies over the time of the experiment. However, none of the patterns identified in the referenced literature coincides exactly with our dominant morphologies, which would make our setting also interesting for modeling of the pattern formation process.

Modern AV systems, such as Lost City, can be seen as an example to our model by structure, but not by chemical composition. We selected the fluids to resemble the crucial conditions that allow the precipitation of minerals upon contact and are assumed to have been prevalent on an early Earth. Although we did not aim to recreate the formation of any specific minerals, it is likely that

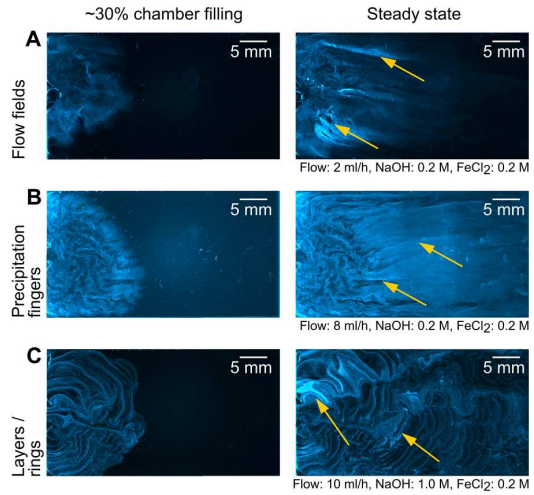

Fig. 4. Accumulation of fluorescent beads in the different dominant morphologies. Ten-micrometer fluorescent beads are dispersed into the alkaline fluid to visualize accumulation in layers/rings (**A**), precipitation fingers (**B**), and flow fields (**C**). Strongest local increase of fluorescence is observed in the precipitation fingers (B), suggesting the accumulation of dispersed beads.

we create white and green rust (amakinite and fougerite) as shown in previous work under comparable conditions (*15*). Although Lost City is considered a low-temperature AV system, the vented fluids still have temperatures 40° to 75°C (*24*, *25*). Our results presented here were mainly focused on experiments carried out at room temperature, but as fig. S3 shows, the injection of heated fluids seems not to have any notable influence on the resulting morphologies. Our setup forms the technical basis to test many other geochemical reagents in a microfluidic setting, which would, however, exceed the scope of this paper. Particularly interesting would be the integration of carbonate as occurring in modern Lost City–type vents (*24*, *25*) and sulfide. Both of them were also likely abundant on an early Earth (*1*–*3*) and are even providing promising catalytic capabilities known from highly reactive metal sulfides like Fe(Ni)S minerals (*23*, *52*–*54*). So far, sulfides were not included in the system due to safety reason and the potential formation of H_2S gas. Future experiments may not only involve further reagents but also aim to sufficiently extract the formed precipitates from the microfluidic cell and subsequent analysis with Raman spectroscopy or scanning electron microscopy (*15*).

Our setup allows to study the AV formation process in quasi–two dimensions, thereby providing full optical access for fluorescence and bright-field visualization and allowing for the precise control of chamber thickness and inflow rate. All previous attempts to recreate the AV formation process in the laboratory were focused on a 3D setup (*23*, *37*). Because of technical limitations of our microscope, the flow cell could only be located horizontally in our experiments, but given the close density values of the fluids (table S1), buoyancy effect would be negligible. The 2D representation serves as a model for the precipitation process in 3D and only requires sample volumes lower than 100 µl. As the AV precipitates provide highly reactive mineral surfaces (*13*, *15*), this would also provide a promising setting to study the effect of minerals and gradients on origins of life–related chemical reactions in low volumes. Apart from that, the confined geometry could probably be seen not only as a model but also as a potential geological scenario, considering the possibility that the vent precipitation process could already start in the cracks of the crust before the fluids are exhaled into the bulk ocean waters.

From an origins of life perspective, the quasi-2D scenario could satisfy several requirements, which are thought to be crucial for the emergence of living systems. Essentially, all life we know today depends on nonequilibria and, thus, requires gradients of ions and pH that are separated by a semipermeable membrane (*9*). In the alkaline hydrothermal vent theory, it is therefore considered that geochemical gradients could pose an early precursor to the topology of living systems, given their structural similarities to autotrophic cells (*3*, *9*). This is also clearly reflected in our precipitation finger morphology, with the alkaline fluid streaming inside the finger structures, which are separated by a thin mineral barrier from the more acidic ocean solution in between the streams.

In order for chemical reactions to happen and to start molecular evolution, it requires high concentration of molecules and means to localize reagents and products to avoid dilution in an extensive ocean, an issue usually referred to as the "concentration problem" (*55*). Via diffusiophoresis, the ion gradients could facilitate a directed colloid transport (*9*) in addition to the trapping of dissolved species in the physical structure of the morphologies (e.g., formed pockets) to even further boost the accumulation of (macro-)molecules. Further, accumulation could be aided by thermophoresis due to temperature gradients between the two fluids (*56*). This would enhance the local concentration of dissolved molecules, which in turn could be localized by trapping or interaction with the minerals (*15*) and eventually participate in reactions catalyzed by the minerals. Further experiments will also consider 2D matrix-assisted laser desorption/ionization (MALDI) imaging of the dried precipitates to map out local accumulation sites of different organic molecules within the mineral structures.

Theoretical ideas also suggest that steep proton gradients across the thin mineral membranes in AVs could facilitate CO_2 reduction that enables abiotic organic syntheses similar to the acetyl–coenzyme A pathway in bacteria and archea (*3*, *23*, *57*). Recent experimental work (*21*–*23*), however, has shown only very low yields of simple organic products so far. Also, because of that, electrochemical gradients in AVs may pose an important role by combining strongly opposing conditions (high-low pH or reduced-oxidized) for different or subsequent chemical reactions (*13*) in close spatial proximity and driving diffusiophoretic accumulation of dilute molecules (*9*) at catalytically active mineral surfaces (*3*, *9*, *14*). The catalytic potential of different iron sulfide minerals has been shown in recent experimental publications for the reduction of CO_2 (*53*, *54*, *58*) and also the effect of oxyhydroxide minerals on product selectivity in amino acid synthesis (*13*).

We investigated the precipitation of hydrothermal vent morphologies in a quasi-2D setting. We found that finger-like precipitates at medium flow rate and OH^- concentration allow for the generation and maintenance of pH gradients and facilitate the accumulation of dispersed particles at the same time. Considering the possibility that AV precipitation could already happen within the fractures of the seafloor, the confined geometry could even be a promising mimic of geological scenario. Our microfluidic setup allows the spatiotemporal visualization of the precipitation

process and the emerging gradients with universal and fluorescent pH dyes. This could open the door for laboratory experiments in low volume to study the impact of AV environments on accumulation of organic molecules, catalytic reactions, and processes like polymerization or replication of biopolymers.

MATERIALS AND METHODS

The microfluidic setup (fig. S1A) is a custom-made flow cell consisting of a 2D rectangular geometry (16 mm × 40 mm) with inlet/outlet channels (fig. S1C) cut out of a 500-μm-thick sheet of fluorinated ethylene propylene (FEP). To form a closed chamber, the sheet is sandwiched between two transparent sapphire plates of size 22 mm × 60 mm with a thickness of 1.0 mm (top) and 0.5 mm (bottom). The three layers are pressed together by a steel frame screwed on an aluminum base to tightly seal the chamber. Hydrodynamic access to the chamber is provided by a total of four holes in the thin bottom sapphire that are connected to polytetrafluoroethylene (PTFE) tubings (inside diameter, 180 μm) via standard low-pressure fittings, ferrules, and corresponding threads in the aluminum base.

Microscopy and visualization

For visualization of the chamber's interior, the setup is placed on the stage of a microscope (Axio Zoom.V16, Carl Zeiss, Germany) using a 3D-printed support frame. For bright-field imaging, the chamber is illuminated by the microscope's built-in white light source from below, whereas for fluorescence imaging the sample is excited from above by the white light from a light engine (SOLA 80-10247, Lumencor, USA) coupled with a Zeiss 38 He filter to generate a 470/40-mm light through the objective lens (0.5×). Images are recorded using a complementary metal-oxide semiconductor (CMOS) camera (ORCA-Flash 4.0, Hamamatsu, Japan) or a mirrorless photographic camera (Lumix DC-G100K, Panasonic, Japan) for color imaging mounted to the microscope with a C-mount adapter.

Microfluidics

The chamber is prefilled manually with the ocean analog, whereas injection of the alkaline fluid is controlled by a pulsation-free, continuous-flow syringe pump (Nemesys S, Cetoni, Germany) operated with glass syringes (1 ml) at varying flow rates of 1.0 to 15.0 ml $hour^{-1}$.

The FEP cutout (fig. S1C) features channels of 1.7 mm width that connect the rectangular cell to the holes in the sapphire. In preparation of the experiment, the chamber is prefilled with ocean analog solution through the top outlet channels while keeping the inlet channels closed to avoid precipitation happening in the channels. To avoid bubbles in the chamber, the alkaline solution is slowly pumped into the inlet channel (2 ml $hour^{-1}$) while simultaneously retrieving the air through the drainage channel at the same rate. All motion is stopped when the fluid front is 2 mm from entering the chamber, the drainage channel is closed, and the experiment is started at the desired flow rate.

Sample preparation

The acidic ocean analog is prepared by dissolving iron(II)chloride tetrahydrate [$Fe(II)Cl_2 \cdot 4H_2O$] (Sigma-Aldrich, USA) in nuclease-free water (Ambion, Invitrogen, Thermo Fisher Scientific, USA) to reach concentrations of either 75 or 200 mM. To keep oxidation of the solution to a minimum, iron(II)chloride tetrahydrate is stored under inert gas (argon) and all flasks and vials are preflushed with argon gas. As alkaline fluid, a commercial volumetric standard solution of sodium hydroxide [NaOH] (Carl Roth, Germany) is either used as purchased (1 M) or diluted with nuclease-free water to reach the desired concentration. Depending on the experiment, the fluids are used directly, mixed in a ratio of 8:1 with a universal pH dye (KS90-UpHI, Lovibond, Tintometer, Germany), or mixed 50:1 with a solution of BCECF (Invitrogen, Thermo Fisher Scientific, USA) for fluorescent imaging. For visualization of fluid flow and particle accumulation, the inflowing sodium hydroxide solution was mixed in a ratio of 18:1 with a 2.5% aqueous suspension of 10-μm fluorescent (bright blue) carboxylate polystyrene microspheres (Fluoresbrite, Polysciences, USA).

Supplementary Materials

This PDF file includes:
Figs. S1 to S4
Table S1
Legends for movies S1 to S9

Other Supplementary Material for this manuscript includes the following:
Movies S1 to S9

REFERENCES AND NOTES

1. M. J. Russell, A. J. Hall, The emergence of life from iron monosulphide bubbles at a submarine hydrothermal redox and pH front. *J. Geol. Soc. London* **154**, 377–402 (1997).
2. W. Martin, J. Baross, D. Kelley, M. J. Russell, Hydrothermal vents and the origin of life. *Nat. Rev. Microbiol.* **6**, 805–814 (2008).
3. V. Sojo, B. Herschy, A. Whicher, E. Camprubí, N. Lane, The origin of life in alkaline hydrothermal vents. *Astrobiology* **16**, 181–197 (2016).
4. N. G. Holm, Why are hydrothermal systems proposed as plausible environments for the origin of life?, in *Marine Hydrothermal Systems and the Origin of Life* (Springer Netherlands, 1992), pp. 5–14.
5. S. W. Poulton, D. E. Canfeld, Ferruginous conditions: A dominant feature of the ocean through Earth's history. *Elements* **7**, 107–112 (2011).
6. E. G. Nisbet, The geological setting of the earliest life forms. *J. Mol. Evol.* **21**, 289–298 (1985).
7. M. Preiner, J. C. Xavier, F. L. Sousa, V. Zimorski, A. Neubeck, S. Q. Lang, H. Chris Greenwell, K. Kleinermanns, H. Tüysüz, T. M. McCollom, N. G. Holm, W. F. Martin, Serpentinization: Connecting geochemistry, ancient metabolism and industrial hydrogenation. *Life* **8**, 41 (2018).
8. M. J. Russell, A. J. Hall, W. Martin, Serpentinization as a source of energy at the origin of life. *Geobiology* **8**, 355–371 (2010).
9. F. M. Möller, F. Kriegel, M. Kieß, V. Sojo, D. Braun, Steep pH gradients and directed colloid transport in a microfluidic alkaline hydrothermal pore. *Angew. Chem. Int. Ed.* **56**, 2340–2344 (2017).
10. Q. Wang, K. S. Hernesman, O. Steinbock, Flow-driven precipitation patterns with microemulsions in a confined geometry. *ChemSystemsChem* **2**, e1900037 (2020).
11. C. F. Dirscherl, A. Ianeselli, D. Tetiker, T. Matreux, R. M. Queener, C. B. Mast, D. Braun, A heated rock crack captures and polymerizes primordial DNA and RNA. *Phys. Chem. Chem. Phys.* **25**, 3375–3386 (2023).
12. T. Matreux, B. Altaner, J. Raith, D. Braun, C. B. Mast, U. Gerland, Formation mechanism of thermally controlled ph gradients. *Commun. Phys.* **6**, 14 (2023).
13. L. M. Barge, E. Flores, M. M. Baum, D. G. Velde, M. J. Russell, Redox and pH gradients drive amino acid synthesis in iron oxyhydroxide mineral systems. *Proc. Natl. Acad. Sci. U.S.A.* **116**, 4828–4833 (2019).
14. N. H. Sleep, A. Meibom, T. Fridriksson, R. G. Coleman, D. K. Bird, H2-rich fluids from serpentinization: Geochemical and biotic implications. *Proc. Natl. Acad. Sci. U.S.A.* **101**, 12818–12823 (2004).
15. V. Helmbrecht, M. Weingart, F. Klein, D. Braun, W. D. Orsi, White and green rust chimneys accumulate RNA in a ferruginous chemical garden. arXiv:2212.02793 [physics.geo-ph] (6 December 2022).

16. S. Duhr, D. Braun, Why molecules move along a temperature gradient. *Proc. Natl. Acad. Sci. U.S.A.* **103**, 19678–19682 (2006).
17. P. Baaske, F. M. Weinert, S. Duhr, K. H. Lemke, M. J. Russell, D. Braun, Extreme accumulation of nucleotides in simulated hydrothermal pore systems. *Proc. Natl. Acad. Sci. U.S.A.* **104**, 9346–9351 (2007).
18. A. V. Dass, S. Wunnava, J. Langlais, B. von der Esch, M. Krusche, L. Ufer, N. Chrisam, R. C. A. Dubini, F. Gartner, S. Angerpointner, C. F. Dirscherl, P. Rovó, C. B. Mast, J. E. Šponer, C. Ochsenfeld, E. Frey, D. Braun, RNA oligomerisation without added catalyst from 2′,3′-cyclic nucleotides by drying at air-water interfaces. *ChemSystemsChem* **5**, e202200026 (2023).
19. C. B. Mast, D. Braun, Thermal trap for DNA replication. *Phys. Rev. Lett.* **104**, 188102 (2010).
20. C. B. Mast, S. Schink, U. Gerland, D. Braun, Escalation of polymerization in a thermal gradient. *Proc. Natl. Acad. Sci. U.S.A.* **110**, 8030–8035 (2013).
21. V. Sojo, A. Ohno, S. E. McGlynn, Y. M. A. Yamada, R. Nakamura, Microfluidic reactors for carbon fixation under ambient-pressure alkaline-hydrothermal-vent conditions. *Life* **9**, 16 (2019).
22. R. Hudson, R. de Graaf, M. S. Rodin, A. Ohno, N. Lane, S. E. McGlynn, Y. M. A. Yamada, R. Nakamura, L. M. Barge, D. Braun, V. Sojo, CO_2 reduction driven by a pH gradient. *Proc. Natl. Acad. Sci. U.S.A.* **117**, 22873–22879 (2020).
23. B. Herschy, A. Whicher, E. Camprubi, C. Watson, L. Dartnell, J. Ward, J. R. G. Evans, N. Lane, An origin-of-life reactor to simulate alkaline hydrothermal vents. *J. Mol. Evol.* **79**, 213–227 (2014).
24. D. S. Kelley, J. A. Karson, D. K. Blackman, G. L. Früh-Green, D. A. Butterfield, M. D. Lilley, E. J. Olson, M. O. Schrenk, K. K. Roe, G. T. Lebon, P. Rivizzigno; AT3-60 Shipboard Party, An off-axis hydrothermal vent field near the Mid-Atlantic Ridge at 30° N. *Nature* **412**, 145–149 (2001).
25. D. S. Kelley, J. A. Karson, G. L. Früh-Green, D. R. Yoerger, T. M. Shank, D. A. Butterfield, J. M. Hayes, M. O. Schrenk, E. J. Olson, G. Proskurowski, M. Jakuba, A. Bradley, B. Larson, K. Ludwig, D. Glickson, K. Buckman, A. S. Bradley, W. J. Brazelton, K. Roe, M. J. Elend, A. Delacour, S. M. Bernasconi, M. D. Lilley, J. A. Baross, R. E. Summons, S. P. Sylva, A serpentinite-hosted ecosystem: The Lost City hydrothermal field. *Science* **307**, 1428–1434 (2005).
26. W. Bach, H. Paulick, C. J. Garrido, B. Ildefonse, W. P. Meurer, S. E. Humphris, Unraveling the sequence of serpentinization reactions: Petrography, mineral chemistry, and petrophysics of serpentinites from MAR 15°N (ODP Leg 209, Site 1274). *Geophys. Res. Lett.* **33**, (2006).
27. G. Macleod, C. McKeown, A. J. Hall, M. J. Russell, Hydrothermal and oceanic pH conditions of possible relevance to the origin of life. *Orig. Life Evol. Biosph.* **24**, 19–41 (1994).
28. I. Halevy, A. Bachan, The geologic history of seawater pH. *Science* **355**, 1069–1071 (2017).
29. E. D. Swanner, N. Lambrecht, C. Wittkop, C. Harding, S. Katsev, J. Torgeson, S. W. Poulton, The biogeochemistry of ferruginous lakes and past ferruginous oceans. *Earth Sci. Rev.* **211**, 103430 (2020).
30. T. Altair, L. G. F. Borges, D. Galante, H. Varela, Experimental approaches for testing the hypothesis of the emergence of life at submarine alkaline vents. *Life* **11**, 777 (2021).
31. U. Pedreira-Segade, C. Feuillie, M. Pelletier, L. J. Michot, I. Daniel, Adsorption of nucleotides onto ferromagnesian phyllosilicates: Significance for the origin of life. *Geochim. Cosmochim. Acta* **176**, 81–95 (2016).
32. J. S. Beard, B. R. Frost, P. Fryer, A. McCaig, R. Searle, B. Ildefonse, P. Zinin, S. K. Sharma, Onset and progression of serpentinization and magnetite formation in olivine-rich troctolite from IODP Hole U1309D. *J. Petrol.* **50**, 387–403 (2009).
33. F. Trolard, S. Duval, W. Nitschke, B. Ménez, C. Pisapia, J. Ben Nacib, M. Andréani, G. Bourrié, Mineralogy, geochemistry and occurrences of fougerite in a modern hydrothermal system and its implications for the origin of life. *Earth Sci. Rev.* **225**, 103910 (2022).
34. S. E. McGlynn, I. Kanik, M. J. Russell, Peptide and RNA contributions to iron-sulphur chemical gardens as life's first inorganic compartments, catalysts, capacitors and condensers. *Philos. Trans. R. Soc. A Math. Phys. Eng. Sci.* **370**, 3007–3022 (2012).
35. L. M. Barge, Y. Abedian, I. J. Doloboff, J. E. Nuñez, M. J. Russell, R. D. Kidd, I. Kanik, Chemical gardens as flow-through reactors simulating natural hydrothermal systems. *J. Vis. Exp.* **2015**, 53015 (2015).
36. B. T. Burcar, L. M. Barge, D. Trail, E. B. Watson, M. J. Russell, L. B. McGown, RNA oligomerization in laboratory analogues of alkaline hydrothermal vent systems. *Astrobiology* **15**, 509–522 (2015).
37. L. M. Barge, S. S. S. Cardoso, J. H. E. Cartwright, G. J. T. Cooper, L. Cronin, A. De Wit, I. J. Doloboff, B. Escribano, R. E. Goldstein, F. Haudin, D. E. H. Jones, A. L. Mackay, J. Maselko, J. J. Pagano, J. Pantaleone, M. J. Russell, C. I. Sainz-Díaz, O. Steinbock, D. A. Stone, Y. Tanimoto, N. L. Thomas, From chemical gardens to chemobrionics. *Chem. Rev.* **115**, 8652–8703 (2015).
38. J. H. E. Cartwright, J. M. García-Ruiz, M. L. Novella, F. Otálora, Formation of chemical gardens. *J. Colloid Interface Sci.* **256**, 351–359 (2002).
39. D. A. Stone, B. Lewellyn, J. C. Baygents, R. E. Goldstein, Precipitative growth templated by a fluid jet. *Langmuir* **21**, 10916–10919 (2005).
40. F. Haudin, J. H. E. Cartwright, F. Brau, A. De Wit, Spiral precipitation patterns in confined chemical gardens. *Proc. Natl. Acad. Sci. U.S.A.* **111**, 17363–17367 (2014).
41. E. Balog, P. Papp, Á. Tóth, D. Horváth, G. Schuszter, The impact of reaction rate on the formation of flow-driven confined precipitate patterns. *Phys. Chem. Chem. Phys.* **22**, 13390–13397 (2020).
42. K. V. Bere, E. Nez, E. Balog, L. Janovák, D. Sebők, Á. Kukovecz, C. Roux, V. Pimienta, G. Schuszter, Enhancing the yield of calcium carbonate precipitation by obstacles in laminar flow in a confined geometry. *Phys. Chem. Chem. Phys.* **23**, 15515–15521 (2021).
43. C. I. Sainz-Díaz, E. Escamilla-Roa, J. H. E. Cartwright, Growth of self-assembling tubular structures of magnesium oxy/hydroxide and silicate related with seafloor hydrothermal systems driven by serpentinization. *Geochem. Geophys. Geosyst.* **19**, 2813–2822 (2018).
44. Y. Ding, C. M. Gutiérrez-Ariza, M. Zheng, A. Felgate, A. Lawes, C. I. Sainz-Díaz, J. H. E. Cartwright, S. S. S. Cardoso, Downward fingering accompanies upward tube growth in a chemical garden grown in a vertical confined geometry. *Phys. Chem. Chem. Phys.* **24**, 17841–17851 (2022).
45. G. Schuszter, F. Brau, A. De Wit, Flow-driven control of calcium carbonate precipitation patterns in a confined geometry. *Phys. Chem. Chem. Phys.* **18**, 25592–25600 (2016).
46. L. A. M. Rocha, L. Thorne, J. J. Wong, J. H. E. Cartwright, S. S. S. Cardoso, Archimedean spirals form at low flow rates in confined chemical gardens. *Langmuir* **38**, 6700–6710 (2022).
47. A. Comolli, A. De Wit, F. Brau, Dynamics of $A + B \rightarrow C$ reaction fronts under radial advection in a Poiseuille flow. *Phys. Rev. E* **104**, 044206 (2021).
48. S. Leduc, *The Mechanism of Life* (Rebman, 1911).
49. Q. Wang, O. Steinbock, Materials synthesis and catalysis in microfluidic devices: Prebiotic chemistry in mineral membranes. *ChemCatChem* **12**, 63–74 (2020).
50. B. C. Batista, O. Steinbock, Growing inorganic membranes in microfluidic devices: Chemical gardens reduced to linear walls. *J. Phys. Chem. C* **119**, 27045–27052 (2015).
51. Q. Wang, L. M. Barge, O. Steinbock, Microfluidic production of pyrophosphate catalyzed by mineral membranes with steep pH gradients. *Chemistry* **25**, 4732–4739 (2019).
52. L. M. White, R. Bhartia, G. D. Stucky, I. Kanik, M. J. Russell, Mackinawite and greigite in ancient alkaline hydrothermal chimneys: Identifying potential key catalysts for emergent life. *Earth Planet. Sci. Lett.* **430**, 105–114 (2015).
53. T. Beyazay, K. S. Belthle, C. Farès, M. Preiner, J. Moran, W. F. Martin, H. Tüysüz, Ambient temperature CO_2 fixation to pyruvate and subsequently to citramalate over iron and nickel nanoparticles. *Nat. Commun.* **14**, 570 (2023).
54. T. Beyazay, C. Ochoa-Hernández, Y. Song, K. S. Belthle, W. F. Martin, H. Tüysüz, Influence of composition of nickel-iron nanoparticles for abiotic CO_2 conversion to early prebiotic organics. *Angew. Chem. Int. Ed.* **62**, e202218189 (2023).
55. C. De Duve, R. De Neufville, *Blueprint for a Cell: The Nature and Origin of Life* (Carolina Biological Supply Company, 1991).
56. L. Keil, M. Hartmann, S. Lanzmich, D. Braun, Probing of molecular replication and accumulation in shallow heat gradients through numerical simulations. *Phys. Chem. Chem. Phys.* **18**, 20153–20159 (2016).
57. A. Yamaguchi, M. Yamamoto, K. Takai, T. Ishii, K. Hashimoto, R. Nakamura, Electrochemical CO_2 reduction by Ni-containing iron sulfides: How is CO_2 electrochemically reduced at bisulfide-bearing deep-sea hydrothermal precipitates? *Electrochim. Acta* **141**, 311–318 (2014).
58. M. Preiner, K. Igarashi, K. B. Muchowska, M. Yu, S. J. Varma, K. Kleinermanns, M. K. Nobu, Y. Kamagata, H. Tüysüz, J. Moran, W. F. Martin, A hydrogen-dependent geochemical analogue of primordial carbon and energy metabolism. *Nat. Ecol. Evol.* **4**, 534–542 (2020).

Acknowledgments: We thank L. S. Gigou for assistance in preliminary experiments, A. Schmid and C. F. Dirscherl for extensive comments on figures and manuscript, and J. H. Cartwright for comments on data and manuscript. **Funding:** This work was supported by the European Research Council (ERC) Evotrap, grant no. 787356 (D.B.); the Deutsche Forschungsgemeinschaft (DFG, German Research Foundation)—Project-ID 364653263—TRR 235 (CRC 235) (D.B. and W.D.O.); and the Max Planck Society (K.A.). **Author contributions:** M.W., D.B., and K.A. designed the experiments. M.W., C.D., and S.C. performed all experiments. V.H. and W.D.O. developed the sample composition and gave major input on geological interpretation. M.W., S.C., V.H., W.D.O., and K.A. analyzed the data. K.A. and D.B. supervised the project. M.W. wrote the manuscript, and all authors commented on the manuscript and contributed to the writing process. All authors edited and reviewed the manuscript for resubmission. **Competing interests:** The authors declare that they have no competing interests. **Data and materials availability:** All data needed to evaluate the conclusions in the paper are present in the paper and/or the Supplementary Materials. The collected experimental data are openly available in the mediaTUM repository under URL/DOI: doi.org/10.14459/2023mp1716502.

Submitted 24 April 2023
Accepted 30 August 2023
Published 29 September 2023
10.1126/sciadv.adi1884

Received: 24 April 2023 | Revised: 17 July 2023 | Accepted: 12 August 2023

DOI: 10.1111/gbi.12572

ORIGINAL ARTICLE

gebiology WILEY

White and green rust chimneys accumulate RNA in a ferruginous chemical garden

Vanessa Helmbrecht[1] | Maximilian Weingart[2] | Frieder Klein[3] | Dieter Braun[2] | William D. Orsi[1,4]

[1]Department for Geo- and Environmental Sciences, Palaeontology & Geobiology, Ludwig-Maximilians-Universität, Munich, Germany

[2]Systems Biophysics, Faculty of Physics, Ludwig-Maximilians-Universität, Munich, Germany

[3]Department of Marine Chemistry and Geochemistry, Woods Hole Oceanographic Institution, Woods Hole, Massachusetts, USA

[4]GeoBio-Center[LMU], Ludwig-Maximilians-Universität München, Munich, Germany

Correspondence
William D. Orsi, Department for Geo- and Environmental Sciences, Palaeontology & Geobiology, Ludwig-Maximilians-Universität, 80333 Munich, Germany.
Email: w.orsi@lrz.uni-muenchen.de

Funding information
Deutsche Forschungsgemeinschaft; Germanys Excellence Strategy

Abstract

Mechanisms of nucleic acid accumulation were likely critical to life's emergence in the ferruginous oceans of the early Earth. How exactly prebiotic geological settings accumulated nucleic acids from dilute aqueous solutions, is poorly understood. As a possible solution to this concentration problem, we simulated the conditions of prebiotic low-temperature alkaline hydrothermal vents in co-precipitation experiments to investigate the potential of ferruginous chemical gardens to accumulate nucleic acids via sorption. The injection of an alkaline solution into an artificial ferruginous solution under anoxic conditions (O_2 < 0.01% of present atmospheric levels) and at ambient temperatures, caused the precipitation of amakinite ("white rust"), which quickly converted to chloride-containing fougerite ("green rust"). RNA was only extractable from the ferruginous solution in the presence of a phosphate buffer, suggesting RNA in solution was bound to Fe^{2+} ions. During chimney formation, this iron-bound RNA rapidly accumulated in the white and green rust chimney structure from the surrounding ferruginous solution at the fastest rates in the initial white rust phase and correspondingly slower rates in the following green rust phase. This represents a new mechanism for nucleic acid accumulation in the ferruginous oceans of the early Earth, in addition to wet-dry cycles and may have helped to concentrate RNA in a dilute prebiotic ocean.

KEYWORDS
alkaline vents, emergence of life, ferruginous, green rust, RNA accumulation, white rust

1 | INTRODUCTION

There are many theories on a possible emergence of life at alkaline hydrothermal vents (AHVs) on Earth. The "RNA world" theory (Gilbert, 1986), and the "metabolism first" theory at AHVs (Martin et al., 2008) feature prominently in the discussion about the emergence of life and are now considered to be not necessarily mutually exclusive (Preiner et al., 2020). A key unknown in the emergence of life is, how nucleic acids could overcome the large dilution factor of the prebiotic oceans, which has been referred to as the "concentration problem" (De Duve, 1991). It has been proposed, that AHV chimneys could accumulate nucleic acids including RNA during the RNA world (Martin & Russell, 2003). In this scenario, AHV chimneys provide an alternative RNA concentration site to the wet-dry cycles that have been proposed for 'warm little ponds' (Damer & Deamer, 2020; Darwin, 1871; Pearce et al., 2017).

Few studies so far have shown evidence for compatibility of nucleic acids within an AHV environment (Altair et al., 2021; Baaske et al., 2007; Burcar et al., 2015; Mast & Braun, 2010) but RNA accumulation dynamics at an AHV are poorly understood. Some studies that focus on the adsorption of RNA test mineral surfaces like iron sulfides (Mizuuchi et al., 2019) or clay minerals (Pedreira-Segade et al., 2016).

Compared to modern oceans, prebiotic oceans of the Hadean and Archean were likely more acidic and ferruginous, that is, anoxic conditions with high concentrations of dissolved iron (Poulton & Canfield, 2011). As soon as liquid water oceans were present on Earth ~4.4 Ga ago (Heller et al., 2021; Mojzsis et al., 2001), water would have interacted with ultramafic to mafic seafloor rocks, resulting in widespread hydrothermal alteration, including serpentinization across the Hadean seafloor (Figure 1a; Rouillard et al., 2018; White et al., 2020). The pH of the emanating fluids is increasingly alkaline pH with decreasing temperatures (Klein et al., 2013; Rouillard et al., 2018).

The likely ferruginous conditions of the prebiotic oceans suggest the existence of a different kind of chimney at AHVs on early Earth (Figure 1b) compared to the white calcium carbonate and brucite smokers seen at Lost City today (Kelley et al., 2001), and other serpentinization hosted systems (Charlou et al., 1998). However assuming a circumneutral pH (~6.6) of the ocean around 4.0 Ga, it has been proposed that carbonates and brucite could have existed as well (Krissansen-Totton et al., 2018). Previous studies argue for the presence of "green rust" as an important mineral in the emergence of life at AHVs, since green rust can form inorganic membranes to maintain disequilibria between the acidic ocean and the alkaline interior of the vents (Altair et al., 2021; Arrhenius, 2003; Barge et al., 2015; Duval et al., 2019; Halevy et al., 2017; Russell, 2018). The highly redox-reactive mineral green rust is a ferrous-ferric oxyhydroxide also known as fougerite (Bernal et al., 1959; Halevy et al., 2017; Trolard et al., 2007). Amakinite or "white rust", the rare ferrous analogue of brucite, is the precursor phase of fougerite and was detected in the basement rocks below the Lost City hydrothermal field (Beard et al., 2009; Trolard et al., 2022).

Despite acknowledging the minerals' significance in an emergence of life context, experimental evidence for alkaline vents made out of white and green rust chimneys, is scarce (Altair et al., 2021). Moreover, their capability to accumulate nucleic acids to avoid dilution in a prebiotic ocean, to our knowledge, has not been tested. Therefore, we tested the hypothesis that AHV chimneys can concentrate RNA (Martin & Russell, 2003), offering a potential solution to the 'concentration problem' (De Duve, 1991).

We created alkaline vents under ferruginous conditions thought to a defining feature of the prebiotic oceans (Poulton & Canfield, 2011) under O_2 concentrations less than 0.01% of present atmospheric levels. Within these ferruginous chemical gardens, chimney structures composed of the iron-containing hydroxide white rust and the layered double hydroxide green rust form across strong pH gradients. We show that the chimneys accumulate RNA from the surrounding ferruginous solution at rates that depend on the formation of white and green rust. In a prebiotic ocean on early Earth, this process may have helped to overcome dilution of the RNA to very low concentrations, supporting the hypothesis that AHV chimneys can concentrate RNA in a ferruginous environment (Martin & Russell, 2003).

2 | METHODS

2.1 | Experimental setup

Similar to previous AHV experiments (Altair et al., 2021; Barge et al., 2015), our experimental setup was designed to mimic ferruginous early Earth conditions (Figure 1a). Five AHV experimental replicates were performed in an anaerobic chamber (MBRAUN Labstar) containing a N_2 atmosphere to maintain anoxic conditions. Oxygen

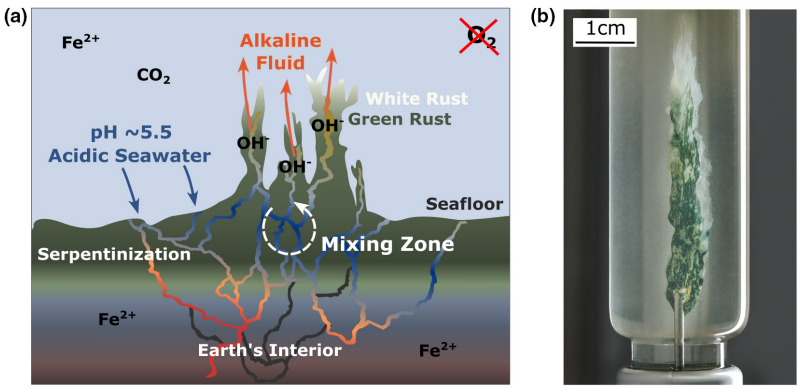

FIGURE 1 Alkaline vents and the emergence of life in a ferruginous environment. (a) Schematic drawing of the seafloor conditions during the ferruginous oceans of the Hadean and Archean. The pH of the seawater was ~5.5. Acidic seawater gets reduced by Fe^{2+}-containing rocks (e.g., olivine) in the Earth's interior, releasing OH^- via serpentinization, fueling the formation of alkaline vents. (b) White and green rust chimney formed in a 20 mL vial through the mixing of an alkaline fluid with a ferruginous solution. Injection rate: 5 mL/h.

values were continuously monitored inside the anaerobic chamber using two digital sensors. They were constantly below <0.01% of present atmospheric levels. Experiments were carried out at room temperature (25°C) as it seems likely that low-temperature systems were widespread in off-axis environments.

Our experimental setup was similar to those used in previous studies where an alkaline solution representing the hydrothermal fluid is slowly pumped into a ferruginous solution representing the ocean (Barge et al., 2015, 2020; Burcar et al., 2015; White et al., 2015; Figure S1). We used an inverted 125 mL glass vial with the bottom cut off to hold the ferruginous solution. The vial was sealed with a rubber stopper (Figure S1) and a pipette tip was inserted through the crimp-seal and connected to a polymer tube on the outside (bottom) of the inverted flask, which was connected to a syringe 10 mL Luer-lock plastic syringe (B Braun) filled with alkaline NaOH (Carl Roth) solution. The polymer tubing was connected to the syringe via a Sterican® hypodermic-needle (B Braun, 1.20×50 mm, 18 G×2). The syringe was mounted on a single-syringe pump (Cole Parmer, Model 100 78-9100C), that was vertically oriented to ensure a constant flow rate of alkaline fluid from the syringe into the simulated iron ocean. Horizontal orientation of the syringe and syringe pump was found to result in less stable chimneys, because the required longer tubing length caused introduction of gas bubbles that disrupted chimney growth. Vertical orientation of the syringe and syringe pump, and the shorter tubing length greatly ameliorated this problem.

A 100 mL solution with 0.2 M $FeCl_2{}^*4H_2O$ (Sigma-Aldrich) and MilliQ water resulted in ferruginous and acidic (pH 3) conditions. The alkaline (pH 13) hydrothermal solution consisted of 0.2 M NaOH (Carl Roth) dissolved in MilliQ water. All solutions were prepared inside the anaerobic chamber to ensure anoxic conditions and reduce the presence of dissolved O_2 in the solutions. The alkaline NaOH solution was injected into the ferruginous solution at a rate of 3.7 mL/h. The pH of the ferruginous solution was monitored over the duration of the experiment using a pH meter. After ~2 h and injection of 7 mL NaOH, chimney growth ceased. A total of 12 mg dry-powdered total RNA from the yeast *Saccharomyces cerevisiae* (Sigma-Aldrich, catalog number 10109223001) was dissolved in the ferruginous solution (before the injection started) to achieve a mean starting concentration (+/− standard error of the mean) at $t(_0)$ of (3.96 +/− 0.54) ng/μL in all five experimental replicates (Table S1). The powder was weighed using a high sensitivity scale with an analytical variation of ±1 mg. The starting concentration of RNA slightly varied because of the uneven dissolution of the RNA powder.

2.2 | RNA sampling, extraction and quantification

Inside the anaerobic chamber, 1 mL samples of the ferruginous solution were taken with a pipettor at set time intervals as the chimney grew. At the end of the experiment, the chimney was dried in the anaerobic chamber for 24 h and frozen for subsequent RNA extraction (see below). All RNA extractions from the ferruginous solution and the green rust chimneys were performed in a laminar flow clean bench equipped with a high-efficiency particulate air filter. The clean bench is a dedicated bench for RNA only with its own dedicated set of pipettors, racks and tubes, where no DNA samples or PCR products are introduced (Orsi et al., 2022). This helps to maintain a relatively low level of RNA and DNA contamination from aerosols as well as DNA contamination from PCR products. All surfaces are sterilized with UV prior and after sample processing and all surfaces are wiped down with RNAseZap to remove any potential contaminating microbes or aerosolized RNA.

During the experiment within the anaerobic chamber, the ferruginous solution was sampled at a consistent frequency every 10 min in all five experimental replicates, and additionally every minute in the first 10 min in experimental replicates 3, 4 and 5 (Table S3) to capture a high temporal resolution from the initial period of chimney formation where the most rapid RNA depletion in the ferruginous solution simulant was observed. The liquid samples were immediately transferred to RNA/DNA clean 2 mL Eppendorf tubes that were frozen at −20°C. RNA was extracted by adding 1 mL of acidic (pH: 4) trizol (MP Biomedicals) and 1 M Na_2HPO_4 (Sigma-Aldrich) powder. The addition of the phosphate buffer was used to reduce RNA adsorption to iron particles in the ferruginous solution, which is a well-known feature of iron minerals that can reduce nucleic acid extraction efficiencies (Muto et al., 2017). The solutions were mixed by vortexing for 10 s and centrifuged for 10 min at 4°C (to increase RNA preservation and strengthen the trizol phase separation) at 13,000 rpm. The supernatant (containing the dissolved RNA) was transferred via pipetting to a new 2 mL RNA/DNA free tube. An equal volume of ≥99.5% isopropanol (Carl Roth) and 3 μL glycogen (Carl Roth) as a carrier were added to help precipitate the relatively low concentrations of RNA. Precipitation was done overnight at −20°C. RNA was pelleted by centrifugation (5 min at 4°C, 13,000 rpm). The pellets were air dried in an RNA-dedicated laminar flow hood (see above) with HEPA filtered air to reduce contamination. To remove residual salts, the pellets were washed with 500 μL of 70% molecular biology grade ethanol (Carl Roth) centrifuged for 5 min and air dried in the laminar flow clean hood. After air drying, the RNA pellets were resuspended in RNAse free diethyl pyrocarbonate (DEPC) treated water (Carl Roth) and vortexed for 30 s to resuspend the RNA. Quantification was done with an Invitrogen Qubit 3 Fluorometer and the micro–RNA kit.

After the AHV experiment, the ferruginous solution was drained with a pipette and the chimney was dried out for 1 day inside the anaerobic chamber. The dried chimney was weighed and placed in a sterile RNA free 2 mL screw cap microtube (MP Biomedicals, Lysing Matrix E) containing 0.5 mL of differently sized silica beads. The silica beads were added to the RNA extraction step to physically disrupt the chimney structure during beating in order to enhance RNA retrieval during the extraction. RNA extractions were optimized using 1 mL of acidic (pH: 4) Phenol:Chloroform:Isoamyl alcohol ('trizol'). To desorb the RNA off of the green rust, 1 M Na_2HPO_4 was added since the addition of a phosphate buffer assists in desorbing RNA off of mineral surfaces (Muto et al., 2017). Chimney samples were homogenized in the presence of the acidic trizol and phosphate buffer in the Lysing

Matrix E tubes, using a Fastprep-24 5G (MP Biomedicals) at a speed of 6.0 m/s for 40 s. The samples were centrifuged for 10 min at 4°C and 13,000 rpm and the upper aqueous phase (containing the RNA) was transferred to new 2 mL Eppendorf tubes. The RNA was precipitated by adding an equal volume of isopropanol and 3 μL glycogen each. All samples were frozen overnight at −20°C. Pelleting, washing and measuring the RNA was done as described in the previous paragraph.

2.3 | Raman spectroscopy

The dry green rust chimneys were stored under an N_2 atmosphere to minimize oxidation prior to the analysis with the Raman spectrometer (HORIBA Jobin Yvon XploRA, Mineralogical State Collection Munich). For data acquisition, the chimneys were taken out of the anaerobic chamber. Exposure to air was less than 2 min until the start of the first Raman measurement. After 30 min, the chimney was completely oxidized and no green rust was detectable anymore. The settings of the scans were as follows: spectral range from 50 to 4000 cm^{-1}, 10 s acquisition time, 2 accumulations, 300 μm confocal hole and 100 μm slit, 1800 grooves/mm grating and a filter with 10 to 25% optical density of the incoming laser to avoid laser-induced oxidation of the chimney. A green laser with a wavelength of 532 nm, the ×100 long working distance (LWD) objective (0.80 numerical aperture) were used for all measurements and the Labspec 6 software was used to process the acquired spectra. We used an in-house reference Raman database MSC-RD (Mineralogical State Collection Raman Database, Drozdovskiy et al., 2020), the KnowItAll database (Horiba Edition, now John Wiley & Sons) and the database from the RRUFF™ Project (Lafuente et al., 2015). The instrument was calibrated with a silicon wafer (520.7 cm^{-1}) daily and immediately before the measurements took place.

2.4 | Scanning electron microscopy

We used a Phenom XL G2 scanning electron microscope (SEM) to further characterize the mineralogy of chimneys under vacuum. The dry chimneys were stored under an N_2 atmosphere until measurements started. Air exposure during transfer to the vacuum chamber of the SEM was limited to 30 s maximum. All measurements were carried out using an acceleration voltage of 10 kV, a beam current of 1 μA-pA, a vacuum pressure of 0.10 Pa and a beam diameter of 0.005 to 1 μm. For imaging, secondary electrons (SE) and backscattered electrons (BSE) were used. Elemental analysis of the green rust chimneys was carried out with the electron dispersive X-ray spectroscopy detector (EDX).

2.5 | Imaging, processing, quantifying chimney growth

Images of chimneys were taken with a Sony Alpha a6000 mirrorless camera and a 90 mm Sony macro lens. The images were processed using the Adobe Lightroom and Photoshop software packages and the height of the chimney was determined in Adobe Photoshop with a ruler. Timelapse videos were taken with the Sony Alpha a6000 as well. The camera took an image of the chimney every 1–2 s during growth. The raw timelapse videos from the camera were sped up x20 times in post-production.

3 | RESULTS

3.1 | Chimney morphology

Five different AHV experiments were carried out in an anaerobic chamber in a N_2 atmosphere. During chimney growth, the pH was constantly monitored and it remained at pH 3 for the entire duration of the experiment. In all five experimental replicates, the injection of the alkaline fluid resulted in the formation of chimney structures within 90 min. These structures resemble "chemical gardens" that have been found to form in AHV models across steep pH gradients (Altair et al., 2021). The average height of the chimneys (+/− standard error of mean) was (3.7 +/− 0.2) cm. The average width was (0.6 +/− 0.2) cm. The fastest growth rates were observed in the first 10 min of the five experimental replicates (Figure 3b). The raw RNA data for all five experiments is displayed in Table S1. After the initial growth phase, which ended after 10 min, vertical chimney growth slowed down significantly, after which horizontal growth of small mm-sized branches was observed. No more vertical growth was noted after 90 min. Growth of additional chimney extensions was detected only in two out of five experiments after 90 min of chimney growth.

A reproducible color transition pattern was observed during all experiments, whereby the base of the chimney would change from being translucent or white color to a green color in 5 min only. Then, as the chimneys grew, the green color gradually moved upwards towards the top replacing the white color by the end of the experiment. After a few minutes, the surface of the green precipitate would break and a new chimney structure would grow vertically on top of the green structure (Videos S1–S3). These new structures also appeared first as a white film, which turned green also within 4 to 5 min of exposure to the ferruginous solution. This process of constant ruptures, re-precipitation and color transition continued, until the chimneys reached their maximum heights. A visualization of the phase transition from the white film to green colored chimney structure is presented in Figure 3e and in Videos S1–S3.

3.2 | Green rust identification

The fully grown chimney shows a complex morphology on a macroscopic and a microscopic scale. SEM images show that the chimney is composed of a thin inorganic 'membrane' of euhedral hexagonal plate-shaped crystals (Figure 2a) that are similar in size

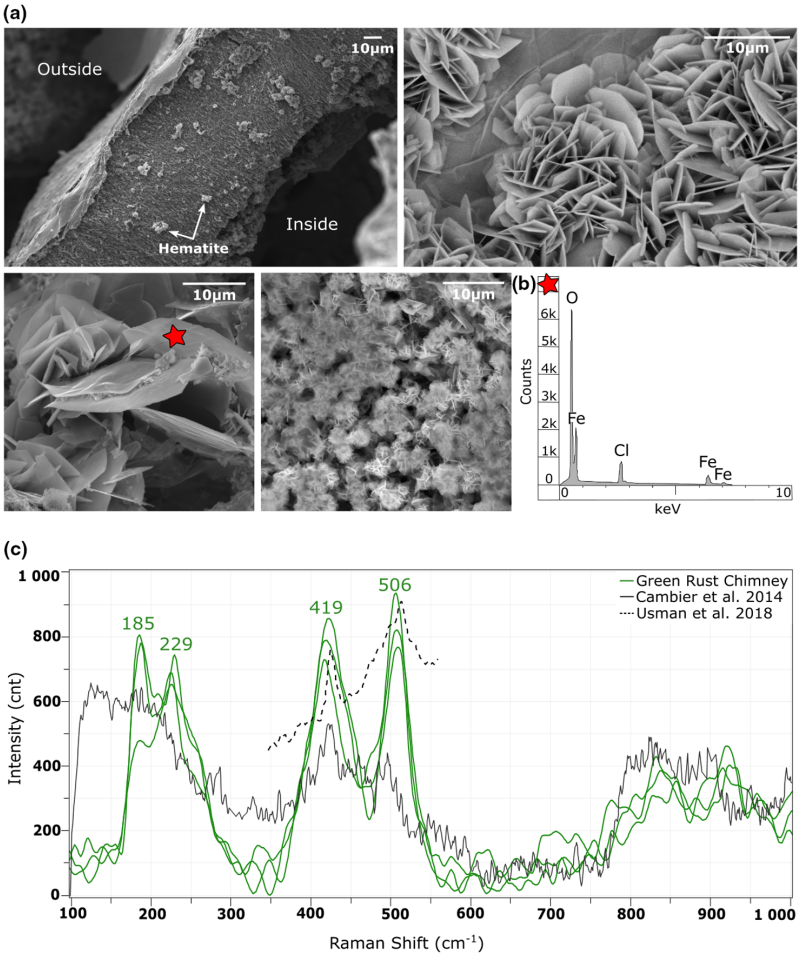

FIGURE 2 Dried chimney structures are composed primarily of green rust. (a) BSE images of a dried green rust chimney. The first image shows a chimney wall with a thickness of approx. 80 to 90 µm. Hematite globules are located on top of the green rust. The other BSE images show different magnifications of hexagonal platy green rust crystals. Contamination with oxygen during the transfer to the vacuum chamber was limited to max. 1 min transfer time. (b) EDX spectrum with the elemental composition of the chimney in the marked region (red star). Acquisition settings were 30 s time, 10 kV acceleration voltage and 0.10 Pa vacuum pressure. (c) Raman spectra of a green rust chimney made with 0.2 M NaOH and 0.2 M $FeCl_2$*$4H_2O$. The significant Raman bands for green rust identification are at 427 and 518 cm^{-1} (Usman et al., 2018). Other mineral peaks except green rust peaks were removed from the Cambier et al. (2014) spectrum for simplification.

and shape to green rust (Duval et al., 2019; Usman et al., 2018). Crystals formed aggregates, with individual crystals ranging in diameter from <1 µm to approximately 20 µm. The chimneys contain an inorganic membrane with a width between 80 to 90 µm (Figure 2a). SEM images also revealed a high internal pore space and surface area with nanopores (<1 µm) and channels in the chimney structure (Figure 2a).

Raman spectra of a dried chimney suggests that it is mainly composed of green rust (Figure 2c). This evidence is based on the characteristic Raman bands at 427 and 518 cm^{-1}, that are considered diagnostic for green rust identification (Trolard et al., 2007; Usman et al., 2018). The EDX spectrum highlights the elemental composition of the chimneys, which is consistent with chloride-bearing green rust (Figure 2b). Chloride green rust has a chemical composition of ~$[Fe_3^{2+}Fe^{3+}(OH)_8]^+[Cl{\cdot}2H_2O]^-$ (Arrhenius, 2003; Barge et al., 2015; Russell et al., 2013). When left exposed to air for more than 20 min, the chimneys changed color quickly from dark green to an ochre color indicating oxidation of iron. Based on SEM and Raman analyses, these oxidation products were identified as hematite (Figure 2a; Figure S2).

3.3 | RNA depletion from the ferruginous solution during chimney growth

A rapid decrease of RNA in the ferruginous solution was observed primarily during initial stages of chimney growth in all five experimental replicates (Figure 3b). RNA starting concentrations ranged from 1.99 to 5.27 ng/µL, because the powder containing the yeast RNA did not dissolve completely. We presume the powder might contain additional water insoluble components (for example lipids) to RNA that are unknown and not listed by the manufacturer. Nevertheless, the standard error (0.54) of the average starting concentration of 3.96 ng/µL is only 14% (Table S1). No matter the starting concentration, the same depletion trend was observed across all five experimental replicates. Figure 3d highlights the first 10 min of RNA depletion in experimental replicates 3, 4 and 5 (error bars show standard error of the means). RNA concentration values are listed in the Table S3. Figure 3d shows that the fastest RNA depletion rate in solution takes place in the first 4 min from an average of 4.82 ± 0.30 ng/µL of RNA to 1.02 ± 0.32 ng/µL of RNA, which coincides with the white rust phase of the chimney. In this time,

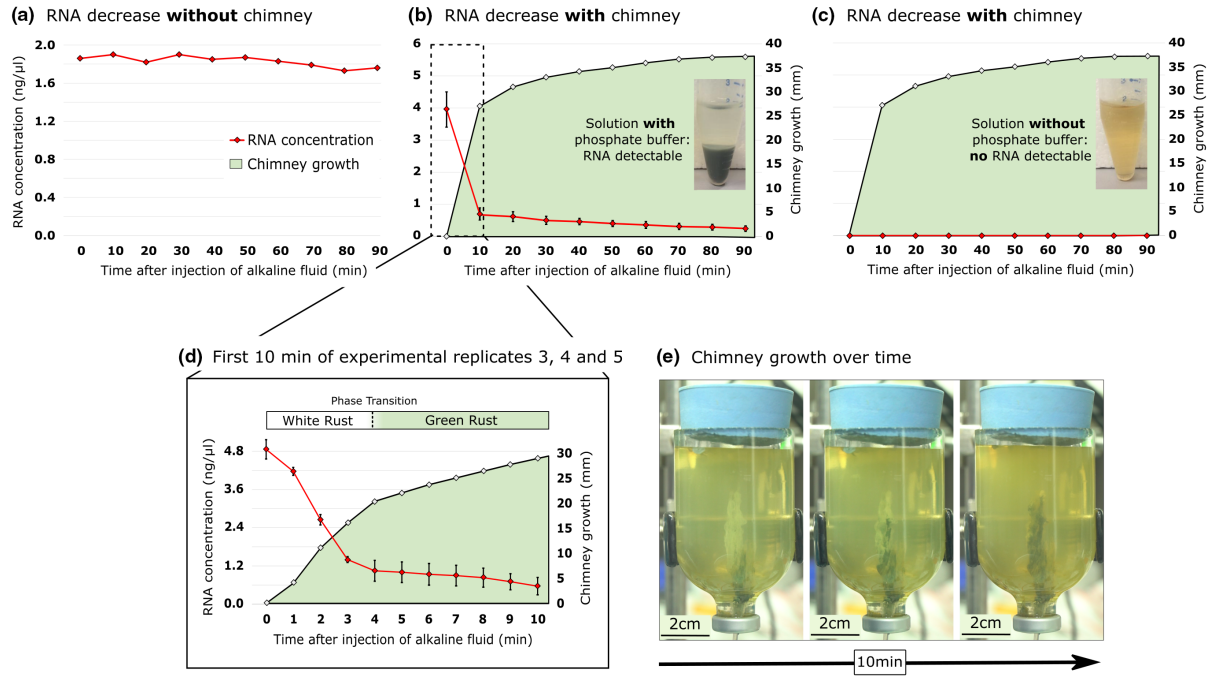

FIGURE 3 RNA is depleted from the ferruginous solution only in the presence of chimneys. RNA extractions were performed by adding a phosphate buffer (1 M Na_2HPO_4) to desorb the RNA from the iron in the solution. (a) Rate of RNA depletion in the ferruginous solution without a chimney (control experiment). (b) Rate of RNA depletion from the solution with a chimney. Error bars show the standard error of the mean across five experimental replicates. RNA extractions were performed with a phosphate buffer, which precipitated together with the iron at the bottom of the sample tubes. The RNA remained in solution. (c) RNA extractions without a phosphate buffer. The same five samples as in (b) were used. Without phosphates, no RNA was extractable because the RNA was still bound to the iron in solution. This highlights the positive effect of adding phosphate to the RNA extraction protocol. (d) First 10 min of experimental replicates 3, 4 and 5. Error bars show the standard error of the mean. (e) White $Fe(OH)_2$ oxidation to green rust in contact with the ferruginous solution. RNA concentration values in Tables S1 and S3.

the three replicate chimneys show an average growth from 0 to 22.33 mm. After 4 min, RNA depletion rates slowed down significantly and the concentrations only dropped from 1.02 ± 0.32 ng/µL to 0.54 ± 0.27 ng/µL. This second phase of slower RNA depletion correlates with green rust formation (Figure 3d).

To confirm, that the measured RNA in the solution is not from contamination, a control experiment was performed as described, but no *Saccharomyces cerevisiae* RNA was added. The results reveal that RNA concentrations at $t(_0)$ and $t(_{end})$ in the solution and in the chimney were all below the detection limit of the Qubit Fluorometer (Table S1). This provides evidence, that all detected RNA in the five experimental replicates was from *Saccharomyces cerevisiae*.

Another control experiment with *Saccharomyces cerevisiae* RNA but no chimney confirmed that the RNA depletion in the solution was not due to degradation, but due to chimney growth (Figure 3a). The rate of natural RNA degradation without a chimney was relatively slow and only decreased <10% over the course of the experiment. In contrast, with a chimney, the RNA was depleted ≥99% and was below the detection limit of the Qubit Fluorometer by the end of the experiment (Figure 3b).

No RNA could be extracted from the ferruginous solution without the addition of a phosphate (1 M Na_2HPO_4) buffer (Figure 3c), indicating that the dissolved RNA is likely adsorbed onto iron particles in the solution as described previously (Muto et al., 2017).

3.4 | RNA accumulation in chimneys

When a chimney was present, RNA concentrations decreased 1000-fold in the ferruginous solution compared to the starting concentration (Figure 4a). This contrasts with conditions of a control experiment, where no alkaline fluid was injected, hence no chimney was formed. Here, only a minor decrease in RNA concentration in the iron solution was observed (Figure 3a). At the end of the experiments with a green rust chimney, the concentration of RNA in the chimney (765 ± 79 ng per gram) was significantly higher (two-sided *t*-test: $p = 0.000031$) than the concentration of RNA in the solution at the end of the experiment (20 ± 4 ng per gram) (Figure 4a; Table S2). Without a phosphate extraction buffer, no RNA was extractable from the chimney samples. This indicates that the RNA was complexed with the iron in the chimney, a well-known feature of iron-containing minerals (and clay minerals in general) that bind nucleic acids and reduce their extractability (Muto et al., 2017).

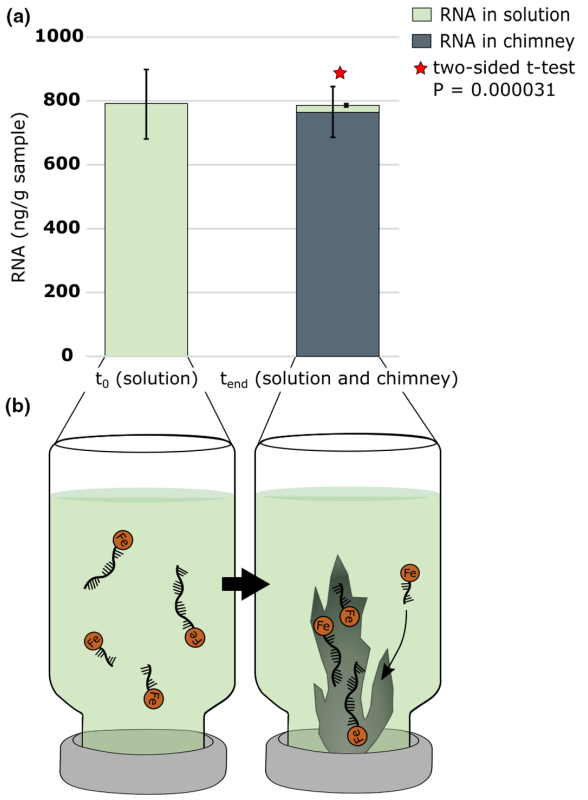

FIGURE 4 Accumulation of RNA in the white and green rust chimneys. (a) Bar charts show the average of RNA in ng/g in the ferruginous solution at the beginning (t_0) and the end (t_{end}) of five experimental replicates (green bar charts). The grey bar chart shows the mean RNA from five different chimneys. RNA data listed in Table S2. Error bars represent standard error of the means. The two-sided *t*-test was significant with $p = 0.000031$. (b) Schematic drawing of Fe-RNA complexes in the solution getting incorporated into the chimney while it grows. At $t(_{end})$, almost no RNA was detected in the solution, as it was mainly detected in the chimney (a).

4 | DISCUSSION

4.1 | Experimental geochemical conditions in the context of predictions for early Earth

We tested key geochemical aspects of the prebiotic ocean on early Earth, anoxic and ferruginous conditions. It is widely accepted that these seawater conditions were characteristic of the Hadean and Archean (Poulton & Canfield, 2011). Our alkaline vent experiments are based on the prediction, that widespread serpentinization of the oceanic lithosphere was common in prebiotic oceans (Camprubí et al., 2019; Russell, 2018). This probably resulted in venting of high pH fluids at the seafloor, forming alkaline springs when the alkaline fluids came in contact with the ferruginous ocean. We chose pH 3 for the ferruginous solution and pH 13 for the alkaline fluid, since these conditions facilitated repeatable chimney growth structures and did not impact the overall results.

Our experiments were carried out at 25°C room temperature, which seems justified considering that temperature estimates of the prebiotic ocean are highly uncertain (Altair et al., 2021; Camprubí et al., 2019), ranging from boiling to freezing conditions (Kasting & Ackerman, 1986). Hydrothermal activity can proceed over an even broader range from <10°C to about 407°C (German et al., 2008). Thus, our ambient experimental conditions represent a relatively cool off-ridge environment. We also show that hydrothermal conditions with elevated temperatures are not necessarily required for the formation of green rust chimneys in a ferruginous solution. Relatively mild temperatures are not out of the question in terms of prebiotic ocean conditions, since recent models predict temperatures for some regions of the prebiotic ocean down to as low as 0 to 50°C (Krissansen-Totton et al., 2018). The fact that our green rust chimneys form at 25°C is also beneficial to RNA stability compared to elevated temperatures (Jo et al., 2022).

We were not able to simulate high pressures in the anaerobic chamber. Thus, all experiments were performed at atmospheric pressure, which is relatively low and not representative of the deep sea, where many hydrothermal vents are found (Baker & German, 2004). However, shallow water alkaline vents might have been located near oceanic islands, island arcs or continental shelves, if they existed in the Hadean and Archean, which is highly debatable (Arndt & Nisbet, 2012). Nonetheless, many of the earliest fossils known today are located in shallow water settings, like the 3.4 Ga Strelley Pool Formation in the Pilbara Craton of Western Australia (Sugitani et al., 2015). Moreover, modern examples of such shallow serpentinite-hosted vents today are the Strytan Hydrothermal Field in Iceland or the Prony Hydrothermal Field in New Caledonia (Quéméneur et al., 2014), showing the possibility of hosting complex biological communities. In conclusion, water depth and pressure mimicked in our experiments could represent shallow water vents (Barge & Price, 2022), that hold some of the earliest signs of life in the fossil record according to Sugitani et al. (2015), but the results need to be reviewed with caution. The recent study by Barge and Price (2022) mentions the growing importance of shallow-sea alkaline hydrothermal vents and their possibility to facilitate life-forming reactions.

4.2 | Assessing oxidation of the chimneys

It is known that green rust oxidizes quite fast upon air exposure (Usman et al., 2018). Therefore, we carefully assessed the possibility for oxidation in our experiments. Oxygen exposure during the alkaline vent experiments ($O_2 < 0.01\%$ of present atmospheric values) and sample transfer (transport in N_2 purged gas tight flasks) was kept at a minimum. We acknowledge, that some oxidation might have occurred during the transfer of the chimneys to the microscope. The SEM and elemental analysis indicate effects of oxidation to be minor and resulted in small hematite globules (<10 μm in size) that are likely

the first signs of oxidation (Figure 2a). This likely has to do with SEM measurements being made in a vacuum chamber with no air, and the sample being exposed to air for only a few seconds during transfer. However, when the sample was scanned with the Raman it was not in a vacuum and showed strong signs of oxidation after 20 min where the entire chimney had been oxidized to hematite (Figure S2). When the green rust chimney was measured with the Raman within 1 or 2 min, the characteristic Raman bands at 419 and 506 cm^{-1} for green rust (Usman et al., 2018) were observed (Figure 2c). Therefore, our results indicate that we are forming green rust in the anaerobic chamber that quickly oxidizes to hematite under the Raman. However, it is possible to obtain the green rust spectra with the Raman when measuring quickly after transfer from the gas tight anoxic flask. As expected, the oxidation in air changes the green rust to hematite relatively quickly.

4.3 | Mineralogy and morphology of the chimneys

Evidence for injection-growth experiments under ferruginous conditions forming white and green rust, is scarce. For this reason, we simulated iron hydroxide chimneys in an anaerobic chamber. The first white phase that precipitates in our alkaline vent experiments is probably $Fe(OH)_2$ sometimes referred to as amakinite (Trolard et al., 2022). It shows the typical white color for ferrous iron hydroxide (Lutz et al., 1994) and turns green when it comes in contact with the ferruginous solution in less than 5 min (Figure 3e), indicating oxidation and green rust formation (Barge et al., 2015; Trolard et al., 2007). Difficulties arose, when we attempted to investigate the white rust phase, because of its quick transformation into green rust during the AHV experiment and the lacking ability to dry this highly metastable phase in order to microscopically analyze it. A pure white rust chimney collapses immediately when we attempted to remove the ferruginous solution with a syringe. It was only after the phase transition to green rust that the chimney increases in stability and the solution can be removed with no problem. Similarities in other studies point to this first precipitated phase being ferrous hydroxide $Fe(OH)_2$. Stone et al. (2005) also performed chemical garden chimney growth experiments across pH gradients in ferruginous solutions, and identified the oxidized precipitate of iron in aqueous solutions as ferrous hydroxide $Fe(OH)_2$, namely "white rust". Trolard et al. (2022) describe the precipitation of ferrous hydroxide after mixing a Fe(II) salt solution with sodium hydroxide. Barge et al. (2015) identify the first precipitates in a green rust forming experiment as white rust (iron hydroxide) as well. White rust forms by oxidation and partial hydrolysis of dissolved Fe^{2+} (Trolard et al., 2007), which is the process described in our experiments.

Green rust showed a higher stability than white rust under anoxic conditions, which allowed us to dry the chimneys and prepare them for measurements. Since $FeCl_2{}^*4H_2O$ was used as a salt for the ferruginous solution, chloride-containing green rust GR1-Cl was formed out of the precursor phase white rust (Duval et al., 2019; Trolard et al., 2022). Depending on the intercalated anion in the double layer hydroxide structure, different varieties of green rust are possible, Cl^-, $CO_3{}^{2-}$ or $SO_4{}^{2-}$ green rust for example (Russell, 2018; Trolard et al., 2007). The hexagonal and tabular morphologies of the crystals (Figure 2a) are a typical indicator for green rust as well (Duval et al., 2019; Trolard et al., 2007; Usman et al., 2018). Our chimneys show very similar Raman bands to Usman et al. (2018) and Cambier et al. (2014) that are albeit slightly shifted to 419 and 506 cm^{-1} (Figure 2c).

Chimney morphologies like ours (but with varying chemistries) have been formed in different AHV experiments in the past (Barge et al., 2015, 2020; Burcar et al., 2015; White et al., 2015). The spontaneously formed chemical gardens are made out of vertically oriented chimneys with high internal surface areas that act as flow-through chemical reactors composed of inorganic membranes (Barge et al., 2020). The mainly vertical formation of the chimney structures might be due to fluid buoyancy effects, suggesting the injected sodium hydroxide was less dense than the iron-rich solution (Barge et al., 2012). Experiments performed in microgravity showed no preferred chimney growth orientation (Barge et al., 2012). The injection of 7 mL 0.2 M NaOH with pH 13 had no measurable effect on the pH of the ferruginous solution, which was at pH 3 for the entire duration of the experiment. This could either indicate that the OH^- was being consumed completely by the green rust chimney structure as it grew over time, or the amount of NaOH pumped into the ferruginous solution was simply too small to overcome its buffering capacity.

4.4 | An alternative RNA concentration mechanism compared to wet-dry cycles based on RNA-iron complexation

Generally, adsorption of RNA onto mineral surfaces is a known process particularly in the emergence of life context (Altair et al., 2021; Biondi et al., 2017; Cleaves II et al., 2011; Mizuuchi et al., 2019; Muto et al., 2017; Pedreira-Segade et al., 2016). Especially phyllosilicates are known to adsorb nucleotides, like Fe-Mg-rich swelling clays (Pedreira-Segade et al., 2016). The observation that divalent cations like Mg^{2+} or Fe^{2+} stabilize nucleotides better than monovalent cations (Bowman et al., 2012), supports the importance of the iron-rich mineral green rust. Furthermore, Fe^{2+} can replace Mg^{2+} as the dominant divalent cation during key catalytic RNA functions (Athavale et al., 2012; Bray et al., 2018), indicating that Fe^{2+} was a potential important chelator of RNA in the ferruginous prebiotic oceans.

A fundamental question addressed in our AHV study is the mechanism of RNA sequestration into the chimney. Our results show that RNA is already complexed with Fe^{2+} in the ferruginous solution and that it is concentrated in the chimney as it grows over time (Figure 4b). The iron in solution facilitates the sequestration of RNA into the mineral structure as the chimney precipitates out of solution across the pH gradient. This is evident, because no RNA

was extractable from the ferruginous solution without a phosphate buffer (Figure 3c), showing that the RNA is complexed to iron in the solution.

Wet-dry cycles in warm little ponds are often invoked as possible concentration sites for nucleic acids on an early Earth's surface (Damer & Deamer, 2020; Darwin, 1871; Pearce et al., 2017) that can lead to polymerization (Pearce et al., 2017). Our findings offer an additional plausible concentration mechanism of RNA that does not depend on wet-dry cycles. This is facilitated instead by white and green rust low-temperature alkaline vents. To our knowledge, this is also the first experimental evidence that RNA-iron complexation facilitates the concentration of RNA in an AHV. This opens up the possibility that RNA oligo- and/or polymerization could also occur in AHVs under these conditions.

4.5 | RNA accumulation dynamics in the green rust chimney

RNA accumulation inside the chimney could either be correlated to the height of the chimney, where the amount of RNA in solution decreases as the chimney grows, or the phase transition of white to green rust. RNA seems to bind faster to the initial white rust phase in the first 4 min compared to green rust that forms several minutes later (Videos S1 and S2). The first 10 min of the experimental replicates 3, 4 and 5 reveal, that the highest depletion of RNA in solution takes place in the first 4 min, where the average RNA concentration drops from 4.82 ± 0.30 to 1.02 ± 0.32 ng/μL (Figure 3d). In this period, the chimney growth rate is also the fastest.

In the control experiment without a chimney, the natural RNA degradation (Figure 3a) was minimal, which does not explain the depletion of RNA in the ferruginous solution in the presence of a chimney. Instead, the RNA gets depleted rapidly if a chimney is present (Figure 3b). Thus, the white and green rust chimneys offer a favorable and highly reactive location for the RNA to accumulate. This is evident, when considering that at the end of the experiments higher concentrations of RNA were extracted from the dried green rust chimney compared to the surrounding solution at $t_{(end)}$. Therefore, the RNA is likely moving from the ferruginous solution into the chimney over time and as it grows. The mean of recovered total RNA at $t_{(0)}$ and $t_{(end)}$ is highly similar, showing that there appears to be a mass balance between the RNA concentration at $t_{(0)}$ in the solution and at $t_{(end)}$ in the chimney (Figure 4a).

The variability in RNA concentrations between experiments is likely due to several other factors that introduce variability into the setup such as (1) variation in the chimney growth rate, (2) variation in chimney morphologies, (3) variation in the oxygen concentration in the chamber between 20 and 100 ppm which affects the rate and amount of green rust that forms, and (4) variable amounts of chimney material often get lost to solution in fluid jets or during sample transfer. Nevertheless, the variation is relatively low, indicating that our results are reproducible (Figure 3b; Table S1).

4.6 | Implications for RNA world theories

The RNA world receives strong support from the discovery that all proteins in living organisms are synthesized by a ribozyme at the center of the ribosome (Cech, 2000). Ribozymes, which are enzymes, whose catalytic centers are entirely made of RNA (Scott, 2007), may be the next higher functional building block on the way to a living organism. Ribozymes, which can cleave, join and replicate, are key components for protein synthesis, since they are part of the ribosomes of cellular organisms (Moelling & Broecker, 2021). Thus, it is believed that ribozymes preceded DNA and proteins during evolution (Moelling & Broecker, 2021). Successful trapping and accumulation of ribozymes at iron hydroxide chimneys in future experiments would not only underline the hypothesis of white rust and green rust as important minerals, but of AHVs in general during the emergence of life. Furthermore, Athavale et al. (2012) highlight the importance of the presence of Fe^{2+} over Mg^{2+} in prebiotic oceans, and how Fe^{2+} enhances the catalytic activities of ribozymes.

We acknowledge, that because our tested RNA came from yeast, it is not an ideal proxy for ribozymes. Because the RNA is derived from a living organism (yeast), our experimental setup is not immediately comparable to a possible RNA world that might have consisted of prebiotic self-replicating RNAs. Our experimental setup is similar to that used by McGlynn et al. (2012) who also used RNA from yeast to test hypotheses surrounding the influence of iron sulfide and iron hydroxide minerals on RNA-complexation and binding dynamics in hydrothermal chimney structures (McGlynn et al., 2012). Using a similar logic, we used yeast RNA as a simplification to study how RNA accumulation can occur in white and green rust chimneys forming under simulated geochemical conditions of the early Earth (ferruginous, anoxic). Despite deriving from a living organism, the yeast RNA shares many biochemical and biophysical properties with ribozymes. For example, yeast RNA and ribozymes should both represent soluble charged biomolecules that would promote binding iron minerals like green rust. However, the shorter strand length of ribozymes and potentially different or lower nucleotide diversity of the ribozymes could affect binding to the white rust and green rust, which should be a focus of future studies to see if the same concentration dynamics seen here for yeast RNA also applies to ribozymes.

5 | OUTLOOK

The mineral green rust has been proposed as one of the key minerals in life's emergence, which underlines the significance of our results that white to green rust transforming chimneys accumulate RNA from a ferruginous solution. No rocks exist on the Earth that are older than 4 Ga, but our experiments indicate that green rust chimneys may have been a feature of the early Earth seafloor at alkaline springs under ferruginous conditions. RNA concentrating

mechanisms may have promoted survival of self-replicating RNAs, that otherwise would be diluted to extremely low concentrations in the early ferruginous oceans during the Hadean and Archaean. In contrast to alkaline vents, wet-dry cycles in warm little ponds are a potential place for concentrating biomolecules at life's emergence. Our study shows that white and green rust composed chimneys accumulate RNA from a ferruginous solution, thereby providing an additional potential mechanism to help solve the "concentration problem" (De Duve, 1991) for RNA in a prebiotic ocean.

ACKNOWLEDGMENTS

We thank Dr. Dan Mills for valuable feedback on geobiological interpretations of the experiments. We acknowledge Ninos Hermis for assistance with preliminary experimental setups. Open Access funding enabled and organized by Projekt DEAL.

FUNDING INFORMATION

This work was supported by the Deutsche Forschungsgemeinschaft (DFG, German Research Foundation)—Project-ID 364653263—TRR 235 to WDO and DB, and under Germany's Excellence Strategy—EXC 2077-390741603.

CONFLICT OF INTEREST STATEMENT

The authors declare no conflict of interest.

DATA AVAILABILITY STATEMENT

The data that supports the findings of this study are available in the supplementary material of this article.

ORCID

Vanessa Helmbrecht https://orcid.org/0000-0002-7537-3798

REFERENCES

Altair, T., Borges, L. G., Galante, D., & Varela, H. (2021). Experimental approaches for testing the hypothesis of the emergence of life at submarine alkaline vents. *Life*, *11*(8), 777.

Arndt, N. T., & Nisbet, E. G. (2012). Processes on the young earth and the habitats of early life. *Annual Review of Earth and Planetary Sciences*, *40*(521), 2012–2549.

Arrhenius, G. O. (2003). Crystals and life. *Helvetica Chimica Acta*, *86*, 1569–1586.

Athavale, S. S., Petrov, A. S., Hsiao, C., Watkins, D., Prickett, C. D., Gossett, J. J., Lie, L., Bowman, J. C., O'Neill, E., Bernier, C. R., Hud, N. V., Wartell, R. M., Harvey, S. C., & Williams, L. D. (2012). RNA folding and catalysis mediated by iron (II). *PLoS One*, *7*(5), e38024.

Baaske, P., Weinert, F. M., Duhr, S., Lemke, K. H., Russell, M. J., & Braun, D. (2007). Extreme accumulation of nucleotides in simulated hydrothermal pore systems. *Proceedings of the National Academy of Sciences of the United States of America*, *104*(22), 9346–9351.

Baker, E. T., & German, C. R. (2004). On the global distribution of hydrothermal vent fields. Mid-Ocean ridges: Hydrothermal interactions between the lithosphere and oceans. *Geophysical Monograph Series*, *148*, 245–266.

Barge, L. M., Cardoso, S. S., Cartwright, J. H., Cooper, G. J., Cronin, L., De Wit, A., Doloboff, I. J., Escribano, B., Goldstein, R. E., Haudin, F., Jones, D. E. H., Mackay, A. L., Maselko, J., Pagano, J. J., Pantaleone, J., Russell, M. J., Sainz-Díaz, C. I., Steinbock, O., Stone, D. A., … Thomas, N. L. (2015). From chemical gardens to chemobrionics. *Chemical Reviews*, *115*(16), 8652–8703.

Barge, L. M., Doloboff, I. J., White, L. M., Stucky, G. D., Russell, M. J., & Kanik, I. (2012). Characterization of iron–phosphate–silicate chemical garden structures. *Langmuir*, *28*(8), 3714–3721.

Barge, L. M., Jones, J. P., Pagano, J. J., Martinez, E., & Bescup, J. (2020). Three-dimensional analysis of a simulated prebiotic hydrothermal chimney. *ACS Earth and Space Chemistry*, *4*(9), 1663–1669.

Barge, L. M., & Price, R. E. (2022). Diverse geochemical conditions for prebiotic chemistry in shallow-sea alkaline hydrothermal vents. *Nature Geoscience*, *15*, 1–6.

Beard, J. S., Frost, B. R., Fryer, P., McCaig, A., Searle, R., Ildefonse, B., Zinin, P., & Sharma, S. K. (2009). Onset and progression of serpentinization and magnetite formation in olivine-rich troctolite from IODP hole U1309D. *Journal of Petrology*, *50*(3), 387–403.

Bernal, J. D., Dasgupta, D. T., & Mackay, A. L. (1959). The oxides and hydroxides of iron and their structural interrelationships. *Clay Minerals Bulletin*, *4*, 15–30.

Biondi, E., Furukawa, Y., Kawai, J., & Benner, S. A. (2017). Adsorption of RNA on mineral surfaces and mineral precipitates. *Beilstein Journal of Organic Chemistry*, *13*(1), 393–404.

Bowman, J. C., Lenz, T. K., Hud, N. V., & Williams, L. D. (2012). Cations in charge: Magnesium ions in RNA folding and catalysis. *Current Opinion in Structural Biology*, *22*, 262–272.

Bray, M. S., Lenz, T. K., Haynes, J. W., Bowman, J. C., Petrov, A. S., Reddi, A. R., Hud, N. V., Williams, L. D., & Glass, J. B. (2018). Multiple prebiotic metals mediate translation. *PNAS*, *115*(48), 12164–12169.

Burcar, B. T., Barge, L. M., Trail, D., Watson, E. B., Russell, M. J., & McGown, L. B. (2015). RNA oligomerization in laboratory analogues of alkaline hydrothermal vent systems. *Astrobiology*, *15*(7), 509–522.

Cambier, S. M., Verreault, D., & Frankel, G. S. (2014). Raman investigation of anodic undermining of coated steel during environmental exposure. *Corrosion*, *70*(12), 1219–1229.

Camprubí, E., De Leeuw, J. W., House, C. H., Raulin, F., Russell, M. J., Spang, A., Tirumalai, M. R., & Westall, F. (2019). The emergence of life. *Space Science Reviews*, *215*(8), 1–53.

Cech, T. R. (2000). The ribosome is a ribozyme. *Science*, *289*(5481), 878–879.

Charlou, J. L., Fouquet, Y., Bougault, H., Donval, J. P., Etoubleau, J., Jean-Baptiste, P., Dapoigny, A., Appriou, P., & Rona, P. A. (1998). Intense CH4 plumes generated by serpentinization of ultramafic rocks at the intersection of the 15° 20′ N fracture zone and the mid-Atlantic ridge. *Geochimica et Cosmochimica Acta*, *62*(13), 2323–2333.

Cleaves, H. J., II, Crapster-Pregont, E., Jonsson, C. M., Jonsson, C. L., Sverjensky, D. A., & Hazen, R. A. (2011). The adsorption of short single-stranded DNA oligomers to mineral surfaces. *Chemosphere*, *83*(11), 1560–1567.

Damer, B., & Deamer, D. (2020). The hot spring hypothesis for an origin of life. *Astrobiology*, *20*(4), 429–452.

Darwin, C. (1871). Darwin correspondence project, "Letter No. 7471".

De Duve, C. (1991). *Blueprint for a cell: The nature and origin of life*.

Drozdovskiy, I., Ligeza, G., Jahoda, P., Franke, M., Lennert, P., Vodnik, P., Payler, S. J., Kaliwoda, M., Pozzobon, R., Massironi, M., Turchi, L., Bessone, L., & Sauro, F. (2020). The PANGAEA mineralogical database. *Data in Brief*, *31*, 105985.

Duval, S., Baymann, F., Schoepp-Cothenet, B., Trolard, F., Bourrié, G., Grauby, O., Branscomb, E., Russell, M. J., & Nitschke, W. (2019). Fougerite: The not so simple progenitor of the first cells. *Interface Focus*, *9*(6), 20190063.

German, C. R., Bennett, S. A., Connelly, D. P., Evans, A. J., Murton, B. J., Parson, L. M., Prien, R. D., Ramirez-Llodra, E., Jakuba, M., Shank,

T. M., Yoerger, D. R., Baker, E. T., Walker, S. L., & Nakamura, K. (2008). Hydrothermal activity on the southern mid-Atlantic ridge: Tectonically-and volcanically-controlled venting at 4–5 S. *Earth and Planetary Science Letters*, *273*(3–4), 332–344.

Gilbert, W. (1986). Origin of life: The RNA world. *Nature*, *319*(6055), 618.

Halevy, I., Alesker, M., Schuster, E. M., Popovitz-Biro, R., & Feldman, Y. (2017). A key role for green rust in the Precambrian oceans and the genesis of iron formations. *Nature Geoscience*, *10*(2), 135–139.

Heller, R., Duda, J. P., Winkler, M., Reitner, J., & Gizon, L. (2021). Habitability of the early earth: Liquid water under a faint young sun facilitated by strong tidal heating due to a closer moon. *PalZ*, *95*, 1–13.

Jo, T., Tsuri, K., Hirohara, T., & Yamanaka, H. (2022). Warm temperature and alkaline conditions accelerate environmental RNA degradation. *Environmental DNA*, 1–13. https://doi.org/10.1002/edn3.334

Kasting, J. F., & Ackerman, T. P. (1986). Climatic consequences of very high carbon dioxide levels in the Earth's early atmosphere. *Science*, *234*(4782), 1383–1385.

Kelley, D. S., Karson, J. A., Blackman, D. K., Früh-Green, G. L., Butterfield, D. A., Lilley, M. D., Olson, E. J., Schrenk, M. O., Roe, K. K., Lebon, G. T., & Rivizzigno, P. (2001). An off-axis hydrothermal vent field near the mid-Atlantic ridge at 30 N. *Nature*, *412*(6843), 145–149.

Klein, F., Bach, W., & McCollom, T. M. (2013). Compositional controls on hydrogen generation during serpentinization of ultramafic rocks. *Lithos*, *178*, 55–69.

Krissansen-Totton, J., Arney, G. N., & Catling, D. C. (2018). Constraining the climate and ocean pH of the early earth with a geological carbon cycle model. *Proceedings of the National Academy of Sciences of the United States of America*, *115*(16), 4105–4110.

Lafuente, B., Downs, R. T., Yang, H., Stone, N., Armbruster, T., & Danisi, R. M. (2015). *Highlights in mineralogical crystallography* (pp. 1–30). W. De Gruyter.

Lutz, H. D., Möller, H., & Schmidt, M. (1994). Lattice vibration spectra. Part LXXXII. Brucite-type hydroxides $M(OH)_2$ (M = Ca, Mn, Co, Fe, Cd)—IR and Raman spectra, neutron diffraction of $Fe(OH)_2$. *Journal of Molecular Structure*, *328*, 121–132.

Martin, W., Baross, J., Kelley, D., & Russell, M. J. (2008). Hydrothermal vents and the origin of life. *Nature Reviews Microbiology*, *6*(11), 805–814.

Martin, W., & Russell, M. J. (2003). On the origins of cells: A hypothesis for the evolutionary transitions from abiotic geochemistry to chemoautotrophic prokaryotes, and from prokaryotes to nucleated cells. *Philosophical Transactions of the Royal Society of London. Series B: Biological Sciences*, *358*(1429), 59–85.

Mast, C. B., & Braun, D. (2010). Thermal trap for DNA replication. *Physical Review Letters*, *104*(18), 188102.

McGlynn, S. E., Kanik, I., & Russell, M. J. (2012). Peptide and RNA contributions to iron–Sulphur chemical gardens as life's first inorganic compartments, catalysts, capacitors and condensers. *Philosophical Transactions of the Royal Society A: Mathematical, Physical and Engineering Sciences*, *370*(1969), 3007–3022.

Mizuuchi, R., Blokhuis, A., Vincent, L., Nghe, P., Lehman, N., & Baum, D. (2019). Mineral surfaces select for longer RNA molecules. *Chemical Communications*, *55*(14), 2090–2093.

Moelling, K., & Broecker, F. (2021). Viroids and the origin of life. *International Journal of Molecular Sciences*, *22*(7), 3476.

Mojzsis, S. J., Harrison, T. M., & Pidgeon, R. T. (2001). Oxygen-isotope evidence from ancient zircons for liquid water at the Earth's surface 4,300 Myr ago. *Nature*, *409*(6817), 178–181.

Muto, H., Takaki, Y., Hirai, M., Mino, S., Sawayama, S., Takai, K., & Nakagawa, S. (2017). A simple and efficient RNA extraction method from Deep-Sea hydrothermal vent chimney structures. *Microbes and Environments*, *32*, 330–335.

Orsi, W. D., Vuillemin, A., Coskun, Ö. K., Rodriguez, P., Oertel, Y., Niggemann, J., Mohrholz, V., & Gomez-Saez, G. V. (2022). Carbon assimilating fungi from surface ocean to subseafloor revealed by coupled phylogenetic and stable isotope analysis. *The ISME Journal*, *16*(5), 1245–1261.

Pearce, K. D. B., Pudritz, R. E., Semenov, D. A., & Henning, T. K. (2017). Origin of the RNA world: The fate of nucleobases in warm little ponds. *Proceedings of the National Academy of Sciences of the United States of America*, *114*(43), 11327–11332.

Pedreira-Segade, U., Feuillie, C., Pelletier, M., Michot, L. J., & Daniel, I. (2016). Adsorption of nucleotides onto ferromagnesian phyllosilicates: Significance for the origin of life. *Geochimica et Cosmochimica Acta*, *176*, 81–95.

Poulton, S. W., & Canfield, D. E. (2011). Ferruginous conditions: A dominant feature of the ocean through Earth's history. *Elements*, *7*(2), 107–112.

Preiner, M., Asche, S., Becker, S., Betts, H. C., Boniface, A., Camprubi, E., Chandru, K., Erastova, V., Garg, S. G., Khawaja, N., Kostyrka, G., Machné, R., Moggioli, G., Muchowska, K. B., Neukirchen, S., Peter, B., Pichlhöfer, E., Radványi, Á., Rossetto, D., … Xavier, J. C. (2020). The future of origin of life research: Bridging decades-old divisions. *Life*, *10*(3), 20.

Quéméneur, M., Bes, M., Postec, A., Mei, N., Hamelin, J., Monnin, C., Chavagnac, V., Payri, C., Pelletier, B., Guentas-Dombrowski, L., Gérard, M., Pisapia, C., Gérard, E., Ménez, B., Ollivier, B., & Erauso, G. (2014). Spatial distribution of microbial communities in the shallow submarine alkaline hydrothermal field of the Prony Bay, New Caledonia. *Environmental Microbiology Reports*, *6*(6), 665–674.

Rouillard, J., García-Ruiz, J. M., Gong, J., & Van Zuilen, M. A. (2018). A morphogram for silica-witherite biomorphs and its application to microfossil identification in the early earth rock record. *Geobiology*, *16*(3), 279–296.

Russell, M. J. (2018). Green rust: The simple organizing 'seed'of all life? *Life*, *8*(3), 35.

Russell, M. J., Nitschke, W., & Branscomb, E. (2013). The inevitable journey to being. *Philosophical Transactions of the Royal Society B: Biological Sciences*, *368*(1622), 20120254.

Scott, W. G. (2007). Ribozymes. *Current Opinion in Structural Biology*, *17*(3), 280–286.

Stone, D. A., Lewellyn, B., Baygents, J. C., & Goldstein, R. E. (2005). Precipitative growth templated by a fluid jet. *Langmuir*, *21*(24), 10916–10919.

Sugitani, K., Mimura, K., Takeuchi, M., Yamaguchi, T., Suzuki, K., Senda, R., Asahara, Y., & Van Kranendonk, M. J. (2015). A Paleoarchean coastal hydrothermal field inhabited by diverse microbial communities: The Strelley Pool formation, Pilbara craton. *Western Australia. Geobiology*, *13*(6), 522–545.

Trolard, F., Bourrié, G., Abdelmoula, M., Refait, P., & Feder, F. (2007). Fougerite, a new mineral of the pyroaurite-iowaite group: Description and crystal structure. *Clays and Clay Minerals*, *55*(3), 323–334.

Trolard, F., Duval, S., Nitschke, W., Ménez, B., Pisapia, C., Nacib, J. B., Andréani, M., & Bourrié, G. (2022). Mineralogy, geochemistry and occurrences of fougerite in a modern hydrothermal system and its implications for the origin of life. *Earth-Science Reviews*, *225*, 103910.

Usman, M., Byrne, J. M., Chaudhary, A., Orsetti, S., Hanna, K., Ruby, C., Kappler, A., & Haderlein, S. B. (2018). Magnetite and green rust: Synthesis, properties, and environmental applications of mixed-valent iron minerals. *Chemical Reviews*, *118*(7), 3251–3304.

White, L. M., Bhartia, R., Stucky, G. D., Kanik, I., & Russell, M. J. (2015). Mackinawite and greigite in ancient alkaline hydrothermal chimneys: Identifying potential key catalysts for emergent life. *Earth and Planetary Science Letters*, *430*, 105–114.

White, L. M., Shibuya, T., Vance, S. D., Christensen, L. E., Bhartia, R., Kidd, R., Hoffmann, A., Stucky, G. D., Kanik, I., & Russell, M. J. (2020). Simulating serpentinization as it could apply to the emergence of life using the JPL hydrothermal reactor. *Astrobiology*, *20*(3), 307–326.

SUPPORTING INFORMATION

Additional supporting information can be found online in the Supporting Information section at the end of this article.

How to cite this article: Helmbrecht, V., Weingart, M., Klein, F., Braun, D., & Orsi, W. D. (2023). White and green rust chimneys accumulate RNA in a ferruginous chemical garden. *Geobiology*, *21*, 758–769. https://doi.org/10.1111/gbi.12572

Acknowledgements

First of all, I want to thank Dieter for giving me the opportunity to pursue this research, explore so many different aspects of the origin of life and learning so many things along the way. You taught me, that sometimes just starting and trying something new without meticulously planning can be more efficient to make progress.

I also want to thank Karen for treating me as her "adopted PhD Student', giving me the chance to continue researching my idea on the 2D vents and teaching me a lot about paper writing.

Many thanks also go to Bill for helping me with all my geo-biological questions and always having an open ear for the discussion of my results or future project perspectives.

Thanks to Christof for being the most universal person in our lab and always having an idea to approach or solve a problem. Working with you is a pleasure and I am always happy to discuss your new bike equipment.

I also want to thank everyone in the collaborations for my projects. Ömer and Lea for the great team efforts despite the covid restrictions. Clara and Siyu for the hard efforts on the 2D vent project. Vanessa for our mutual support and being an amazing conference buddy.

Special thanks also go to Almuth, Vanessa, Juliette and Mona for proof-reading and comments on my thesis.

A very huge thank you to all my great colleagues and friends form the baunlab. Without all of you, this group and the everyday lablife would not be the same. Especially I want to thank all the old-school braunies, Patta, Chrissy, Thomas, Annalena and Alex K. You introduced me to the braunie-spirit and our breakfast/lunch breaks made the days in the lab even better. Noel and Avinash, it has been always great to mess around with the postdocs, but at the same time also have helpful discussions about our research. Juliette, Sree, Philipp and Adriana for initiating many of our after work events and making sure we had many relaxing evenings together. Saroj for spoiling us with so much amazing food. Bobby for making the lab a better place. Alex F., Paula, Felix for introducing the new generation of braunies and making sure there is always room for fun.

I want to thank Almuth, not only for enduring all my chemistry related questions over the years, but mainly for always being there for me and reassuring me, whenever I was doubtful about so many things. I am lucky to have you in my life.

Thanks to my family, my parents and my brother for always supporting me along my way and especially to my grandpa, for listening to all my progress and being excited with my during my paper submission.